The characteristics of mesoscale convective system rainfall over Europe

Nicolas A. Da Silva[1] and Jan O Haerter[1]

[1]Leibniz Centre for Tropical Marine Research

April 16, 2023

Abstract

Mesoscale Convective Systems (MCS) are common over Europe and can produce severe weather, including extreme precipitation, which can lead to flash floods.
The few studies analyzing the climatological characteristics of MCS over Europe are either based on only few years of data or focus on limited sub-areas.
Using the recent Integrated Multi-satellitE Retrievals for Global Precipitation Measurement (IMERG) satellite precipitation climatology, we identify and track MCS for 16 years over Europe.
We devise a spatial filter and track cells according to the overlap of filtered rain patches between consecutive time steps.
By fitting an ellipse to these patches, we determine their overall shape and orientation.
To distinguish convective rain patches we condition on lightning data, thus reducing potential identification errors.
We analyze this new European MCS climatology to characterize MCS rainfall properties:
MCS overall occur most frequently over the Mediterranean and Atlantic during fall and winter, whereas during summer, they concentrate over the continent.
Typically, more than half of seasonal precipitation can be attributed to MCS, and
their contribution to extreme precipitation is even greater, often exceeding 70\%.
MCS over the continent display a clear diurnal cycle peaking during the afternoon, and some continental areas even show a second, nocturnal peak.
The MCS diurnal cycle for coastal and oceanic regions is more variable.
Selecting sub-areas, we find that the spatio-temporal distribution of MCS precipitation throughout the year can be well explained by the spatio-temporal distribution of specific environmental variables, namely (sea) surface temperature, fronts occurrence and convective instability.

The characteristics of mesoscale convective system rainfall over Europe

Nicolas A. Da Silva[1] **and Jan O. Haerter**[1,2,3]

[1]Complexity and Climate, Leibniz Centre for Tropical Marine Research, Fahrenheitstrasse 6, 28359 Bremen, Germany.
[2]Physics and Earth Sciences, Constructor University Bremen, Campus Ring 1, 28759 Bremen, Germany.
[3]Niels Bohr Institute, University of Copenhagen, Blegdamsvej 17, 2100 Copenhagen, Denmark.

Key Points:

- MCS substantially contribute to precipitation totals and dominate event-based rainfall extremes over Europe.
- MCS's diurnal cycle displays a large variability over the coasts and may exhibit nocturnal peaks over continental areas.
- The yearly cycle of MCS rainfall is understood with the yearly cycle of surface temperature, convective instability, and frontal activity.

Corresponding author: Nicolas A. Da Silva, `nicolas.da-silva@leibniz-zmt.de`

Abstract

Mesoscale Convective Systems (MCS) are common over Europe and can produce severe weather, including extreme precipitation, which can lead to flash floods. The few studies analyzing the climatological characteristics of MCS over Europe are either based on only few years of data or focus on limited sub-areas. Using the recent Integrated Multi-satellitE Retrievals for Global Precipitation Measurement (IMERG) satellite precipitation climatology, we identify and track MCS for 16 years over Europe. We devise a spatial filter and track cells according to the overlap of filtered rain patches between consecutive time steps. By fitting an ellipse to these patches, we determine their overall shape and orientation. To distinguish convective rain patches we condition on lightning data, thus reducing potential identification errors. We analyze this new European MCS climatology to characterize MCS rainfall properties: MCS overall occur most frequently over the Mediterranean and Atlantic during fall and winter, whereas during summer, they concentrate over the continent. Typically, more than half of seasonal precipitation can be attributed to MCS, and their contribution to extreme precipitation is even greater, often exceeding 70%. MCS over the continent display a clear diurnal cycle peaking during the afternoon, and some continental areas even show a second, nocturnal peak. The MCS diurnal cycle for coastal and oceanic regions is more variable. Selecting sub-areas, we find that the spatio-temporal distribution of MCS precipitation throughout the year can be well explained by the spatio-temporal distribution of specific environmental variables, namely (sea) surface temperature, fronts occurrence and convective instability.

Plain Language Summary

Extreme rainfall events leading to flash floods have major socio-economical impacts over Europe. These events are often created by large and long-lived clusters of clouds called Mesoscale Convective Systems (MCS). Although these MCS are well known by the climate community, their rainfall characteristics over Europe are not fully documented. This is the purpose of this study. Here, we identify MCS by using satellite images (detecting rainfall) and lightning strikes for 16 years over Europe. We also develop a tracking algorithm, enabling us to follow each MCS in time and space. The recognition of individual MCS is based on the overlap of rainfall patches between two consecutive satellite images. We find that MCS overall occur most frequently over the Mediterranean and Atlantic during fall and winter, whereas during summer, they concentrate over the continent. We show that they substantially contribute to the yearly total rainfall over Europe. More remarkably, MCS is the most frequent cloud organization form responsible for extreme rainfall events over Europe. Thus, while the present study gives some general explanations on their main behavior, it is of critical importance to further understand European MCS and their potential changes in a warming climate.

1 Introduction

Mesoscale Convective Systems (MCS) are aggregates of cumulonimbus clouds spanning a few hundreds of kilometers horizontally (R. A. Houze, 2018). These organized weather systems are abundant over the tropics where they contribute to more than half of the total rainfall (Laing & Fritsch, 1997; Nesbitt et al., 2006; Liu & Zipser, 2015; Tan et al., 2015; Schumacher & Rasmussen, 2020; Feng et al., 2021). Despite the frequent occurrence of stratiform rainfall from extra-tropical cyclones in mid-latitudes, MCS are also a significant contributor to mid-latitude precipitation (Haberlie & Ashley, 2019; Feng et al., 2021), in particular during summer when thunderstorm activity is most pronounced (Taszarek et al., 2019) In addition to their significant impact on the hydrological cycle, MCS are often associated with severe weather such as heavy rainfall, large hail, strong winds, or tornadoes (Jirak et al., 2003; Mathias et al., 2017; Luo et al., 2020; Schumacher & Rasmussen, 2020; Fowler et al., 2021). In fact, MCS areas and rain intensities tend to be larger in mid-latitudes than in the tropics, possibly due to larger wind shear (Schumacher & Rasmussen, 2020). It is therefore important to understand the characteristics of mid-latitude MCS and how these may change with global change.

Several studies have focused on the climatological properties of MCS around the globe. In the USA, MCS preferentially occur in the Midwest during the warm season and in the mid-south during the cold season (Cui et al., 2020; Haberlie & Ashley, 2019). In the warm season, they were found to emerge along the eastern flank of the Rocky Mountains (Cheeks et al., 2020) in the late afternoon and subsequently propagate eastward, peaking at night in the central great plains (Geerts et al., 2017). It was suggested that the nocturnal MCS precipitation peak might be related to the peak in the Low Level Jet (LLJ, Pitchford and London (1962)) as well as both gravity waves (Parker, 2008) or potential vorticity anomalies (Jirak & Cotton, 2007) generated and advected away from the Rockies. A nocturnal peak in MCS precipitation was also observed in eastern China (Li et al., 2020) and Argentina (Salio et al., 2007). Both these regions have a mountain range in their western parts (Tibetan Plateau and Andes, respectively) and thus feature similar topographic characteristics as the midwest USA. Conversely, the varied European topography with several mountain ranges oriented along different directions might make for a more complex picture of the MCS diurnal cycle.

Focusing on a restricted part of Europe (García-Herrera et al., 2005; Punkka & Bister, 2015; Rigo et al., 2019; Surowiecki & Taszarek, 2020), investigating only one season (Morel & Senesi, 2002; Kolios & Feidas, 2010), or using a limited time record to assess climatological properties (Morel & Senesi, 2002; García-Herrera et al., 2005; Kolios & Feidas, 2010), several studies have examined MCS over Europe. Using five years of infrared (IR) satellite data, Morel and Senesi (2002) found that summer MCS (April-September) are more common over land than sea and are triggered near mountainous areas (Pyrenees, Alps, Carpathians) during the afternoon, a general characteristic also found for the USA.

The present study composes a comprehensive MCS rainfall climatology over Europe from 16 years of the Integrated Multi-satellitE Retrievals for GPM (IMERG) combined with EUropean Cooperation for LIghtning Detection (EUCLID) lightning data. MCS were often identified as large contiguous areas of low IR radiation emitted from cold convective anvils. While this approach is successful over the tropics, it may not be appropriate over mid-latitudes which are also subject to large frontal non-MCS systems that come with similarly low brightness temperatures. This is why more robust methods were recently developed for identifying MCS in the mid-latitudes (Feng et al., 2021), making use of the precipitation field to distinguish between convective and non convective systems, since convective cells generally produce more extreme rainfall rates than stratiform-type systems. However, since our objective is to investigate the relation between MCS and precipitation intensity, we adopt yet another, precipitation rate-independent, approach, which instead resorts to lightning strikes.

The present study thus aims at characterizing and understanding the hydrological "footprint" and the diurnal cycle of MCS precipitation over Europe. In Sec. 2, we describe the data sets exploited and how they are used to detect and track MCS. The contribution of MCS to both extreme and mean precipitation over Europe, as well as the MCS diurnal cycle, are characterized in Sec. 3. We then investigate the causes explaining the regional and seasonal differences of MCS precipitation (Sec. 4). Finally, we discuss our results and conclude (Sec. 5).

2 Data and tracking algorithm

Our method shares aspects with Feng et al. (2021) but primarily defines patches with the precipitation field instead of cloud top brightness temperatures and uses lightning data to distinguish convective patches.

2.1 Data

2.1.1 Integrated Multi-Satellite Retrievals (IMERG)

We identify precipitating features (PF) using the IMERG precipitation product, version V06B, from the Global Precipitation Measurement (GPM) project (Huffman et al., 2019). This product merges measurements from a constellation of satellites, carrying passive microwave (PM) and/or infrared (IR) sensors. While the PM sensors are generally more precise since they are directly measuring the signal alteration by precipitation droplets, their spatio-temporal coverage is limited. In contrast, IR sensors measure precipitation indirectly through cloud top brightness temperatures, but have a higher spatio-temporal resolution. The precipitation estimates from every satellite are inter-calibrated and combined to produce a half-hourly estimate of precipitation at 0.1^o of horizontal resolution which is monthly calibrated by the Global Precipitation Climatology Project (GPCP) satellite-gauge product (Adler et al., 2018).

2.1.2 European Cooperation for Lightning Detection (EUCLID)

To differentiate convective from stratiform weather systems, we employ the EUCLID lightning dataset (Schulz et al., 2016; Poelman et al., 2016). Only cloud to ground lightning strikes (CG) are used since they display spatio-temporal homogeneity from 2005 to 2020. The original dataset provides the number of CG in 30-minute time windows and on a 0.045^ox0.064^o grid covering most of Europe. We linearly interpolated the original lightning dataset to the IMERG grid (0.1^ox0.1^o) to achieve spatial coherence between both datasets.

2.1.3 General Bathymetric Chart of the Oceans (GEBCO)

Since mountain ranges were found to play an important role in the genesis of MCS in mid-latitudes (Morel & Senesi, 2002; Cheeks et al., 2020), we also make use of the GEBCO topography dataset.

2.1.4 ERA5

Several variables (SST; 2-m and 600 hPa temperatures; 600 hPa zonal and meridional wind speed; Convective Available Potential Energy (CAPE)) from the ERA5 global reanalysis product (Hersbach et al., 2020) are used to provide insights on the processes involved explaining the spatio-temporal distribution of MCS over Europe (in section 4).

2.2 MCS tracking algorithm

Detecting precipitation features and tracks. Similar to Feng et al. (2021), we first apply a spatial filter of 0.3^o to IMERG precipitation (Fig. 1ab), in order to define coherent PF that are not simply an artifact resulting from noise, and allow for "gaps" of a few tens of km to in the precipitation pattern of a PF. The PF are defined as contiguous patterns (when considering the four nearest neighbors on the regular longitude-latitude IMERG grid) of filtered precipitation above $2\,\mathrm{mm.h^{-1}}$ (red contours in Fig. 1b). Other thresholds ($0.5\,\mathrm{mm.h^{-1}}$, $1\,\mathrm{mm.h^{-1}}$, $3\,\mathrm{mm.h^{-1}}$ and $4\,\mathrm{mm.h^{-1}}$) were tested and $2\,\mathrm{mm.h^{-1}}$ was found to give the best compromise in order to discard many weak and sporadic systems that increase computational cost while preserving the main spatial patterns of the most significant systems.

All PFs are labeled at each time step as follows: when a PF spatially overlaps with another PF at the previous time step, it receives the same identification number (IN). Under strong wind conditions, it might occur that the area covered by one precipitation system does not overlap with the area covered by the same precipitation system 30 minutes earlier (especially for small systems). To limit identification errors related to these occurrences, we adopt the iterative strategy of Moseley et al. (2013) computing the mean displacement of all neighboring PFs within a 1000 km radius around a non-overlapping PF, then translating the non-overlapping PF backward in time with the resulted displacement vector, and searching for overlap in the corresponding new position. We perform this procedure for every non overlapping PFs and iterate until not any new overlap is found and not any new neighboring PF is found.

If a PF (e.g. Fig. 1d) spatially overlaps with several PFs at the previous time step (e.g. Fig. 1e), the IN of the PF that has the largest overlap is chosen for the new PF (merging case). A PF receives a new IN when it does not overlap with any PF at the previous time step. Conversely, if two new PFs (e.g. Fig. 1e) overlap with the same PF at the previous time step (e.g. Fig. 1d), the new PF that has the largest overlap with the old PF keeps its IN while the other new PF gets a new IN (splitting case). These choices correspond to the case of $\theta = 1$ in the method proposed by Moseley et al. (2019) to address splitting and merging cases.

In order to define shape properties, such as diameter, orientation, and eccentricity, we then fit an ellipse to each PF and at each time step. The fitting algorithm minimizes the sum of the distances between the contours of the PF and the ellipse in a least square sense (see Fig. 1c). In this algorithm, the area of the ellipse is set to be equal to the area of the PF and the center of the ellipse is fixed to the geometric center of the PF (red point in Fig. 1bc). The goodness of the ellipse fit (G) is defined as follows:

$$G = 1 - \frac{A_{ell,out} + A_{PF,out}}{A_{ell} + A_{PF}} = 1 - \frac{A_{ell,out}}{A_{PF}}\ , \tag{1}$$

where $\mathrm{A_{PF}} = \mathrm{A_{ell}}$ is the areas of the PF (defined as the sum of the pixel areas belonging to the PF) and ellipse, $\mathrm{A_{ell,out}}$ is the ellipse area outside of the PF, and $\mathrm{A_{PF,out}}$ the PF area outside of the ellipse. The probability density function (PDF) of G is displayed in Figure S1a. It shows that most of the PFs are well fitted by the ellipse with G values mostly ranging from 0.6 and 1 (99.5% of the PFs). The maximum of G occurrence is at around 0.95, which corresponds to the average value of G obtained for the ellipse fitting of small area PFs containing few pixels (Fig. S1b) and which are also the most frequent. The lowest values of G correspond to large area and complex PFs whose shapes can not be well represented by an ellipse.

Defining convective precipitation features and MCS. We now define convective and stratiform PFs by using the EUCLID lightning dataset regridded to match the IMERG grid. At any time of its "life cycle", a PF for which at least one CG was detected inside or in the vicinity (at a distance of less than 5 km) of its ellipse during the corresponding IMERG 30-minutes time window is defined as an "isolated convective PF". In this study, an MCS is a PF which experiences a diameter of at least 100 km for at least four consecutive hours during which at least one CG was detected at a distance of less than 5 km from its ellipse. Another approach, which makes use of ERA5 CAPE instead of lightning data (described in supplementary materials), was tested to define convective PFs and produced similar results for MCS (Figs S2, S3), showing that the MCS identification is robust. Here we choose to keep using the EUCLID lightning dataset as we believe that it provides a more direct detection of convective occurrence. Figure 2a is a snapshot of IMERG precipitation, EUCLID lightning strikes, and the objects detected by our algorithm on 9 June 2014 at 23h45 CEST, where intense MCS associated with severe

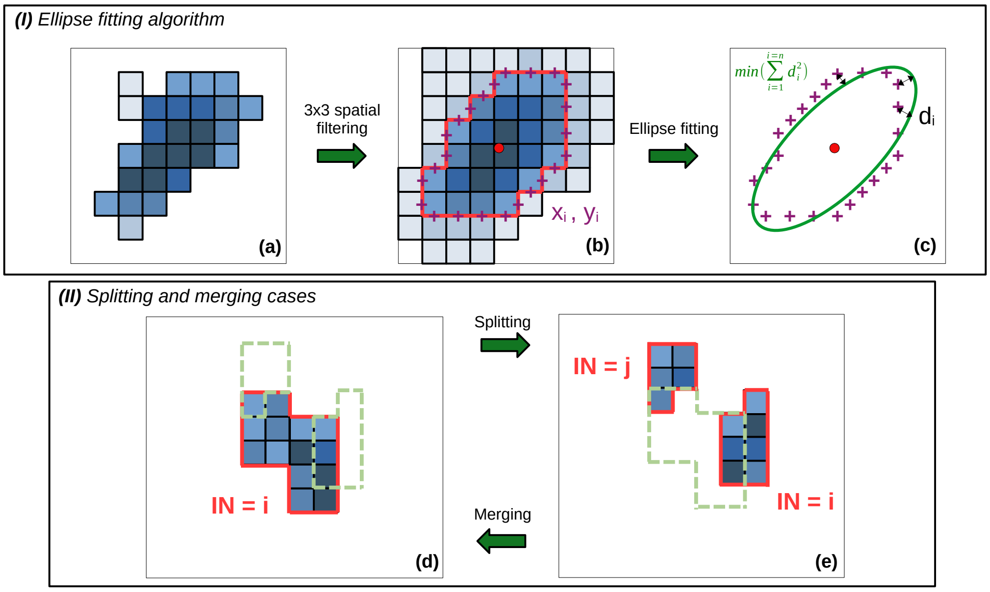

Figure 1. Scheme describing the PF identification (a,b), the ellipse fitting algorithm (c) and the treatment of splitting and merging (d,e) by our algorithm. First, the IMERG precipitation field (represented by blue pixels, with darker blue colors standing for more intense precipitation) is spatially filtered (a,b). Second, contours of filtered precipitation above 2 mm.h^{-1} are drawn (in red) to define PFs (b). The centers of the edges of the pixel contours (purple crosses) are used to fit an ellipse (in green) to each PF by minimizing the distance between the PF contours and the ellipse (c). The snapshots d and e represent two consecutive time steps for which the PF contours of the previous/next time step are reminded in light green dashed lines for an easier identification of the overlaps.

weather were observed in western Europe (Mathias et al., 2017). It shows a general good correspondence between the lightning strikes and the precipitating cells emerging from two different datasets, as well as fairly consistent ellipse fits to these objects. One can see that with the threshold approach, only the largest precipitating cells are detected by the algorithm.

For the analysis in the current work we retain unfiltered precipitation from the original IMERG grid. Since the PFs are defined using the spatial average of IMERG precipitation from 3x3 grid points, all of these unfiltered IMERG precipitation grid points contributing to the spatially filtered precipitation field of a particular PF are retained for this PF. This procedure may result in precipitation grid boxes belonging to two (or more) PF at the same moment. We have checked the PDFs with and without these repeated pixels and found that the differences are minor (not shown) and therefore retained this approach.

3 MCS climatology over Europe

3.1 Overall characteristics — MCS are more than a sum of stratiform and convective cells

With the algorithm described above, we were able to detect a total of 11,092 MCS from 2005 to 2020 (on average 693 per year) in our European domain (−13°W to 38°E, 30°N to 59°N; Fig. 3). To give an overview, Figure 2b shows the PDF of the duration

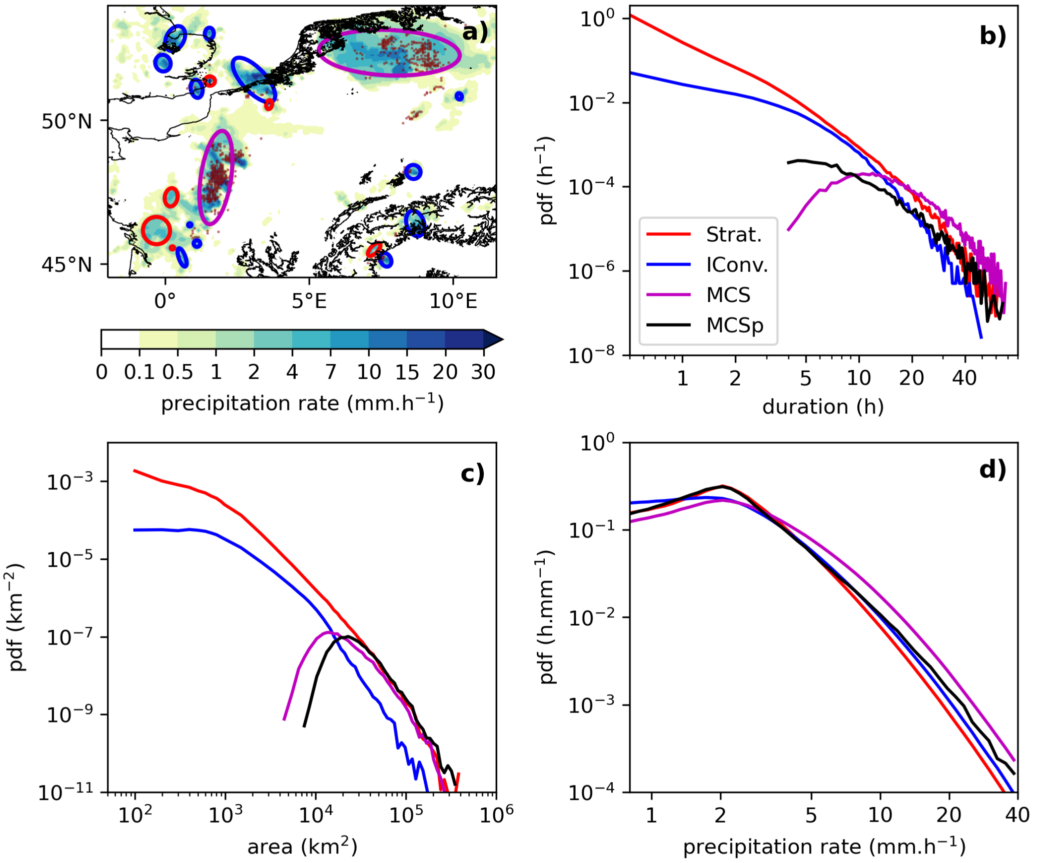

Figure 2. Snapshot of IMERG precipitation (shadings; in mm.$^{\mathrm{h}}-1$) and EUCLID lightning strikes (dark red points) on 9th June 2014 at 23h45 CEST in western Europe (a). The ellipses represent the detected PF according to our algorithm presented in section 2: red for stratiform PF, blue for isolated convective PF, and magenta for MCS PF. Probability density functions (PDF) of precipitation features (PF) duration (b; in h), mean area (c; in km^2), and precipitation (d; in mm.h^{-1}) for stratiform ("Strat.", red), isolated convective ("IConv.", blue), MCS PF (magenta), and for MCS periods ("MCSp", black). MCSp was built by selecting only instants for which a MCS PF has MCS attributes (see section 3a). The PDF of duration and area were normalized by the the total number of PF while the PDF of precipitation were normalized by the number of instants of PF of the corresponding type (stratiform, isolated convective, MCS, or MCS periods).

of detected PF for the different types (stratiform, isolated convective, MCS). Since MCS are sometimes embedded in fronts, the duration of MCS PF can reach several days whereas the actual MCS activity may only last for few hours. To account for this potential difference, we also plot the PDF of MCS periods, defined as instants which are part of a four consecutive hours with diameter exceeding 100 km and for which a lightning strike was detected within these same 4 consecutive hours. For stratiform and isolated convective precipitation, the PDF monotonically decreases with PF duration. The isolated convective PFs display a more selective range of life duration than the stratiform, as seen by the stronger curvature of the blue curve compared to the red, in agreement with the previously reported data by (Berg & Haerter, 2013) but for local rain durations in Germany. We find typical MCS lifetimes to be around 10 hours when accounting for inac-

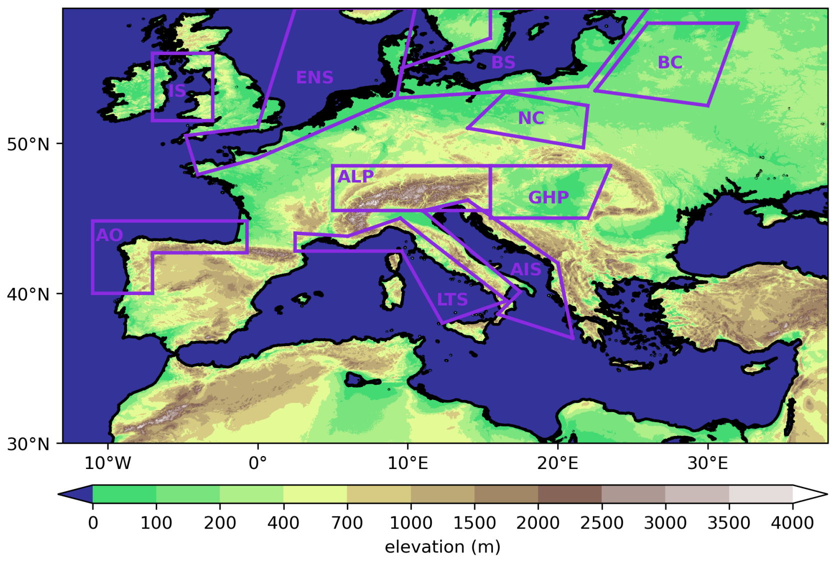

Figure 3. Study domain highlighting sub-regions: AO for Atlantic Ocean, IS for Irish Sea, ENS for English channel and North Sea, LTS for Ligurian and Tyrrhenian Seas, ALP for Alps, BS for Baltic Sea, AIS for Adriatic and Ionian Seas, NC for north Carpathian, GHP for Great Hungarian Plains and BC for Baltic Continent. The shadings represent the elevation (in m).

tive periods, whereas the duration of the active MCS periods are shorter by about a half of the total MCS life time. The area distribution (Fig. 2c) closely mirrors that of duration. In detail, mean MCS areas are even more selective, their occurrence frequency peaking for areas around $10^4\,\mathrm{km}^2$, which is partly influenced by our detection method enforcing a size threshold of 100 km of diameter. The PDF of mean precipitation (Fig. 2d) shows that high precipitation intensities, $> 10\,\mathrm{mm.h}^{-1}$, are approximately three times more frequent within MCS than for isolated convective PFs, and isolated convective cases are overall more intense than stratiform ones. The maximum around 2 $\mathrm{mm.h}^{-1}$ can be attributed to our detection threshold.

Given the intensity distributions (Fig. 2d), MCS can not only be seen as a collection of stratiform and convective precipitation patches but there is a systematic precipitation enhancement. This may result from the merging of convective cells, possibly related to dynamical (cold pools and/or mesoscale circulation; e.g. Haerter and Schlemmer (2018)) and/or microphysical effects (reduced entrainment and/or rain evaporation; e.g. Da Silva et al. (2021)).

3.2 MCS dominate in southern coastal regions in winter and continental regions in summer

As noted (Taszarek et al., 2019), mid-latitude convection is strongly dependent on season, a feature we examine further by examining the MCS occurrence for the different months (Fig. 4). As might be expected from the overall precipitation climatology in Europe (Fig. S4), MCS are generally more frequent in the coastal regions of southern Europe in winter, whereas they dominate in summer for the North. It is however worth pointing out that longitudinal differences exist: e.g., along the Eastern Adriatic the overall highest MCS frequency (approximately six per month) is reached in November, whereas the remaining Mediterranean or the continental regions at similar latitude, show a factor 2—3 less. Similar variations are seen in northwestern Spain or the Italian west coast during fall, where frequencies are again much higher than for similar latitudes. As opposed to the strong activity during fall, the transitional period during spring shows generally weak MCS activity. This lack of symmetry regarding MCS during the transitional periods, where continental temperatures are fairly similar, points to a strong influence of the large water bodies, with their large heat capacities, thus memory, on MCS. Summertime MCS, e.g., from June to August, are most frequent over the Alps, reaching about five per month in August. To a lesser extent this effect also holds for the Carpathians, highlighting the role of topography in triggering/enhancing deep convection (J. Houze & Robert, 2012). Perhaps more surprisingly, the continental regions near the East of southern Baltic Sea experience an important peak of MCS occurrence during the month of July, with around 3.5 MCS in this month on average. Another remarkable feature is the high number (exceeding 4 on average) of MCS in both southern Baltic Sea and southern North Sea (especially in the southeastern side) during August, while the surrounding continental areas experience comparably fewer MCS. The spatial peak of MCS occurrence over these regions extends to the fall months. Finally, one may notice that northern Germany experiences fewer MCS than its surrounding regions between June to September. This may be due to the Alps acting as a barrier to some of the MCS, which mostly travel in southwesterly flows (not shown).

Similarities between the spatial distribution of MCS occurrence in our current study and previous studies exist for the summer months. Yet, there are some noticeable differences compared to the previous climatologies of summer MCS (Morel & Senesi, 2002; Kolios & Feidas, 2010). While some of the difference might be explained by the longer averaging time used by the present study, an important difference lies in our method of identifying MCS by precipitation and lightning, whereas both Morel and Senesi (2002) and Kolios and Feidas (2010) used a method based on cloud top brightness temperature. In particular, we found a peak of MCS occurrence in both the North Sea and the Baltic Sea during August and a generally higher MCS occurrence in northern Europe during the warm season compared to Morel and Senesi (2002). Similarly, while the peak of MCS frequency in fall over the eastern Adriatic is expected (Feng et al., 2021; Taszarek et al., 2019), the peak over northwestern Spain is more surprising and was not found in previous studies based on cloud top brightness temperature for MCS identification (García-Herrera et al., 2005; Feng et al., 2021). We believe that the MCS over the North Sea and the Baltic Sea in late summer, and those over northwestern Spain during the cold season, are due to less deep convective systems that do not satisfy the IR criteria but have a large area and still produce some lightning.

Thus, MCS affect many regions over Europe throughout the year, and, due to their convective nature and their large spatial extent, MCS often generate large amounts of precipitation both in time and in space (e.g., Schumacher and Johnson (2005)). In the following, we quantify their contribution to total and extreme precipitation for each seasons (DJF, MAM, JJA, SON).

3.3 Substantial MCS contributions to rainfall totals

Again distinguishing seasons, MCS account for large precipitation amounts exceeding 100 mm in a single season over large areas (Fig. 5), which often corresponds to more than an half of the total rainfall in this season (Fig. 6). Overall, MCS precipitation dominate convective precipitation (Fig. S5) and its spatial patterns are generally commensurate with those of MCS frequency in the previous section (Fig. 4) and those of the mean precipitation climatology (Fig. S4). There are however smaller scale differences that can be attributed to the average spatial distribution of precipitation within individual MCS. In winter and to a lesser extent in fall, precipitation totals stemming from MCS tend to peak offshore along the coasts, a pattern that is even more pronounced for isolated convection (Fig. S6) and suggesting a role of the land-sea contrasts for MCS triggering in these seasons. The regions most affected by MCS precipitation are eastern Adriatic, west-

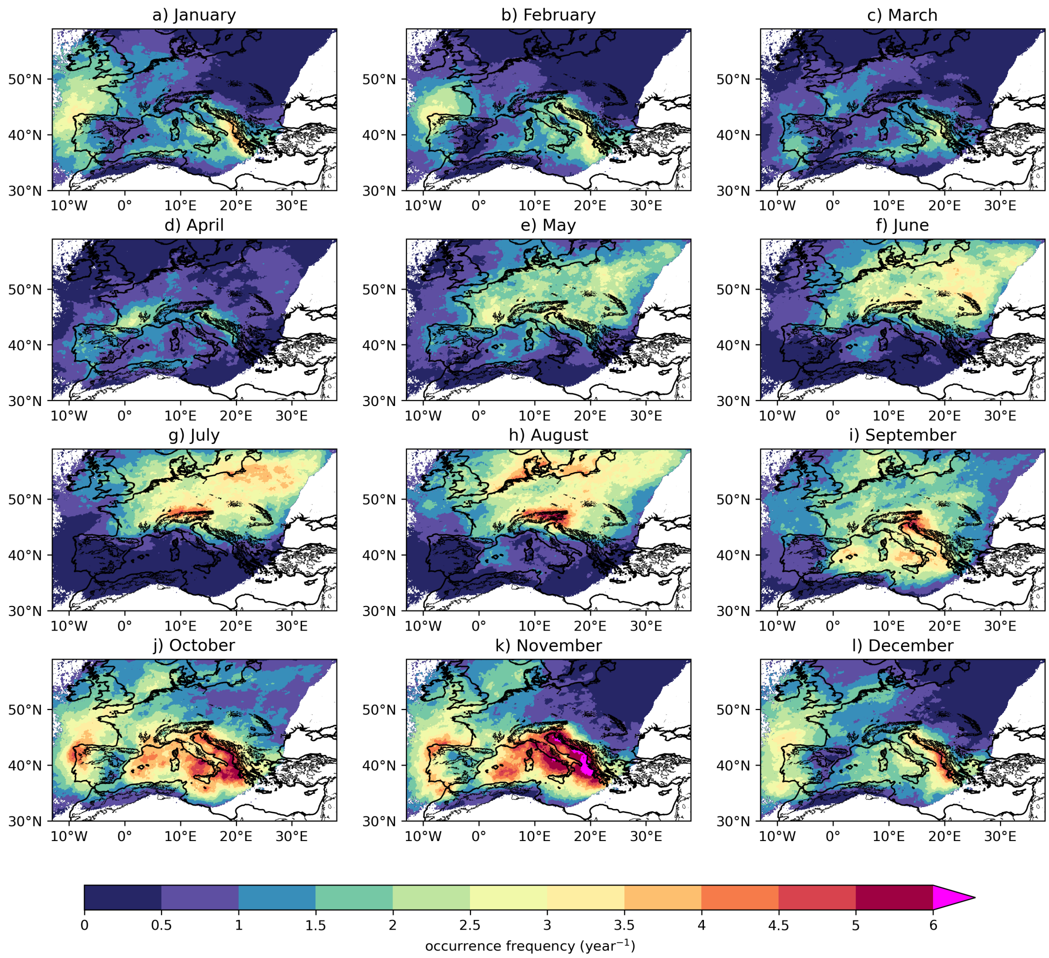

Figure 4. Averaged number of MCS per year by month (a-i). White areas represent missing values, defined as points with means of less than one lightning strike per year.

ern Italy, and south eastern France during fall, with MCS rainfall contributions exceeding 300 mm on average, which corresponds to 60% to 80% of the total precipitation. Northwestern Spain also exhibits a pronounced peak exceeding 200 mm in both fall and winter, although the contribution to total precipitation is somewhat lower with 40-50%. This region, and more generally most of northern Europe is also significantly impacted by stratiform precipitation stemming from Atlantic low pressure systems (Fig. S7), explaining relatively low MCS contributions to total precipitation, there. The MCS contribution to total precipitation is comparatively higher in southern Portugal in all seasons although the number of MCS affecting northwestern Spain is higher.

In spring, MCS precipitation amounts are more homogeneous between continents and seas, reaching about 30-50 mm over large areas, which corresponds to 30-40% of total precipitation. The summer MCS precipitation peaks at about 200 mm over the mountain ranges and the northern Seas of Europe, corresponding to about half of the seasonal total precipitation in these areas.

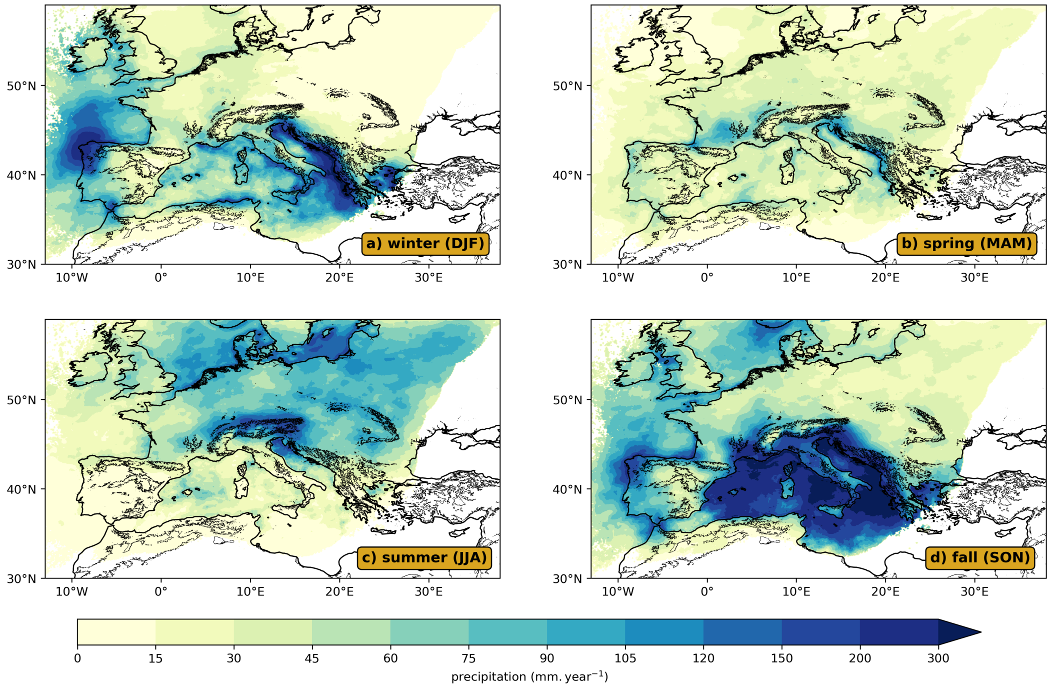

Figure 5. Total precipitation per year (in mm.year^{-1}) from MCS over Europe in winter (DJF, a), spring (MAM, b), summer (JJA, c) and fall (SON, d).

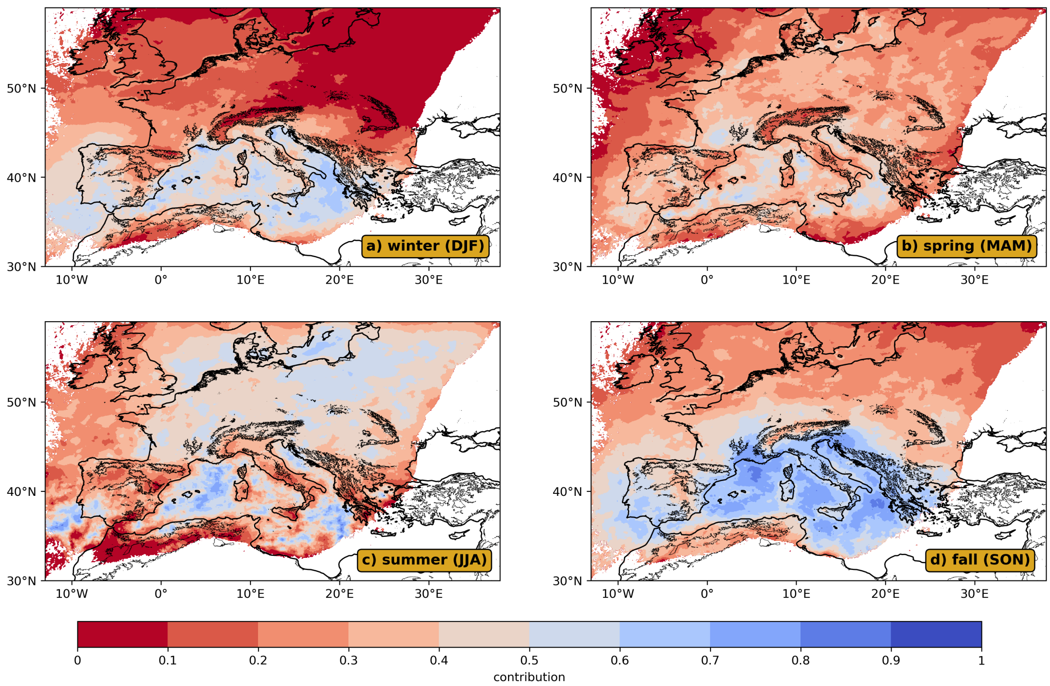

Figure 6. Contribution of MCS to total precipitation over Europe in winter (DJF, a), spring (MAM, b), summer (JJA, c) and fall (SON, d).

3.4 Extreme precipitation dominated by MCS

One of the most common hazards resulting from MCS is their tendency to generate intense precipitation accumulations over extended regions. To quantify the MCS contribution to extreme precipitation accumulations we first derive the 90th percentile of event-based precipitation accumulations from individual PFs (both MCS and non-MCS PFs) for each pixel (displayed in Fig. 7). We select areas where the amplitude of the confidence interval (at 95% of confidence level) on the 90th percentile of precipitation accumulations does not exceed 10 percents to ensure a reasonable definition of the 90th percentile. One can see that the PFs tend to produce heavy rain accumulations over the Mediterranean in all seasons but especially during fall and winter where the 90th percentile of precipitation accumulation due to individual PFs exceeds 40 mm along the coasts. Most of the coastal areas exhibit maxima in extreme precipitation accumulations, as noticed for both isolated convective and MCS precipitation totals (Fig. 5, S6). By compositing over events over several of the coasts in December (Fig. S8, S9), we found that their maxima are often associated with enhanced low-level winds from sea to land, suggesting enhanced convergence of moisture by the reduction of wind speed when propagating inland, e.g., due to increased surface roughness or/and the presence of topography. We find this to be a characteristic of coastal isolated convective events and most coastal MCS.

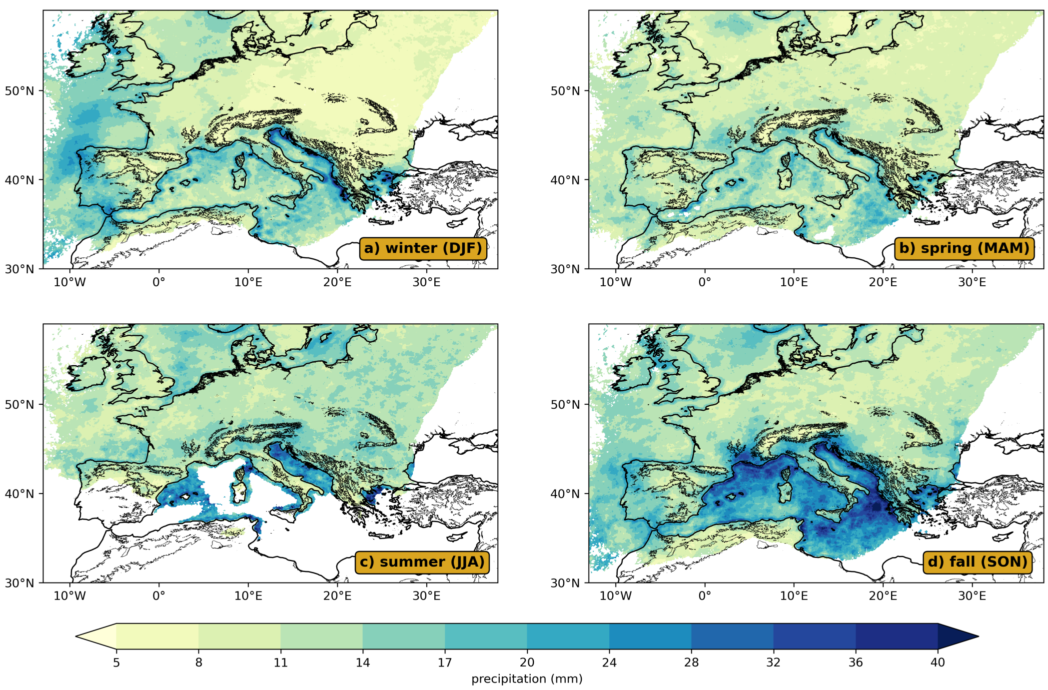

Figure 7. 90th percentile of individual PF precipitation accumulations (in mm) over Europe in winter (DJF, a), spring (MAM, b), summer (JJA, c) and fall (SON, d). White areas are missing data, i.e. points with an insufficient number of PFs (section 3.4) or with means of less than one lightning strike per year.

For each pixel we then select all PFs that produce rainfall exceeding the local 90th percentile of precipitation accumulation. By determining the fractional contribution by MCS (Figure 8) we show that MCS contribute more strongly to extreme precipitation events than to the mean. In some parts of the Mediterranean and the southern Iberian Peninsula, this contribution reaches a peak during fall approaching 100% and remains high (> 70%) during winter. In summer, more than 70% of rainfall accumulation extremes in continental Europe are due to MCS while the remaining 30% are mainly due to isolated convective events (Fig. S10). Although MCS are not particularly frequent in spring, their contribution to extreme precipitation accumulation is significant, exceeding 50% in most of Europe (except UK) and in the Mediterranean area. In this season, the remainder of extreme rainfall events is due isolated convective and stratiform rainfall (Fig. S11), with a similar share between these two (around 25%).

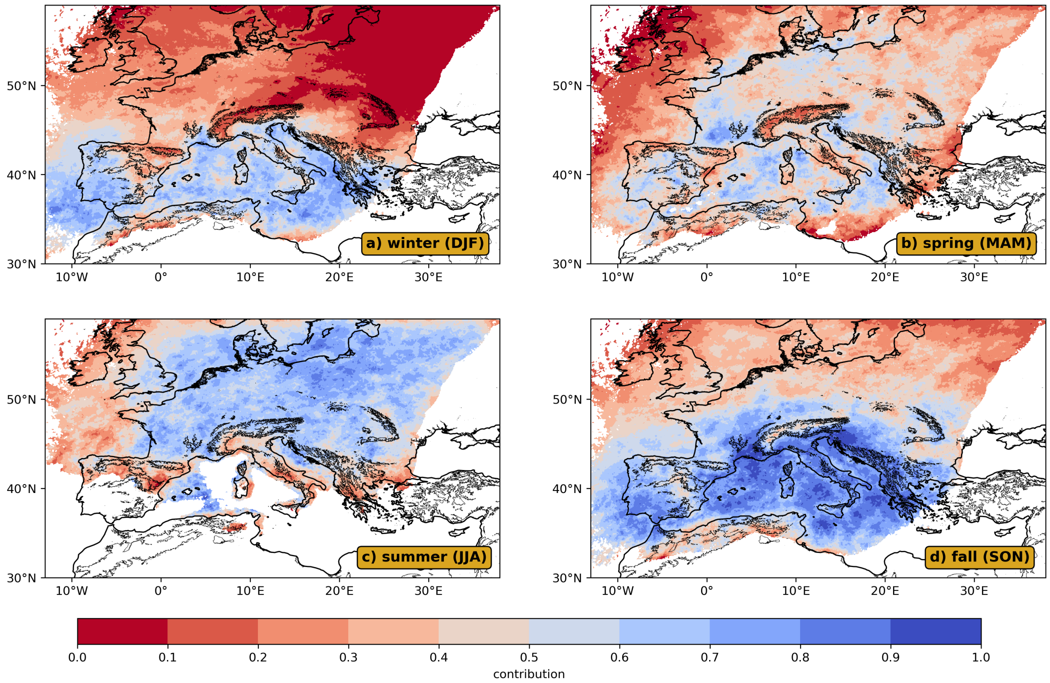

Figure 8. Contribution of MCS to the precipitation features producing the 10% most extreme precipitation accumulations (as defined in section 3.4) over Europe in winter (DJF, a), spring (MAM, b), summer (JJA, c) and fall (SON, d).

Summing up, MCS generally dominate precipitation accumulation extremes over most of Europe, with only northern Europe during winter constituting an exception.

3.5 Diurnal cycle — large contrasts between coasts and continents

Often poorly represented by numerical models (Brockhaus et al., 2008), the diurnal cycle of precipitation is of key mechanistic and practical relevance. For each of the sub-regions (Fig. 3) and each month, we compute the diurnal cycle of the expected value of MCS precipitation given the occurrence of a MCS in the sub-region at any time of the day. In detail, we collect the MCS precipitation intersecting the sub-region, average over the sub-region, and stratify by local solar time (LST) 1-h bins. For each MCS affecting the sub-region, to ensure an equal number of samples per LST bins and thus a fair estimation of the MCS precipitation conditional probability, we complete each bins by zeros. For each bin, we finally calculate the MCS averaged precipitation and select the months of peak MCS activity according to the monthly number distribution shown in Fig. 4.

3.5.1 Large inter-month and inter-regional variability in coastal regions.

For the coastal sub-regions (BS, ENS, AO, IS, LTS and AIS) the diurnal cycle of MCS precipitation varies strongly between sub-regions and seasons. Some sub-regions (BS in June, July, October; ENS in November; AO in February; IS in October, November, and December) exhibit afternoon peaks of MCS precipitation, which are likely associated with continental convection. We however note that the amplitude of these peaks is not commensurate with the amplitude of the solar diurnal cycle, e.g., IS experiences the strongest afternoon peak of MCS precipitation during the month with the least diurnal variation in solar irradiance of the year (December). A number of sub-regions (BS in October; ENS from September to December; AO in December and January; IS in October and November; LTS in September, October and December; AIS in February) exhibit a nocturnal/early morning peak, reminiscent of the total precipitation diurnal cycle over most sea areas (Dai, 2001; Bowman et al., 2005; Tan et al., 2019; Watters & Battaglia, 2019). We note that this peak is not systematic and depends on the region, the month and type of precipitation (Figs S12, S13, S14).

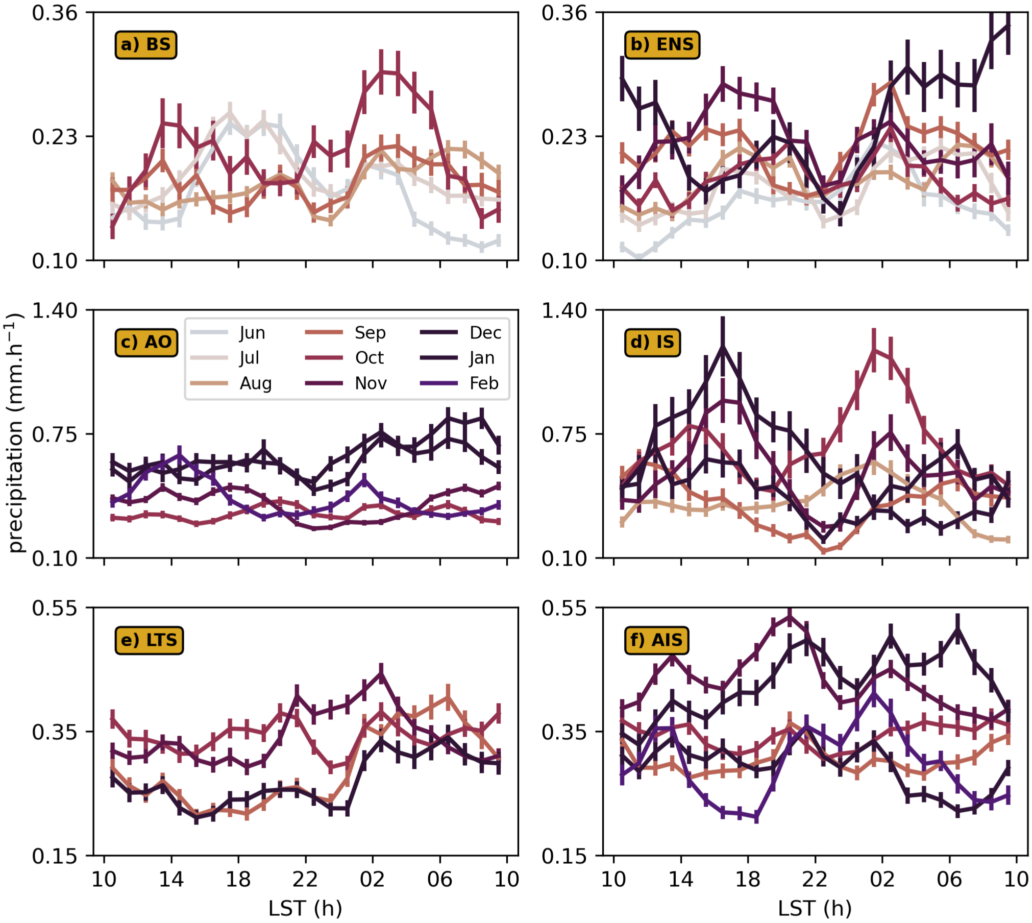

Figure 9. Monthly expected values of MCS precipitation (in mm.h^{-1}) conditioned on MCS occurrence within the coastal sub-regions as a function of LST (in h): BS (a), ENS (b), AO (c), IS (d), LTS (e) and AIS (f) (see Fig. 3). Results are given for months with the main MCS activity according to Fig. 4. For each LST bin the standard error is calculated to estimate the uncertainty in the mean and represented by error bars.

3.5.2 Nocturnal peaks in continental regions

The diurnal cycle analysis was repeated for the continental sub-regions for May to October (Fig. 10). There, a generally more pronounced MCS diurnal cycle is found, exhibiting reduced inter-month variability compared to the coastal areas. In the four continental sub-regions there is a strong late-afternoon peak of MCS precipitation from May to August. This peak is most pronounced during July over ALP and BC, whereas it is more marked in May in GHP and NC. We note that this peak tends to occur later (around 20 LST) in the lee of the Alps (in GHP) and the lee of the Carpathians (in NC), compared to the Alps and the Baltic plains (BC; around 18 LST). This characteristic may be explained by propagating systems from the mountains to the plains occurring later in the evening. Similarly, convective precipitation tends to peak earlier in the afternoon than MCS (Fig. S17), consistent with the time required for the upscale growth of MCS. Generally weaker diurnal ranges of MCS precipitation are observed during September and October (as observed for total precipitation in Mandapaka et al. (2013); Alber et al. (2015)).

Interestingly, for the GHP sub-region, the diurnal cycle of MCS precipitation exhibits another systematic peak (at around 3 LST). This nocturnal peak becomes more and more pronounced when moving from May to October, as opposed to the late afternoon peak, which diminishes in the course of this seasonal period. A secondary nocturnal peak also appears for the other continental sub-regions, even though it is less pronounced and systematic. One could argue that the nocturnal MCS precipitation peak in GHP might be related to the Adriatic Sea diurnal cycle, "leaking" into GHP at nighttime as a result of a southwesterly flow. However, as seen in Fig. 9g and Fig. S12g, there is no evidence for a clear evening or nocturnal peak in both MCS and isolated convective precipitation for AIS during these months, suggesting a local enhancement/development of MCS precipitation during the night in GHP. We further note that the nocturnal peak is generally less pronounced or does not appear in isolated convective precipitation, as well as for lightning (Fig. S15, S16 and S17). Levizzani et al. (2010) evidenced a slight nocturnal peak of cold cloud frequency in August over similar longitudes, mentioning a potential role of the Carpathians in enhancing precipitating systems. Twardosz (2007) analyzed the diurnal cycle of precipitation over southern Poland conditional on different circulation types and noted a nocturnal/early morning peak of precipitation associated with warm fronts in southerly/southwesterly flows. It is however uncertain whether nocturnal MCS in this region are regularly embedded within a warm front, when warm fronts are usually associated to less convectively unstable environments (as noted in Twardosz (2010)). The precise origin of MCS nocturnal precipitation peaks over continental areas remains thus uncertain and requires further studies.

4 Understanding the spatio-temporal distribution of European MCS

It was found that MCS often develop near frontal boundaries which provide dynamical lifting over large scales (e.g. Maddox (1983)). Here, we estimate the frontal activity by using the method of Parfitt et al. (2017) to identify fronts in the middle troposphere (600 hPa; to avoid the detection of low level breeze fronts), and define fronts as contiguous frontal pixels with a horizontal extent of at least 300 km. To only select synoptic fronts from low pressure systems, we discard every fronts containing less than 4 ERA5 pixels with a low pressure and a low geopotential height at 500 hPa (defined as a negative anomaly from a 2000-2020 climatology). By calculating the frequency of frontal pixels as a function of the distance from a PF at the time of their largest extent (Fig. S18), we find that MCS are more tightly connected to the presence of a frontal boundary at few hundreds of km from their center than for isolated convective and stratiform PFs. Among these fronts, the contribution of cold fronts is the most important by a factor of two compared to warm fronts (not shown).

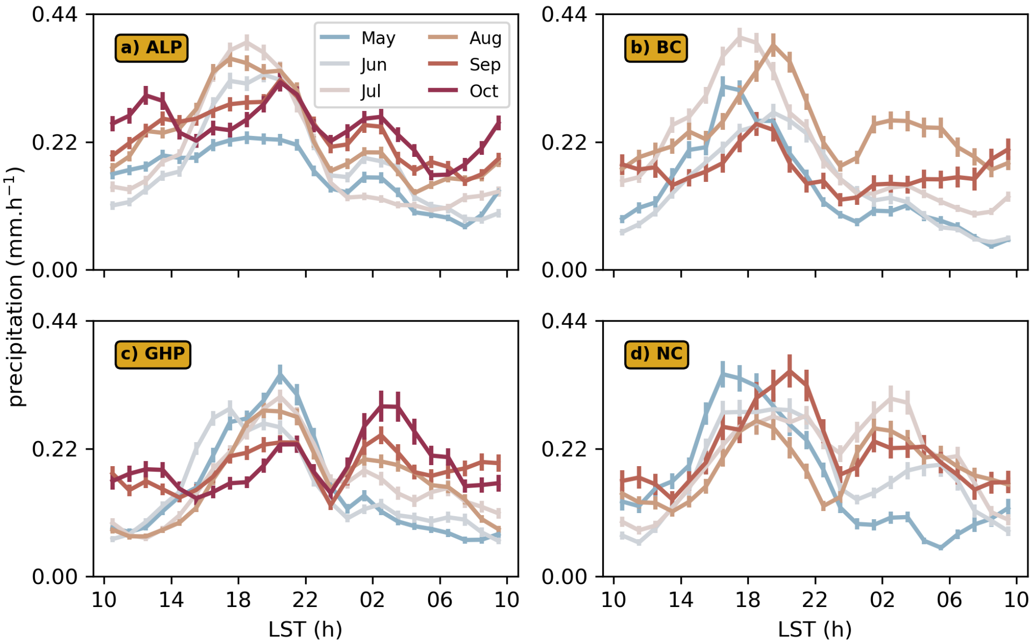

Figure 10. Similar as Fig. 9 but for the continental sub-regions: ALP (a), BC (b), GHP (c) and NC (d) (see Fig. 3).

In the remainder of this section, we analyze the MCS precipitation annual cycle for the different sub-regions (Fig. 3) in relation to the SST (or land 2-m temperatures for continental sub-regions), the frequency of significant CAPE, and frontal occurrence. CAPE is considered as significant when it exceeds a threshold of 100 J.kg^{-1} (consistently with fig. S2). We evaluate frontal occurrence as follows: for each pixel within each sub-region we count the number of times a front occurred over each month. If a pixel is part of two fronts that are separated within less than a three-hour interval, it is assumed that it is the same front. This front occurrence frequency is then averaged over the box and the 16 years.

4.1 Coastal drivers: dynamics.

In all coastal locations, SSTs generally peak in August, as does CAPE. For the northern coasts of Europe, BS and ENS, these peaks coincide with that of MCS precipitation, suggesting that convective instability might play a determining role in MCS precipitation there. This applies particularly to BS, where the rapid SST decrease after August is accompanied by a rapid decay of CAPE. For ENS the drop in SSTs is more gradual, limiting the decay of CAPE in fall. This, associated with increased frontal activity, may extend the MCS precipitation peak until November in ENS. For all remaining coastal regions the MCS precipitation peak is delayed relative to the August SST and CAPE peaks: November for the Mediterranean coasts (LTS and AIS), October for IS and December for AO. Unlike BS and ENS, these regions experience higher SSTs in August that decrease progressively during fall, hence these regions might be less limited by CAPE availability in fall. Rather, despite the larger summertime CAPE, the lack of triggering and organizing large scale patterns, such as fronts, may be limiting factors in these regions during summer. Across sub-regions, we attribute the decrease in MCS activity in winter or early spring to CAPE limitations.

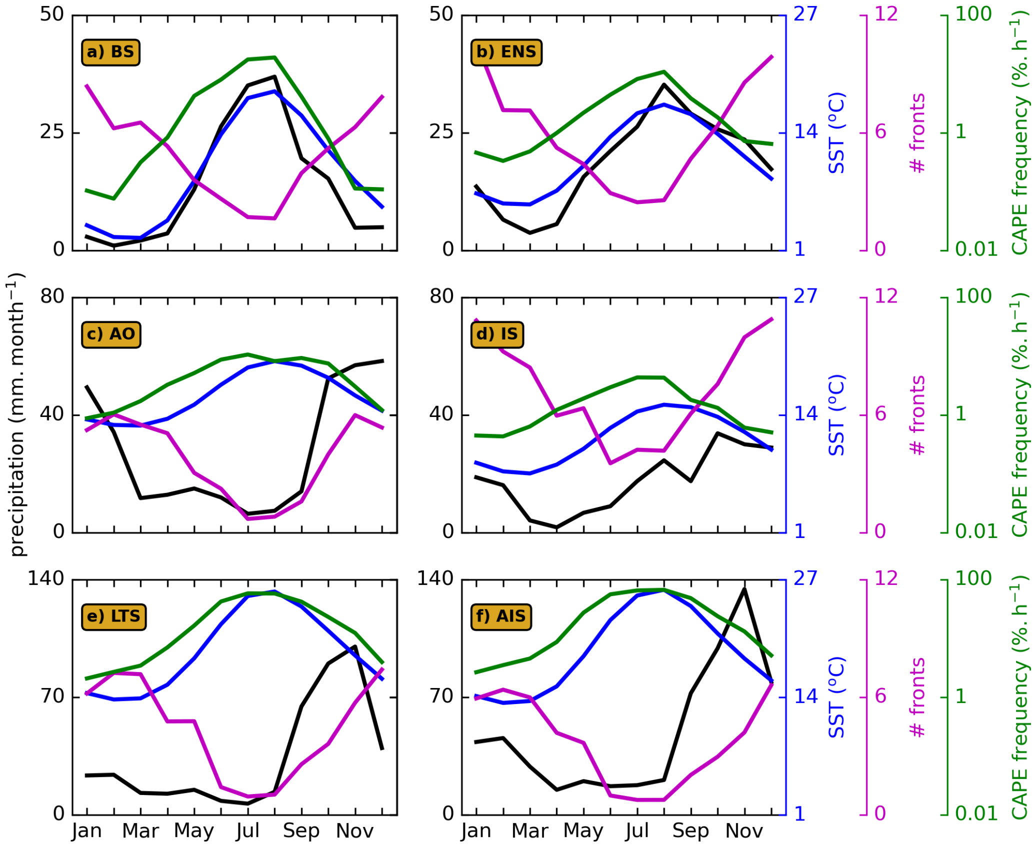

Figure 11. Averaged monthly time series of IMERG MCS precipitation amounts (in mm.month^{-1}, black), ERA-5 Sea Surface Temperature (SST, in degrees, blue), number of fronts (magenta), and Convective Available Potential Energy (CAPE) frequency (defined in section 4; in %.h^{-1}, green; note the logarithmic scale) for the coastal sub-regions: BS (a), ENS (b), AO (c), IS (d), LTS (e) and AIS (f) (see Fig. 3).

4.2 Continental drivers: thermodynamics.

In contrast to the coastal regions, for land regions MCS precipitation peaks generally coincide with the peaks in surface temperature, i.e., July for BC and NC and August for ALP and GHP, despite a relatively low front frequency, suggesting a more thermodynamic control. We interpret this as resulting from land surfaces often constituting topographic boundaries that force large-scale convection without the need for an air mass boundary. We note that CAPE frequency maxima generally occurs slightly earlier in the year (typically in July). ALP and GHP show a long tail in the fall months despite thermodynamic and instability conditions deteriorating. These might be related to Mediterranean unstable air masses that are advected towards the Alps and Balkans, and eventually leading to MCS formation by topographic lifting or MCS advection.

5 Conclusions

We have characterized mesoscale convective systems (MCS) over Europe by building a long-term MCS climatology (16 years) at high spatial resolution (0.1°). MCS are identified by detecting and tracking precipitation features using the recent IMERG satellite-

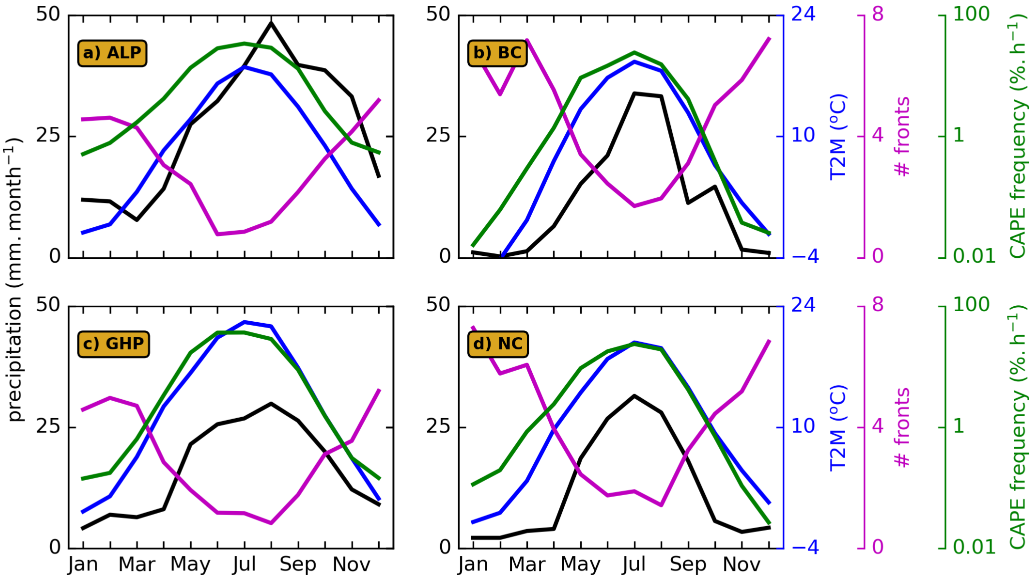

Figure 12. Similar as Fig. 11 but for the continental sub-regions: ALP (a), BC (b), GHP (c) and NC (d) (see Fig. 3).

based dataset and conditioning on lightning data from the EUCLID dataset. MCS are abundant and responsible for substantial precipitation totals in all seasons. In fall and winter, MCS are mainly concentrated over the Mediterranean and the Atlantic coasts, whereas in summer, MCS mainly affect continental Europe, especially mountainous regions, and the northern seas. Spring is transitionary, with MCS activity moving inland and pole-ward.

The contribution of MCS to total rainfall peaks over the Mediterranean during fall, exceeding 70% over large areas. While many other regions are also significantly affected by stratiform precipitation from extratropical cyclones, the MCS contribution often reaches similar amplitudes over the hotspot regions. Concerning extremes, MCS contribute even more strongly, exceeding 90% in the Mediterranean in fall and 70% over northern Europe in summer.

The diurnal cycle of MCS precipitation over coastal areas exhibits large inter-month and inter-regional variability, far from a systematic nocturnal/early morning maximum expected from the climatology (Watters & Battaglia, 2019), and suggesting that local mechanisms are involved. The MCS precipitation diurnal cycle over the selected continental sub-regions shows a more pronounced and systematic diurnal cycle during the warmest months of the year. For these months we find a late afternoon/evening peak for MCS, following the afternoon peak of isolated convective. In some of the locations (particularly in the Great Hungarian Plains in early fall), we find an additional nocturnal maximum, despite reduced convective instability. The exact origin of this striking feature remains unclear and begs for further investigation, such as through high-resolution simulation case studies.

We then analyze the MCS annual cycle and associated variables, finding that, across sub-regions, convective instability peaks in summer whereas frontal activity, for which we found an overall strong involvement in MCS activity, peaks in the winter. Two main features stick out:

- In sub-regions where convective instability is a limiting factor and decreases rapidly from summer to fall, MCS precipitation peaks concomitantly with the peak of convective instability and surface temperature. This is the case for the continental regions and the Baltic and North Seas.
- In sub-regions where the convective instability has a more gradual decrease or remains significant in fall, MCS precipitation tends to peak in fall. We further attribute this delay to more favorable dynamical conditions, namely more pronounced frontal activity and larger boundary layer lapse rates. This is the case of the large water bodies of high-heat capacity, for which the decrease of SSTs during fall is slower. Whereas MCS do occasionally occur in these regions, the lack of dynamical forcing appears as a limiting factor during summer compared to fall.

In summary, this study highlights the significant role of MCS in driving total, and in particular extreme, rainfall in Europe. We advocate studies unveiling the mechanisms leading to extreme MCS rainfall and their local characteristics, such as the nocturnal MCS rainfall enhancement over eastern Europe, diurnal cycle variability in coastal regions, and the role of the topography, microphysics, and radiation. Such studies could combine higher resolution precipitation datasets, e.g., radar, with numerical simulations to explore local effects. Such endeavors may ultimately lead to a better causal understanding and thus improved forecasting of mid-latitude MCS rainfall extremes.

6 Open Research

ERA5 reanalysis data were downloaded from `https://doi.org/10.24381/cds.bd0915c6` and `https://doi.org/10.24381/cds.adbb2d47`. The IMERG precipitation product was downloaded from `https://doi.org/10.5067/GPM/IMERG/3B-HH/06` (Huffman et al., 2019). The surface synoptic observation (SYNOP; O'Brien (2008)) was downloaded from `https://catalogue.ceda.ac.uk/uuid/9f80d42106ba708f92ada730ba321831`. The EUCLID data are available upon request from `https://www.euclid.org/#`. Topography data were supplied by the GEBCO Compilation Group (2022) GEBCO_2022 Grid (doi:10.5285/e0f0bb80-ab44-2739-e053-6c86abc0289c).

Acknowledgments

The authors gratefully acknowledge funding by the European Research Council (ERC) under the European Union's Horizon 2020 research and innovation program (grant number: 771859). JOH further acknowledges funding by a grant from the VILLUM Foundation (grant number: 13168) and the Novo Nordisk Foundation Interdisciplinary Synergy Program (grant no. NNF19OC0057374).

References

Adler, R. F., Sapiano, M. R., Huffman, G. J., Wang, J.-J., Gu, G., Bolvin, D., ... others (2018). The global precipitation climatology project (gpcp) monthly analysis (new version 2.3) and a review of 2017 global precipitation. *Atmosphere*, *9*(4), 138. doi: 10.3390/atmos9040138

Alber, R., Jaagus, J., & Oja, P. (2015). Diurnal cycle of precipitation in estonia. *Estonian Journal of Earth Sciences*, *64*(4), 305. doi: 10.3176/earth.2015.36

Berg, P., & Haerter, J. (2013). Unexpected increase in precipitation intensity with temperature—a result of mixing of precipitation types? *Atmospheric Research*, *119*, 56–61.

Bowman, K. P., Collier, J. C., North, G. R., Wu, Q., Ha, E., & Hardin, J. (2005). Diurnal cycle of tropical precipitation in tropical rainfall measuring mission (trmm) satellite and ocean buoy rain gauge data. *Journal of Geophysical Research: Atmospheres*, *110*(D21). doi: 10.1029/2005JD005763

Brockhaus, P., Luthi, D., & Schar, C. (2008). Aspects of the diurnal cycle in a regional climate model. *Meteorologische Zeitschrift*, *17*(4), 433–444. doi: 10.1127/0941-2948/2008/0316

Cheeks, S. M., Fueglistaler, S., & Garner, S. T. (2020). A satellite-based climatology of central and southeastern u.s. mesoscale convective systems. *Monthly Weather Review*, *148*(6), 2607 - 2621. doi: 10.1175/MWR-D-20-0027.1

Cui, W., Dong, X., Xi, B., Feng, Z., & Fan, J. (2020). Can the gpm imerg final product accurately represent mcss' precipitation characteristics over the central and eastern united states? *Journal of Hydrometeorology*, *21*(1), 39 - 57. doi: 10.1175/JHM-D-19-0123.1

Dai, A. (2001). Global precipitation and thunderstorm frequencies. part ii: Diurnal variations. *Journal of Climate*, *14*(6), 1112 - 1128. doi: 10.1175/1520-0442(2001)014⟨1112:GPATFP⟩2.0.CO;2

Da Silva, N. A., Muller, C., Shamekh, S., & Fildier, B. (2021). Significant amplification of instantaneous extreme precipitation with convective self-aggregation. *Journal of Advances in Modeling Earth Systems*, *13*(11), e2021MS002607. (e2021MS002607 2021MS002607) doi: https://doi.org/10.1029/2021MS002607

Feng, Z., Leung, L. R., Liu, N., Wang, J., Houze Jr, R. A., Li, J., ... Guo, J. (2021). A global high-resolution mesoscale convective system database using satellite-derived cloud tops, surface precipitation, and tracking. *J. Geophys. Res.*, *126*(8), e2020JD034202. doi: 10.1029/2020JD034202

Fowler, H. J., Lenderink, G., Prein, A. F., Westra, S., Allan, R. P., Ban, N., ... others (2021). Anthropogenic intensification of short-duration rainfall extremes. *Nature Reviews Earth & Environment*, *2*(2), 107–122.

García-Herrera, R., Hernández, E., Paredes, D., Barriopedro, D., Correoso, J. F., & Prieto, L. (2005). A mascotte-based characterization of mcss over spain, 2000–2002. *Atmospheric Research*, *73*(3-4), 261–282.

Geerts, B., Parsons, D., Ziegler, C. L., Weckwerth, T. M., Biggerstaff, M. I., Clark, R. D., ... Wurman, J. (2017). The 2015 plains elevated convection at night field project. *Bulletin of the American Meteorological Society*, *98*(4), 767 - 786. doi: 10.1175/BAMS-D-15-00257.1

Haberlie, A. M., & Ashley, W. S. (2019). A radar-based climatology of mesoscale convective systems in the united states. *Journal of Climate*, *32*(5), 1591 - 1606. doi: 10.1175/JCLI-D-18-0559.1

Haerter, J. O., & Schlemmer, L. (2018). Intensified cold pool dynamics under stronger surface heating. *Geophysical Research Letters*, *45*(12), 6299-6310. doi: 10.1029/2017GL076874

Hersbach, H., Bell, B., Berrisford, P., Hirahara, S., Horányi, A., Muñoz-Sabater, J., ... Thépaut, J.-N. (2020). The era5 global reanalysis. *Quarterly Journal of the Royal Meteorological Society*, *146*(730), 1999-2049. doi: 10.1002/qj.3803

Houze, J., & Robert, A. (2012). Orographic effects on precipitating clouds. *Reviews of Geophysics*, *50*(1). doi: 10.1029/2011RG000365

Houze, R. A. (2018). 100 years of research on mesoscale convective systems. *Meteor. Monogr.*, *59*, 17.1 - 17.54. doi: 10.1175/AMSMONOGRAPHS-D-18-0001.1

Huffman, G. J., Stocker, E. F., Bolvin, D. T., Nelkin, E. J., & Tan, J. (2019). Gpm imerg final precipitation l3 half hourly 0.1 degree x 0.1 degree v06. *Goddard Earth Sciences Data and Information Services Center (GES DISC), Accessed: 1st August 2021.*. doi: 10.5067/GPM/IMERG/3B-HH/06

Jirak, I. L., & Cotton, W. R. (2007). Observational analysis of the predictability of mesoscale convective systems. *Weather and Forecasting*, *22*(4), 813 - 838. doi: 10.1175/WAF1012.1

Jirak, I. L., Cotton, W. R., & McAnelly, R. L. (2003). Satellite and radar survey of mesoscale convective system development. *Mon. Wea. Rev.*, *131*(10), 2428 - 2449. doi: 10.1175/1520-0493(2003)131⟨2428:SARSOM⟩2.0.CO;2

Kolios, S., & Feidas, H. (2010). A warm season climatology of mesoscale convective systems in the mediterranean basin using satellite data. *Theoretical and applied climatology*, *102*(1), 29–42.

Laing, A. G., & Fritsch, M. (1997). The global population of mesoscale convective complexes. *Quart. J. Roy. Meteor. Soc.*, *123*(538), 389-405. doi: 10.1002/qj.49712353807

Levizzani, V., Pinelli, F., Pasqui, M., Melani, S., Laing, A. G., & Carbone, R. E. (2010). A 10-year climatology of warm-season cloud patterns over europe and the mediterranean from meteosat ir observations. *Atmospheric Research*, *97*(4), 555-576. (From the Lab to Models and Global Observations: Hans R. Pruppacher and Cloud Physics) doi: 10.1016/j.atmosres.2010.05.014

Li, P., Moseley, C., Prein, A. F., Chen, H., Li, J., Furtado, K., & Zhou, T. (2020). Mesoscale convective system precipitation characteristics over east asia. part i: Regional differences and seasonal variations. *Journal of Climate*, *33*(21), 9271–9286.

Liu, C., & Zipser, E. J. (2015). The global distribution of largest, deepest, and most intense precipitation systems. *Geophysical Research Letters*, *42*(9), 3591-3595. doi: 10.1002/2015GL063776

Luo, L., Xue, M., & Zhu, K. (2020). The initiation and organization of a severe hail-producing mesoscale convective system in east china: A numerical study. *J. Geophys. Res.*, *125*(17), e2020JD032606. (e2020JD032606 2020JD032606) doi: 10.1029/2020JD032606

Maddox, R. A. (1983). Large-scale meteorological conditions associated with midlatitude, mesoscale convective complexes. *Monthly Weather Review*, *111*(7), 1475 - 1493. doi: 10.1175/1520-0493(1983)111⟨1475:LSMCAW⟩2.0.CO;2

Mandapaka, P. V., Germann, U., & Panziera, L. (2013). Diurnal cycle of precipitation over complex alpine orography: inferences from high-resolution radar observations. *Quarterly Journal of the Royal Meteorological Society*, *139*(673), 1025-1046. doi: 10.1002/qj.2013

Mathias, L., Ermert, V., Kelemen, F. D., Ludwig, P., & Pinto, J. G. (2017). Synoptic analysis and hindcast of an intense bow echo in western europe: The 9 june 2014 storm. *Weather and Forecasting*, *32*(3), 1121 - 1141. doi: 10.1175/WAF-D-16-0192.1

Morel, C., & Senesi, S. (2002). A climatology of mesoscale convective systems over europe using satellite infrared imagery. ii: Characteristics of european mesoscale convective systems. *Quart. J. Roy. Meteor. Soc.*, *128*(584), 1973-1995. doi: 10.1256/003590002320603494

Moseley, C., Berg, P., & Haerter, J. O. (2013). Probing the precipitation life cycle by iterative rain cell tracking. *Journal of Geophysical Research: Atmospheres*, *118*(24), 13,361-13,370. doi: 10.1002/2013JD020868

Moseley, C., Henneberg, O., & Haerter, J. O. (2019). A statistical model for isolated convective precipitation events. *Journal of Advances in Modeling Earth Systems*, *11*(1), 360-375. doi: 10.1029/2018MS001383

Nesbitt, S. W., Cifelli, R., & Rutledge, S. A. (2006). Storm morphology and rainfall characteristics of trmm precipitation features. *Mon. Wea. Rev.*, *134*(10), 2702 - 2721. doi: 10.1175/MWR3200.1

O'Brien, C. (2008). *Met office (2008): Land synop reports from land stations collected by the met office metdb system.* `https://catalogue.ceda.ac.uk/uuid/9f80d42106ba708f92ada730ba321831`. (Online; accessed 21 October 2021)

Parfitt, R., Czaja, A., & Seo, H. (2017). A simple diagnostic for the detection of atmospheric fronts. *Geophysical Research Letters*, *44*(9), 4351-4358. doi: https://doi.org/10.1002/2017GL073662

Parker, M. D. (2008). Response of simulated squall lines to low-level cooling. *Journal of the Atmospheric Sciences*, *65*(4), 1323 - 1341. doi: 10.1175/2007JAS2507.1

Pitchford, K. L., & London, J. (1962). The low-level jet as related to nocturnal thunderstorms over midwest united states. *Journal of Applied Meteorology and Climatology*, *1*(1), 43 - 47. doi: 10.1175/1520-0450(1962)001⟨0043:TLLJAR⟩2.0.CO;2

Poelman, D. R., Schulz, W., Diendorfer, G., & Bernardi, M. (2016). The european lightning location system euclid – part 2: Observations. *Natural Hazards and Earth System Sciences*, *16*(2), 607–616. doi: 10.5194/nhess-16-607-2016

Punkka, A.-J., & Bister, M. (2015). Mesoscale convective systems and their synoptic-scale environment in finland. *Weather and Forecasting*, *30*(1), 182 - 196. doi: 10.1175/WAF-D-13-00146.1

Rigo, T., Berenguer, M., & del Carmen Llasat, M. (2019). An improved analysis of mesoscale convective systems in the western mediterranean using weather radar. *Atmospheric research*, *227*, 147–156.

Salio, P., Nicolini, M., & Zipser, E. J. (2007). Mesoscale convective systems over southeastern south america and their relationship with the south american low-level jet. *Monthly Weather Review*, *135*(4), 1290 - 1309. doi: 10.1175/MWR3305.1

Schulz, W., Diendorfer, G., Pedeboy, S., & Poelman, D. R. (2016). The european lightning location system euclid – part 1: Performance analysis and validation. *Natural Hazards and Earth System Sciences*, *16*(2), 595–605. doi: 10.5194/nhess-16-595-2016

Schumacher, R., & Johnson, R. H. (2005). Organization and environmental properties of extreme-rain-producing mesoscale convective systems. *Mon. Wea. Rev.*, *133*(4), 961 - 976. doi: 10.1175/MWR2899.1

Schumacher, R., & Rasmussen, K. (2020). The formation, character and changing nature of mesoscale convective systems. *Nat. Rev. Earth Environ.*, *1*, 300–314. doi: 10.1038/s43017-020-0057-7

Surowiecki, A., & Taszarek, M. (2020). A 10-year radar-based climatology of mesoscale convective system archetypes and derechos in poland. *Monthly Weather Review*, *148*(8), 3471 - 3488. doi: 10.1175/MWR-D-19-0412.1

Tan, J., Huffman, G. J., Bolvin, D. T., & Nelkin, E. J. (2019). Diurnal cycle of imerg v06 precipitation. *Geophysical Research Letters*, *46*(22), 13584-13592. doi: 10.1029/2019GL085395

Tan, J., Jakob, C., Rossow, W. B., & Tselioudis, G. (2015). Increases in tropical rainfall driven by changes in frequency of organized deep convection. *Nature*, *519*(7544), 451–454. doi: https://doi.org/10.1038/nature14339

Taszarek, M., Allen, J., Púčik, T., Groenemeijer, P., Czernecki, B., Kolendowicz, L., ... Schulz, W. (2019). A climatology of thunderstorms across europe from a synthesis of multiple data sources. *Journal of Climate*, *32*(6), 1813 - 1837. doi: 10.1175/JCLI-D-18-0372.1

Twardosz, R. (2007). Diurnal variation of precipitation frequency in the warm half

of the year according to circulation types in kraków, south poland. *Theoretical and Applied Climatology*, *89*, 229–238. doi: 10.1007/s00704-006-0268-y
Twardosz, R. (2010). A synoptic analysis of the diurnal cycle of thunderstorm precipitation in kraków (southern poland). *International Journal of Climatology*, *30*(7), 1008-1013. doi: 10.1002/joc.1960
Watters, D., & Battaglia, A. (2019). The summertime diurnal cycle of precipitation derived from imerg. *Remote Sensing*, *11*(15). doi: 10.3390/rs11151781

The characteristics of mesoscale convective system rainfall over Europe

Nicolas A. Da Silva[1] and Jan O. Haerter[1,2,3]

[1]Complexity and Climate, Leibniz Centre for Tropical Marine Research, Fahrenheitstrasse 6, 28359 Bremen, Germany.
[2]Physics and Earth Sciences, Constructor University Bremen, Campus Ring 1, 28759 Bremen, Germany.
[3]Niels Bohr Institute, University of Copenhagen, Blegdamsvej 17, 2100 Copenhagen, Denmark.

Key Points:

- MCS substantially contribute to precipitation totals and dominate event-based rainfall extremes over Europe.
- MCS's diurnal cycle displays a large variability over the coasts and may exhibit nocturnal peaks over continental areas.
- The yearly cycle of MCS rainfall is understood with the yearly cycle of surface temperature, convective instability, and frontal activity.

Corresponding author: Nicolas A. Da Silva, nicolas.da-silva@leibniz-zmt.de

Abstract

Mesoscale Convective Systems (MCS) are common over Europe and can produce severe weather, including extreme precipitation, which can lead to flash floods. The few studies analyzing the climatological characteristics of MCS over Europe are either based on only few years of data or focus on limited sub-areas. Using the recent Integrated Multi-satellitE Retrievals for Global Precipitation Measurement (IMERG) satellite precipitation climatology, we identify and track MCS for 16 years over Europe. We devise a spatial filter and track cells according to the overlap of filtered rain patches between consecutive time steps. By fitting an ellipse to these patches, we determine their overall shape and orientation. To distinguish convective rain patches we condition on lightning data, thus reducing potential identification errors. We analyze this new European MCS climatology to characterize MCS rainfall properties: MCS overall occur most frequently over the Mediterranean and Atlantic during fall and winter, whereas during summer, they concentrate over the continent. Typically, more than half of seasonal precipitation can be attributed to MCS, and their contribution to extreme precipitation is even greater, often exceeding 70%. MCS over the continent display a clear diurnal cycle peaking during the afternoon, and some continental areas even show a second, nocturnal peak. The MCS diurnal cycle for coastal and oceanic regions is more variable. Selecting sub-areas, we find that the spatio-temporal distribution of MCS precipitation throughout the year can be well explained by the spatio-temporal distribution of specific environmental variables, namely (sea) surface temperature, fronts occurrence and convective instability.

Plain Language Summary

Extreme rainfall events leading to flash floods have major socio-economical impacts over Europe. These events are often created by large and long-lived clusters of clouds called Mesoscale Convective Systems (MCS). Although these MCS are well known by the climate community, their rainfall characteristics over Europe are not fully documented. This is the purpose of this study. Here, we identify MCS by using satellite images (detecting rainfall) and lightning strikes for 16 years over Europe. We also develop a tracking algorithm, enabling us to follow each MCS in time and space. The recognition of individual MCS is based on the overlap of rainfall patches between two consecutive satellite images. We find that MCS overall occur most frequently over the Mediterranean and Atlantic during fall and winter, whereas during summer, they concentrate over the continent. We show that they substantially contribute to the yearly total rainfall over Europe. More remarkably, MCS is the most frequent cloud organization form responsible for extreme rainfall events over Europe. Thus, while the present study gives some general explanations on their main behavior, it is of critical importance to further understand European MCS and their potential changes in a warming climate.

1 Introduction

Mesoscale Convective Systems (MCS) are aggregates of cumulonimbus clouds spanning a few hundreds of kilometers horizontally (R. A. Houze, 2018). These organized weather systems are abundant over the tropics where they contribute to more than half of the total rainfall (Laing & Fritsch, 1997; Nesbitt et al., 2006; Liu & Zipser, 2015; Tan et al., 2015; Schumacher & Rasmussen, 2020; Feng et al., 2021). Despite the frequent occurrence of stratiform rainfall from extra-tropical cyclones in mid-latitudes, MCS are also a significant contributor to mid-latitude precipitation (Haberlie & Ashley, 2019; Feng et al., 2021), in particular during summer when thunderstorm activity is most pronounced (Taszarek et al., 2019) In addition to their significant impact on the hydrological cycle, MCS are often associated with severe weather such as heavy rainfall, large hail, strong winds, or tornadoes (Jirak et al., 2003; Mathias et al., 2017; Luo et al., 2020; Schumacher & Rasmussen, 2020; Fowler et al., 2021). In fact, MCS areas and rain intensities tend to be larger in mid-latitudes than in the tropics, possibly due to larger wind shear (Schumacher & Rasmussen, 2020). It is therefore important to understand the characteristics of mid-latitude MCS and how these may change with global change.

Several studies have focused on the climatological properties of MCS around the globe. In the USA, MCS preferentially occur in the Midwest during the warm season and in the mid-south during the cold season (Cui et al., 2020; Haberlie & Ashley, 2019). In the warm season, they were found to emerge along the eastern flank of the Rocky Mountains (Cheeks et al., 2020) in the late afternoon and subsequently propagate eastward, peaking at night in the central great plains (Geerts et al., 2017). It was suggested that the nocturnal MCS precipitation peak might be related to the peak in the Low Level Jet (LLJ, Pitchford and London (1962)) as well as both gravity waves (Parker, 2008) or potential vorticity anomalies (Jirak & Cotton, 2007) generated and advected away from the Rockies. A nocturnal peak in MCS precipitation was also observed in eastern China (Li et al., 2020) and Argentina (Salio et al., 2007). Both these regions have a mountain range in their western parts (Tibetan Plateau and Andes, respectively) and thus feature similar topographic characteristics as the midwest USA. Conversely, the varied European topography with several mountain ranges oriented along different directions might make for a more complex picture of the MCS diurnal cycle.

Focusing on a restricted part of Europe (García-Herrera et al., 2005; Punkka & Bister, 2015; Rigo et al., 2019; Surowiecki & Taszarek, 2020), investigating only one season (Morel & Senesi, 2002; Kolios & Feidas, 2010), or using a limited time record to assess climatological properties (Morel & Senesi, 2002; García-Herrera et al., 2005; Kolios & Feidas, 2010), several studies have examined MCS over Europe. Using five years of infrared (IR) satellite data, Morel and Senesi (2002) found that summer MCS (April-September) are more common over land than sea and are triggered near mountainous areas (Pyrenees, Alps, Carpathians) during the afternoon, a general characteristic also found for the USA.

The present study composes a comprehensive MCS rainfall climatology over Europe from 16 years of the Integrated Multi-satellitE Retrievals for GPM (IMERG) combined with EUropean Cooperation for LIghtning Detection (EUCLID) lightning data. MCS were often identified as large contiguous areas of low IR radiation emitted from cold convective anvils. While this approach is successful over the tropics, it may not be appropriate over mid-latitudes which are also subject to large frontal non-MCS systems that come with similarly low brightness temperatures. This is why more robust methods were recently developed for identifying MCS in the mid-latitudes (Feng et al., 2021), making use of the precipitation field to distinguish between convective and non convective systems, since convective cells generally produce more extreme rainfall rates than stratiform-type systems. However, since our objective is to investigate the relation between MCS and precipitation intensity, we adopt yet another, precipitation rate-independent, approach, which instead resorts to lightning strikes.

The present study thus aims at characterizing and understanding the hydrological "footprint" and the diurnal cycle of MCS precipitation over Europe. In Sec. 2, we describe the data sets exploited and how they are used to detect and track MCS. The contribution of MCS to both extreme and mean precipitation over Europe, as well as the MCS diurnal cycle, are characterized in Sec. 3. We then investigate the causes explaining the regional and seasonal differences of MCS precipitation (Sec. 4). Finally, we discuss our results and conclude (Sec. 5).

2 Data and tracking algorithm

Our method shares aspects with Feng et al. (2021) but primarily defines patches with the precipitation field instead of cloud top brightness temperatures and uses lightning data to distinguish convective patches.

2.1 Data

2.1.1 Integrated Multi-Satellite Retrievals (IMERG)

We identify precipitating features (PF) using the IMERG precipitation product, version V06B, from the Global Precipitation Measurement (GPM) project (Huffman et al., 2019). This product merges measurements from a constellation of satellites, carrying passive microwave (PM) and/or infrared (IR) sensors. While the PM sensors are generally more precise since they are directly measuring the signal alteration by precipitation droplets, their spatio-temporal coverage is limited. In contrast, IR sensors measure precipitation indirectly through cloud top brightness temperatures, but have a higher spatio-temporal resolution. The precipitation estimates from every satellite are inter-calibrated and combined to produce a half-hourly estimate of precipitation at 0.1^{o} of horizontal resolution which is monthly calibrated by the Global Precipitation Climatology Project (GPCP) satellite-gauge product (Adler et al., 2018).

2.1.2 European Cooperation for Lightning Detection (EUCLID)

To differentiate convective from stratiform weather systems, we employ the EUCLID lightning dataset (Schulz et al., 2016; Poelman et al., 2016). Only cloud to ground lightning strikes (CG) are used since they display spatio-temporal homogeneity from 2005 to 2020. The original dataset provides the number of CG in 30-minute time windows and on a $0.045^{o}\text{x}\,0.064^{o}$ grid covering most of Europe. We linearly interpolated the original lightning dataset to the IMERG grid ($0.1^{o}\text{x}\,0.1^{o}$) to achieve spatial coherence between both datasets.

2.1.3 General Bathymetric Chart of the Oceans (GEBCO)

Since mountain ranges were found to play an important role in the genesis of MCS in mid-latitudes (Morel & Senesi, 2002; Cheeks et al., 2020), we also make use of the GEBCO topography dataset.

2.1.4 ERA5

Several variables (SST; 2-m and 600 hPa temperatures; 600 hPa zonal and meridional wind speed; Convective Available Potential Energy (CAPE)) from the ERA5 global reanalysis product (Hersbach et al., 2020) are used to provide insights on the processes involved explaining the spatio-temporal distribution of MCS over Europe (in section 4).

2.2 MCS tracking algorithm

Detecting precipitation features and tracks. Similar to Feng et al. (2021), we first apply a spatial filter of 0.3^{o} to IMERG precipitation (Fig. 1ab), in order to define coherent PF that are not simply an artifact resulting from noise, and allow for "gaps" of a few tens of km to in the precipitation pattern of a PF. The PF are defined as contiguous patterns (when considering the four nearest neighbors on the regular longitude-latitude IMERG grid) of filtered precipitation above $2\,\text{mm.h}^{-1}$ (red contours in Fig. 1b). Other thresholds ($0.5\,\text{mm.h}^{-1}$, $1\,\text{mm.h}^{-1}$, $3\,\text{mm.h}^{-1}$ and $4\,\text{mm.h}^{-1}$) were tested and $2\,\text{mm.h}^{-1}$ was found to give the best compromise in order to discard many weak and sporadic systems that increase computational cost while preserving the main spatial patterns of the most significant systems.

All PFs are labeled at each time step as follows: when a PF spatially overlaps with another PF at the previous time step, it receives the same identification number (IN). Under strong wind conditions, it might occur that the area covered by one precipitation system does not overlap with the area covered by the same precipitation system 30 minutes earlier (especially for small systems). To limit identification errors related to these occurrences, we adopt the iterative strategy of Moseley et al. (2013) computing the mean displacement of all neighboring PFs within a 1000 km radius around a non-overlapping PF, then translating the non-overlapping PF backward in time with the resulted displacement vector, and searching for overlap in the corresponding new position. We perform this procedure for every non overlapping PFs and iterate until not any new overlap is found and not any new neighboring PF is found.

If a PF (e.g. Fig. 1d) spatially overlaps with several PFs at the previous time step (e.g. Fig. 1e), the IN of the PF that has the largest overlap is chosen for the new PF (merging case). A PF receives a new IN when it does not overlap with any PF at the previous time step. Conversely, if two new PFs (e.g. Fig. 1e) overlap with the same PF at the previous time step (e.g. Fig. 1d), the new PF that has the largest overlap with the old PF keeps its IN while the other new PF gets a new IN (splitting case). These choices correspond to the case of $\theta = 1$ in the method proposed by Moseley et al. (2019) to address splitting and merging cases.

In order to define shape properties, such as diameter, orientation, and eccentricity, we then fit an ellipse to each PF and at each time step. The fitting algorithm minimizes the sum of the distances between the contours of the PF and the ellipse in a least square sense (see Fig. 1c). In this algorithm, the area of the ellipse is set to be equal to the area of the PF and the center of the ellipse is fixed to the geometric center of the PF (red point in Fig. 1bc). The goodness of the ellipse fit (G) is defined as follows:

$$G = 1 - \frac{A_{ell,out} + A_{PF,out}}{A_{ell} + A_{PF}} = 1 - \frac{A_{ell,out}}{A_{PF}}\,, \tag{1}$$

where $\mathrm{A_{PF}} = \mathrm{A_{ell}}$ is the areas of the PF (defined as the sum of the pixel areas belonging to the PF) and ellipse, $\mathrm{A_{ell,out}}$ is the ellipse area outside of the PF, and $\mathrm{A_{PF,out}}$ the PF area outside of the ellipse. The probability density function (PDF) of G is displayed in Figure S1a. It shows that most of the PFs are well fitted by the ellipse with G values mostly ranging from 0.6 and 1 (99.5% of the PFs). The maximum of G occurrence is at around 0.95, which corresponds to the average value of G obtained for the ellipse fitting of small area PFs containing few pixels (Fig. S1b) and which are also the most frequent. The lowest values of G correspond to large area and complex PFs whose shapes can not be well represented by an ellipse.

Defining convective precipitation features and MCS. We now define convective and stratiform PFs by using the EUCLID lightning dataset regridded to match the IMERG grid. At any time of its "life cycle", a PF for which at least one CG was detected inside or in the vicinity (at a distance of less than 5 km) of its ellipse during the corresponding IMERG 30-minutes time window is defined as an "isolated convective PF". In this study, an MCS is a PF which experiences a diameter of at least 100 km for at least four consecutive hours during which at least one CG was detected at a distance of less than 5 km from its ellipse. Another approach, which makes use of ERA5 CAPE instead of lightning data (described in supplementary materials), was tested to define convective PFs and produced similar results for MCS (Figs S2, S3), showing that the MCS identification is robust. Here we choose to keep using the EUCLID lightning dataset as we believe that it provides a more direct detection of convective occurrence. Figure 2a is a snapshot of IMERG precipitation, EUCLID lightning strikes, and the objects detected by our algorithm on 9 June 2014 at 23h45 CEST, where intense MCS associated with severe

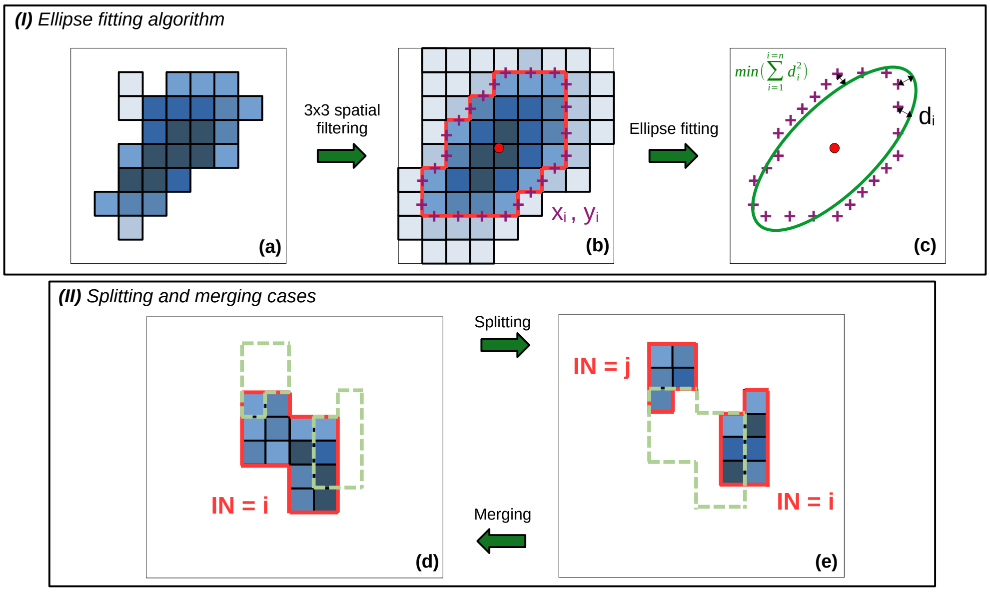

Figure 1. Scheme describing the PF identification (a,b), the ellipse fitting algorithm (c) and the treatment of splitting and merging (d,e) by our algorithm. First, the IMERG precipitation field (represented by blue pixels, with darker blue colors standing for more intense precipitation) is spatially filtered (a,b). Second, contours of filtered precipitation above 2 mm.h^{-1} are drawn (in red) to define PFs (b). The centers of the edges of the pixel contours (purple crosses) are used to fit an ellipse (in green) to each PF by minimizing the distance between the PF contours and the ellipse (c). The snapshots d and e represent two consecutive time steps for which the PF contours of the previous/next time step are reminded in light green dashed lines for an easier identification of the overlaps.

weather were observed in western Europe (Mathias et al., 2017). It shows a general good correspondence between the lightning strikes and the precipitating cells emerging from two different datasets, as well as fairly consistent ellipse fits to these objects. One can see that with the threshold approach, only the largest precipitating cells are detected by the algorithm.

For the analysis in the current work we retain unfiltered precipitation from the original IMERG grid. Since the PFs are defined using the spatial average of IMERG precipitation from 3x3 grid points, all of these unfiltered IMERG precipitation grid points contributing to the spatially filtered precipitation field of a particular PF are retained for this PF. This procedure may result in precipitation grid boxes belonging to two (or more) PF at the same moment. We have checked the PDFs with and without these repeated pixels and found that the differences are minor (not shown) and therefore retained this approach.

3 MCS climatology over Europe

3.1 Overall characteristics — MCS are more than a sum of stratiform and convective cells

With the algorithm described above, we were able to detect a total of 11,092 MCS from 2005 to 2020 (on average 693 per year) in our European domain (−13°W to 38°E, 30°N to 59°N; Fig. 3). To give an overview, Figure 2b shows the PDF of the duration

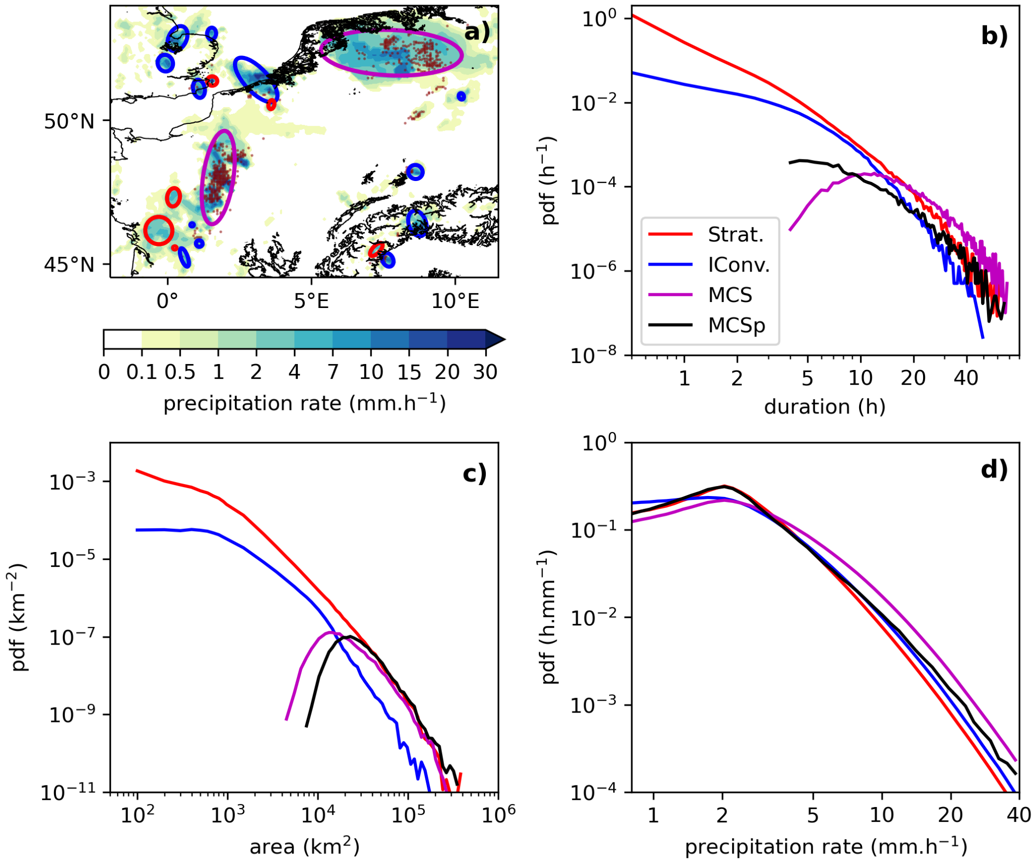

Figure 2. Snapshot of IMERG precipitation (shadings; in mm.$^{\text{h}}-1$) and EUCLID lightning strikes (dark red points) on 9th June 2014 at 23h45 CEST in western Europe (a). The ellipses represent the detected PF according to our algorithm presented in section 2: red for stratiform PF, blue for isolated convective PF, and magenta for MCS PF. Probability density functions (PDF) of precipitation features (PF) duration (b; in h), mean area (c; in km^2), and precipitation (d; in mm.h^{-1}) for stratiform ("Strat.", red), isolated convective ("IConv.", blue), MCS PF (magenta), and for MCS periods ("MCSp", black). MCSp was built by selecting only instants for which a MCS PF has MCS attributes (see section 3a). The PDF of duration and area were normalized by the the total number of PF while the PDF of precipitation were normalized by the number of instants of PF of the corresponding type (stratiform, isolated convective, MCS, or MCS periods).

of detected PF for the different types (stratiform, isolated convective, MCS). Since MCS are sometimes embedded in fronts, the duration of MCS PF can reach several days whereas the actual MCS activity may only last for few hours. To account for this potential difference, we also plot the PDF of MCS periods, defined as instants which are part of a four consecutive hours with diameter exceeding 100 km and for which a lightning strike was detected within these same 4 consecutive hours. For stratiform and isolated convective precipitation, the PDF monotonically decreases with PF duration. The isolated convective PFs display a more selective range of life duration than the stratiform, as seen by the stronger curvature of the blue curve compared to the red, in agreement with the previously reported data by (Berg & Haerter, 2013) but for local rain durations in Germany. We find typical MCS lifetimes to be around 10 hours when accounting for inac-

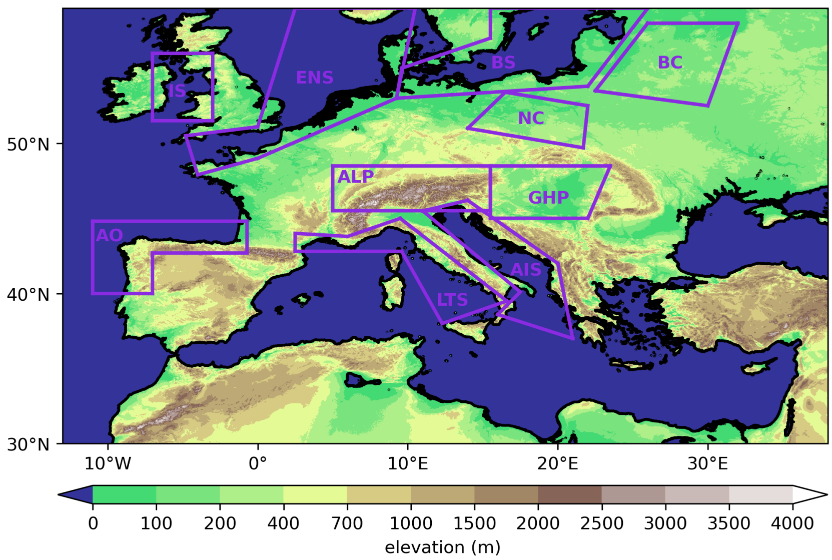

Figure 3. Study domain highlighting sub-regions: AO for Atlantic Ocean, IS for Irish Sea, ENS for English channel and North Sea, LTS for Ligurian and Tyrrhenian Seas, ALP for Alps, BS for Baltic Sea, AIS for Adriatic and Ionian Seas, NC for north Carpathian, GHP for Great Hungarian Plains and BC for Baltic Continent. The shadings represent the elevation (in m).

tive periods, whereas the duration of the active MCS periods are shorter by about a half of the total MCS life time. The area distribution (Fig. 2c) closely mirrors that of duration. In detail, mean MCS areas are even more selective, their occurrence frequency peaking for areas around $10^4\,\mathrm{km}^2$, which is partly influenced by our detection method enforcing a size threshold of 100 km of diameter. The PDF of mean precipitation (Fig. 2d) shows that high precipitation intensities, $> 10\,\mathrm{mm.h}^{-1}$, are approximately three times more frequent within MCS than for isolated convective PFs, and isolated convective cases are overall more intense than stratiform ones. The maximum around 2 $\mathrm{mm.h}^{-1}$ can be attributed to our detection threshold.

Given the intensity distributions (Fig. 2d), MCS can not only be seen as a collection of stratiform and convective precipitation patches but there is a systematic precipitation enhancement. This may result from the merging of convective cells, possibly related to dynamical (cold pools and/or mesoscale circulation; e.g. Haerter and Schlemmer (2018)) and/or microphysical effects (reduced entrainment and/or rain evaporation; e.g. Da Silva et al. (2021)).

3.2 MCS dominate in southern coastal regions in winter and continental regions in summer

As noted (Taszarek et al., 2019), mid-latitude convection is strongly dependent on season, a feature we examine further by examining the MCS occurrence for the different months (Fig. 4). As might be expected from the overall precipitation climatology in Europe (Fig. S4), MCS are generally more frequent in the coastal regions of southern Europe in winter, whereas they dominate in summer for the North. It is however worth pointing out that longitudinal differences exist: e.g., along the Eastern Adriatic the overall highest MCS frequency (approximately six per month) is reached in November, whereas the remaining Mediterranean or the continental regions at similar latitude, show a factor 2—3 less. Similar variations are seen in northwestern Spain or the Italian west coast during fall, where frequencies are again much higher than for similar latitudes. As opposed to the strong activity during fall, the transitional period during spring shows generally weak MCS activity. This lack of symmetry regarding MCS during the transitional periods, where continental temperatures are fairly similar, points to a strong influence of the large water bodies, with their large heat capacities, thus memory, on MCS. Summertime MCS, e.g., from June to August, are most frequent over the Alps, reaching about five per month in August. To a lesser extent this effect also holds for the Carpathians, highlighting the role of topography in triggering/enhancing deep convection (J. Houze & Robert, 2012). Perhaps more surprisingly, the continental regions near the East of southern Baltic Sea experience an important peak of MCS occurrence during the month of July, with around 3.5 MCS in this month on average. Another remarkable feature is the high number (exceeding 4 on average) of MCS in both southern Baltic Sea and southern North Sea (especially in the southeastern side) during August, while the surrounding continental areas experience comparably fewer MCS. The spatial peak of MCS occurrence over these regions extends to the fall months. Finally, one may notice that northern Germany experiences fewer MCS than its surrounding regions between June to September. This may be due to the Alps acting as a barrier to some of the MCS, which mostly travel in southwesterly flows (not shown).

Similarities between the spatial distribution of MCS occurrence in our current study and previous studies exist for the summer months. Yet, there are some noticeable differences compared to the previous climatologies of summer MCS (Morel & Senesi, 2002; Kolios & Feidas, 2010). While some of the difference might be explained by the longer averaging time used by the present study, an important difference lies in our method of identifying MCS by precipitation and lightning, whereas both Morel and Senesi (2002) and Kolios and Feidas (2010) used a method based on cloud top brightness temperature. In particular, we found a peak of MCS occurrence in both the North Sea and the Baltic Sea during August and a generally higher MCS occurrence in northern Europe during the warm season compared to Morel and Senesi (2002). Similarly, while the peak of MCS frequency in fall over the eastern Adriatic is expected (Feng et al., 2021; Taszarek et al., 2019), the peak over northwestern Spain is more surprising and was not found in previous studies based on cloud top brightness temperature for MCS identification (García-Herrera et al., 2005; Feng et al., 2021). We believe that the MCS over the North Sea and the Baltic Sea in late summer, and those over northwestern Spain during the cold season, are due to less deep convective systems that do not satisfy the IR criteria but have a large area and still produce some lightning.

Thus, MCS affect many regions over Europe throughout the year, and, due to their convective nature and their large spatial extent, MCS often generate large amounts of precipitation both in time and in space (e.g., Schumacher and Johnson (2005)). In the following, we quantify their contribution to total and extreme precipitation for each seasons (DJF, MAM, JJA, SON).

3.3 Substantial MCS contributions to rainfall totals

Again distinguishing seasons, MCS account for large precipitation amounts exceeding 100 mm in a single season over large areas (Fig. 5), which often corresponds to more than an half of the total rainfall in this season (Fig. 6). Overall, MCS precipitation dominate convective precipitation (Fig. S5) and its spatial patterns are generally commensurate with those of MCS frequency in the previous section (Fig. 4) and those of the mean precipitation climatology (Fig. S4). There are however smaller scale differences that can be attributed to the average spatial distribution of precipitation within individual MCS. In winter and to a lesser extent in fall, precipitation totals stemming from MCS tend to peak offshore along the coasts, a pattern that is even more pronounced for isolated convection (Fig. S6) and suggesting a role of the land-sea contrasts for MCS triggering in these seasons. The regions most affected by MCS precipitation are eastern Adriatic, west-

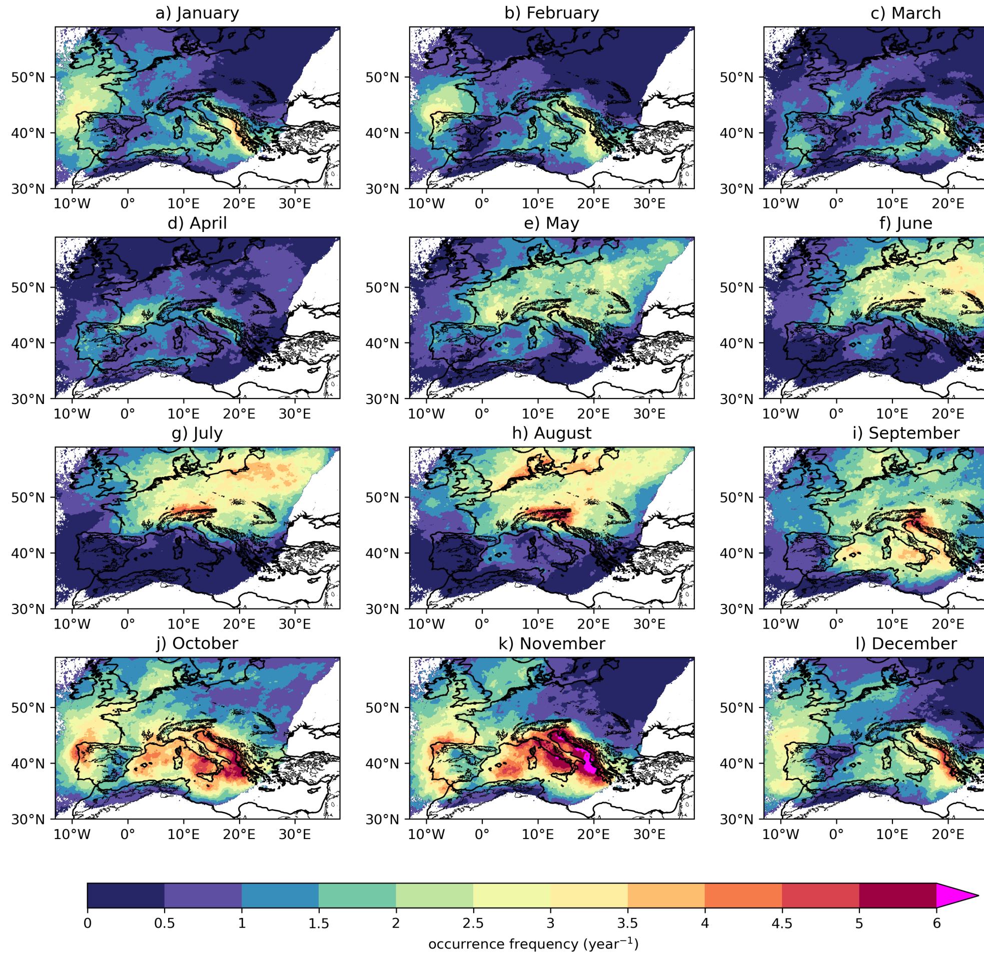

Figure 4. Averaged number of MCS per year by month (a-i). White areas represent missing values, defined as points with means of less than one lightning strike per year.

ern Italy, and south eastern France during fall, with MCS rainfall contributions exceeding 300 mm on average, which corresponds to 60% to 80% of the total precipitation. Northwestern Spain also exhibits a pronounced peak exceeding 200 mm in both fall and winter, although the contribution to total precipitation is somewhat lower with 40-50%. This region, and more generally most of northern Europe is also significantly impacted by stratiform precipitation stemming from Atlantic low pressure systems (Fig. S7), explaining relatively low MCS contributions to total precipitation, there. The MCS contribution to total precipitation is comparatively higher in southern Portugal in all seasons although the number of MCS affecting northwestern Spain is higher.

In spring, MCS precipitation amounts are more homogeneous between continents and seas, reaching about 30-50 mm over large areas, which corresponds to 30-40% of total precipitation. The summer MCS precipitation peaks at about 200 mm over the mountain ranges and the northern Seas of Europe, corresponding to about half of the seasonal total precipitation in these areas.

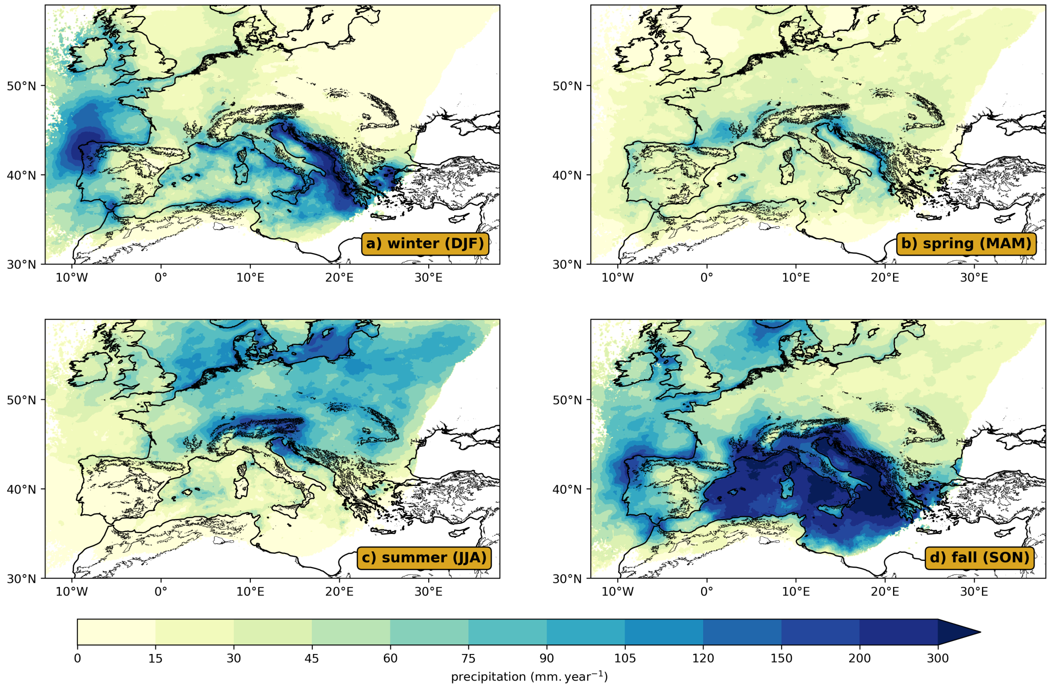

Figure 5. Total precipitation per year (in mm.year^{-1}) from MCS over Europe in winter (DJF, a), spring (MAM, b), summer (JJA, c) and fall (SON, d).

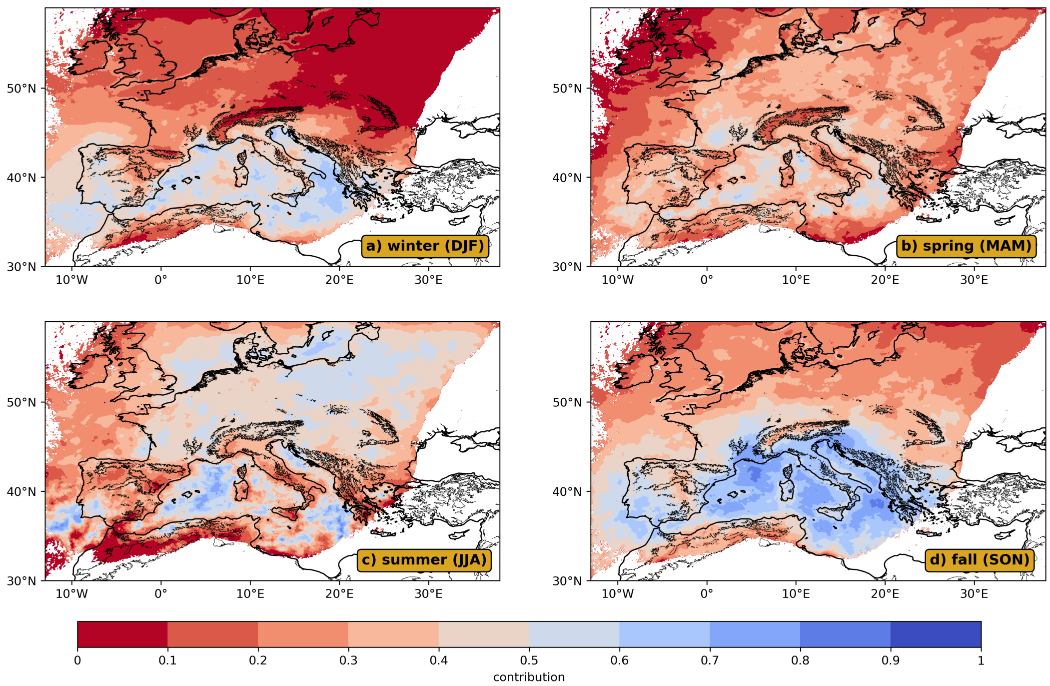

Figure 6. Contribution of MCS to total precipitation over Europe in winter (DJF, a), spring (MAM, b), summer (JJA, c) and fall (SON, d).

3.4 Extreme precipitation dominated by MCS

One of the most common hazards resulting from MCS is their tendency to generate intense precipitation accumulations over extended regions. To quantify the MCS contribution to extreme precipitation accumulations we first derive the 90th percentile of event-based precipitation accumulations from individual PFs (both MCS and non-MCS PFs) for each pixel (displayed in Fig. 7). We select areas where the amplitude of the confidence interval (at 95% of confidence level) on the 90th percentile of precipitation accumulations does not exceed 10 percents to ensure a reasonable definition of the 90th percentile. One can see that the PFs tend to produce heavy rain accumulations over the Mediterranean in all seasons but especially during fall and winter where the 90th percentile of precipitation accumulation due to individual PFs exceeds 40 mm along the coasts. Most of the coastal areas exhibit maxima in extreme precipitation accumulations, as noticed for both isolated convective and MCS precipitation totals (Fig. 5, S6). By compositing over events over several of the coasts in December (Fig. S8, S9), we found that their maxima are often associated with enhanced low-level winds from sea to land, suggesting enhanced convergence of moisture by the reduction of wind speed when propagating inland, e.g., due to increased surface roughness or/and the presence of topography. We find this to be a characteristic of coastal isolated convective events and most coastal MCS.

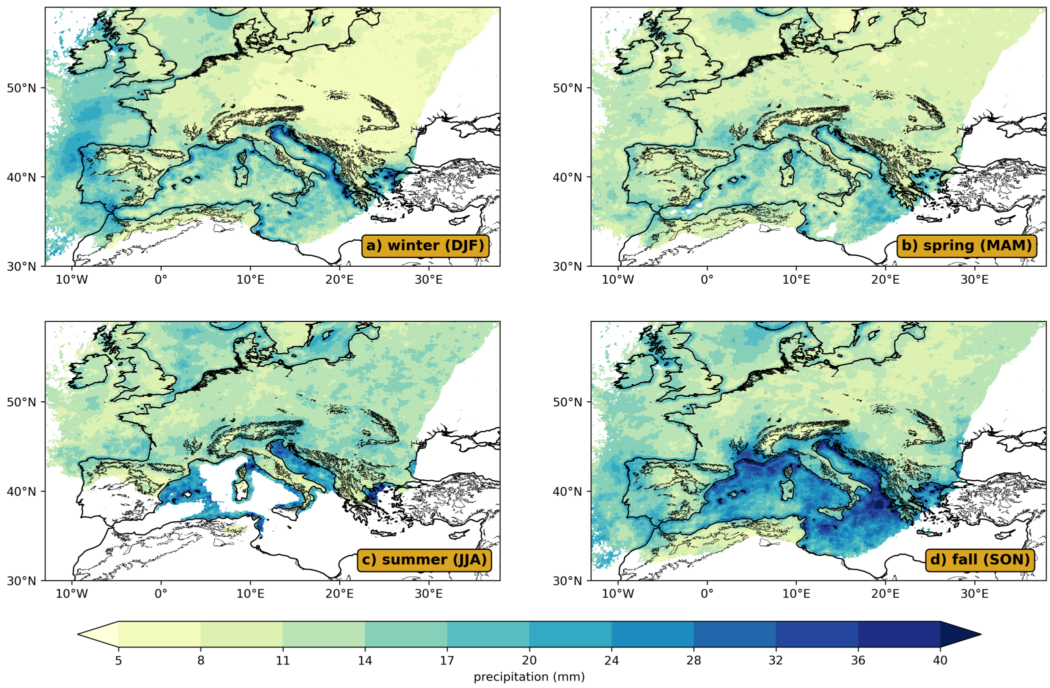

Figure 7. 90th percentile of individual PF precipitation accumulations (in mm) over Europe in winter (DJF, a), spring (MAM, b), summer (JJA, c) and fall (SON, d). White areas are missing data, i.e. points with an insufficient number of PFs (section 3.4) or with means of less than one lightning strike per year.

For each pixel we then select all PFs that produce rainfall exceeding the local 90th percentile of precipitation accumulation. By determining the fractional contribution by MCS (Figure 8) we show that MCS contribute more strongly to extreme precipitation events than to the mean. In some parts of the Mediterranean and the southern Iberian Peninsula, this contribution reaches a peak during fall approaching 100% and remains high (> 70%) during winter. In summer, more than 70% of rainfall accumulation extremes in continental Europe are due to MCS while the remaining 30% are mainly due to isolated convective events (Fig. S10). Although MCS are not particularly frequent in spring, their contribution to extreme precipitation accumulation is significant, exceeding 50% in most of Europe (except UK) and in the Mediterranean area. In this season, the remainder of extreme rainfall events is due isolated convective and stratiform rainfall (Fig. S11), with a similar share between these two (around 25%).

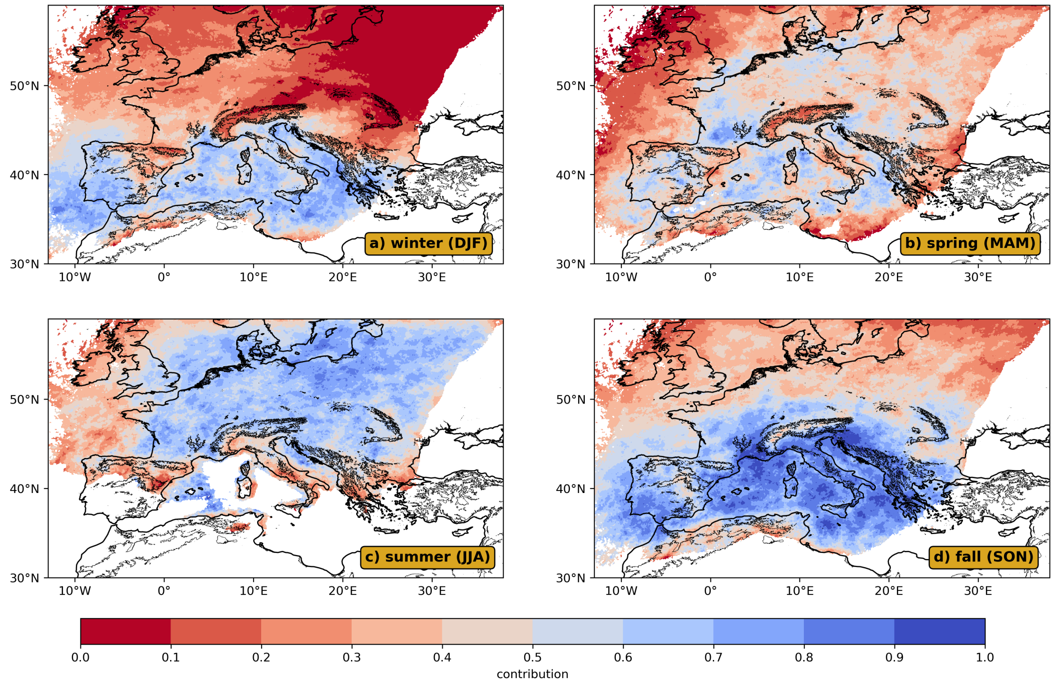

Figure 8. Contribution of MCS to the precipitation features producing the 10% most extreme precipitation accumulations (as defined in section 3.4) over Europe in winter (DJF, a), spring (MAM, b), summer (JJA, c) and fall (SON, d).

Summing up, MCS generally dominate precipitation accumulation extremes over most of Europe, with only northern Europe during winter constituting an exception.

3.5 Diurnal cycle — large contrasts between coasts and continents

Often poorly represented by numerical models (Brockhaus et al., 2008), the diurnal cycle of precipitation is of key mechanistic and practical relevance. For each of the sub-regions (Fig. 3) and each month, we compute the diurnal cycle of the expected value of MCS precipitation given the occurrence of a MCS in the sub-region at any time of the day. In detail, we collect the MCS precipitation intersecting the sub-region, average over the sub-region, and stratify by local solar time (LST) 1-h bins. For each MCS affecting the sub-region, to ensure an equal number of samples per LST bins and thus a fair estimation of the MCS precipitation conditional probability, we complete each bins by zeros. For each bin, we finally calculate the MCS averaged precipitation and select the months of peak MCS activity according to the monthly number distribution shown in Fig. 4.

3.5.1 Large inter-month and inter-regional variability in coastal regions.

For the coastal sub-regions (BS, ENS, AO, IS, LTS and AIS) the diurnal cycle of MCS precipitation varies strongly between sub-regions and seasons. Some sub-regions (BS in June, July, October; ENS in November; AO in February; IS in October, November, and December) exhibit afternoon peaks of MCS precipitation, which are likely associated with continental convection. We however note that the amplitude of these peaks is not commensurate with the amplitude of the solar diurnal cycle, e.g., IS experiences the strongest afternoon peak of MCS precipitation during the month with the least diurnal variation in solar irradiance of the year (December). A number of sub-regions (BS in October; ENS from September to December; AO in December and January; IS in October and November; LTS in September, October and December; AIS in February) exhibit a nocturnal/early morning peak, reminiscent of the total precipitation diurnal cycle over most sea areas (Dai, 2001; Bowman et al., 2005; Tan et al., 2019; Watters & Battaglia, 2019). We note that this peak is not systematic and depends on the region, the month and type of precipitation (Figs S12, S13, S14).

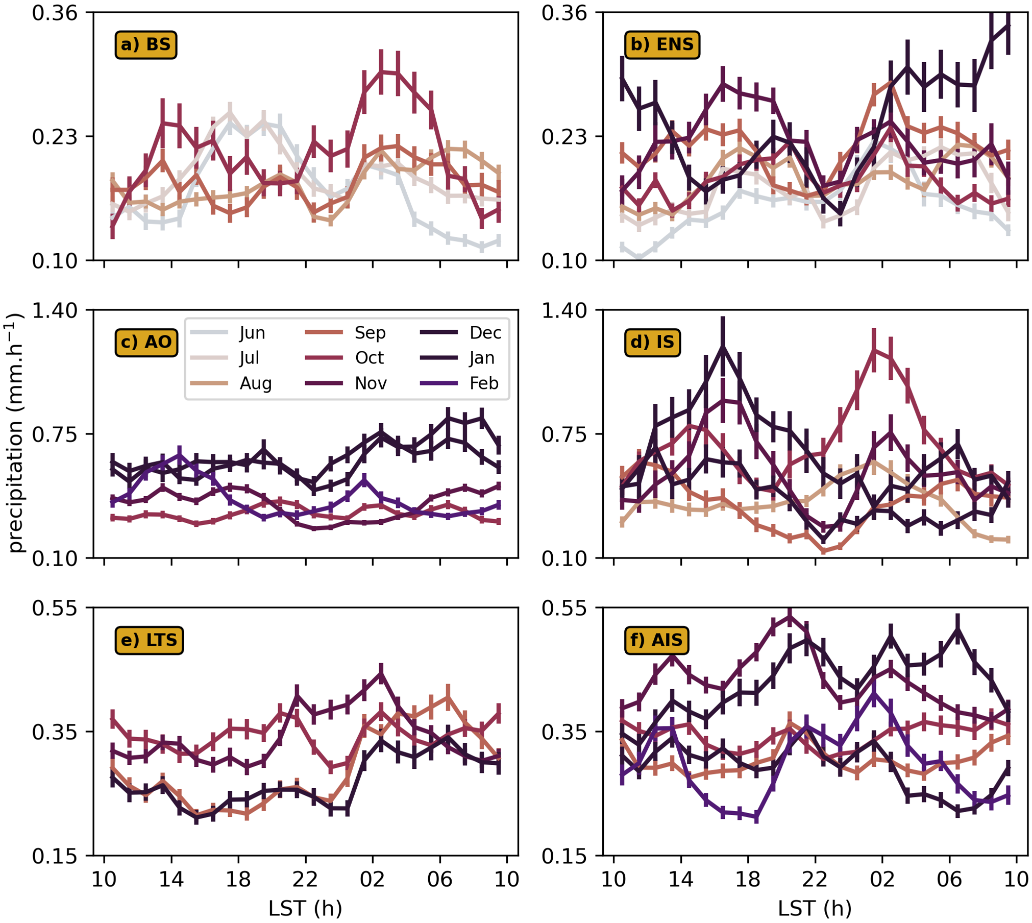

Figure 9. Monthly expected values of MCS precipitation (in mm.h^{-1}) conditioned on MCS occurrence within the coastal sub-regions as a function of LST (in h): BS (a), ENS (b), AO (c), IS (d), LTS (e) and AIS (f) (see Fig. 3). Results are given for months with the main MCS activity according to Fig. 4. For each LST bin the standard error is calculated to estimate the uncertainty in the mean and represented by error bars.

3.5.2 Nocturnal peaks in continental regions

The diurnal cycle analysis was repeated for the continental sub-regions for May to October (Fig. 10). There, a generally more pronounced MCS diurnal cycle is found, exhibiting reduced inter-month variability compared to the coastal areas. In the four continental sub-regions there is a strong late-afternoon peak of MCS precipitation from May to August. This peak is most pronounced during July over ALP and BC, whereas it is more marked in May in GHP and NC. We note that this peak tends to occur later (around 20 LST) in the lee of the Alps (in GHP) and the lee of the Carpathians (in NC), compared to the Alps and the Baltic plains (BC; around 18 LST). This characteristic may be explained by propagating systems from the mountains to the plains occurring later in the evening. Similarly, convective precipitation tends to peak earlier in the afternoon than MCS (Fig. S17), consistent with the time required for the upscale growth of MCS. Generally weaker diurnal ranges of MCS precipitation are observed during September and October (as observed for total precipitation in Mandapaka et al. (2013); Alber et al. (2015)).

Interestingly, for the GHP sub-region, the diurnal cycle of MCS precipitation exhibits another systematic peak (at around 3 LST). This nocturnal peak becomes more and more pronounced when moving from May to October, as opposed to the late afternoon peak, which diminishes in the course of this seasonal period. A secondary nocturnal peak also appears for the other continental sub-regions, even though it is less pronounced and systematic. One could argue that the nocturnal MCS precipitation peak in GHP might be related to the Adriatic Sea diurnal cycle, "leaking" into GHP at nighttime as a result of a southwesterly flow. However, as seen in Fig. 9g and Fig. S12g, there is no evidence for a clear evening or nocturnal peak in both MCS and isolated convective precipitation for AIS during these months, suggesting a local enhancement/development of MCS precipitation during the night in GHP. We further note that the nocturnal peak is generally less pronounced or does not appear in isolated convective precipitation, as well as for lightning (Fig. S15, S16 and S17). Levizzani et al. (2010) evidenced a slight nocturnal peak of cold cloud frequency in August over similar longitudes, mentioning a potential role of the Carpathians in enhancing precipitating systems. Twardosz (2007) analyzed the diurnal cycle of precipitation over southern Poland conditional on different circulation types and noted a nocturnal/early morning peak of precipitation associated with warm fronts in southerly/southwesterly flows. It is however uncertain whether nocturnal MCS in this region are regularly embedded within a warm front, when warm fronts are usually associated to less convectively unstable environments (as noted in Twardosz (2010)). The precise origin of MCS nocturnal precipitation peaks over continental areas remains thus uncertain and requires further studies.

4 Understanding the spatio-temporal distribution of European MCS

It was found that MCS often develop near frontal boundaries which provide dynamical lifting over large scales (e.g. Maddox (1983)). Here, we estimate the frontal activity by using the method of Parfitt et al. (2017) to identify fronts in the middle troposphere (600 hPa; to avoid the detection of low level breeze fronts), and define fronts as contiguous frontal pixels with a horizontal extent of at least 300 km. To only select synoptic fronts from low pressure systems, we discard every fronts containing less than 4 ERA5 pixels with a low pressure and a low geopotential height at 500 hPa (defined as a negative anomaly from a 2000-2020 climatology). By calculating the frequency of frontal pixels as a function of the distance from a PF at the time of their largest extent (Fig. S18), we find that MCS are more tightly connected to the presence of a frontal boundary at few hundreds of km from their center than for isolated convective and stratiform PFs. Among these fronts, the contribution of cold fronts is the most important by a factor of two compared to warm fronts (not shown).

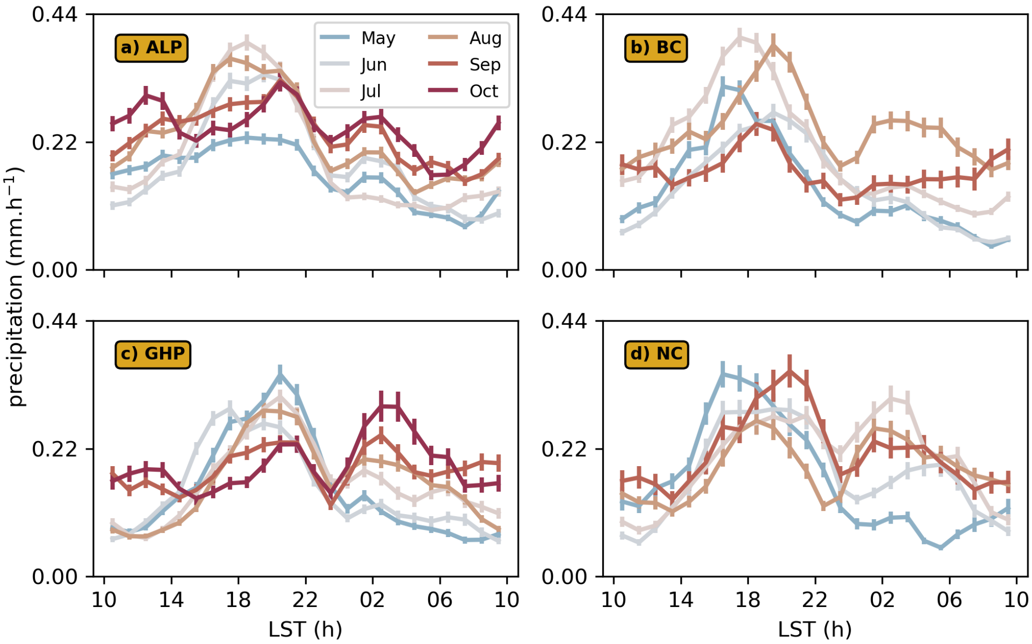

Figure 10. Similar as Fig. 9 but for the continental sub-regions: ALP (a), BC (b), GHP (c) and NC (d) (see Fig. 3).

In the remainder of this section, we analyze the MCS precipitation annual cycle for the different sub-regions (Fig. 3) in relation to the SST (or land 2-m temperatures for continental sub-regions), the frequency of significant CAPE, and frontal occurrence. CAPE is considered as significant when it exceeds a threshold of 100 J.kg^{-1} (consistently with fig. S2). We evaluate frontal occurrence as follows: for each pixel within each sub-region we count the number of times a front occurred over each month. If a pixel is part of two fronts that are separated within less than a three-hour interval, it is assumed that it is the same front. This front occurrence frequency is then averaged over the box and the 16 years.

4.1 Coastal drivers: dynamics.

In all coastal locations, SSTs generally peak in August, as does CAPE. For the northern coasts of Europe, BS and ENS, these peaks coincide with that of MCS precipitation, suggesting that convective instability might play a determining role in MCS precipitation there. This applies particularly to BS, where the rapid SST decrease after August is accompanied by a rapid decay of CAPE. For ENS the drop in SSTs is more gradual, limiting the decay of CAPE in fall. This, associated with increased frontal activity, may extend the MCS precipitation peak until November in ENS. For all remaining coastal regions the MCS precipitation peak is delayed relative to the August SST and CAPE peaks: November for the Mediterranean coasts (LTS and AIS), October for IS and December for AO. Unlike BS and ENS, these regions experience higher SSTs in August that decrease progressively during fall, hence these regions might be less limited by CAPE availability in fall. Rather, despite the larger summertime CAPE, the lack of triggering and organizing large scale patterns, such as fronts, may be limiting factors in these regions during summer. Across sub-regions, we attribute the decrease in MCS activity in winter or early spring to CAPE limitations.

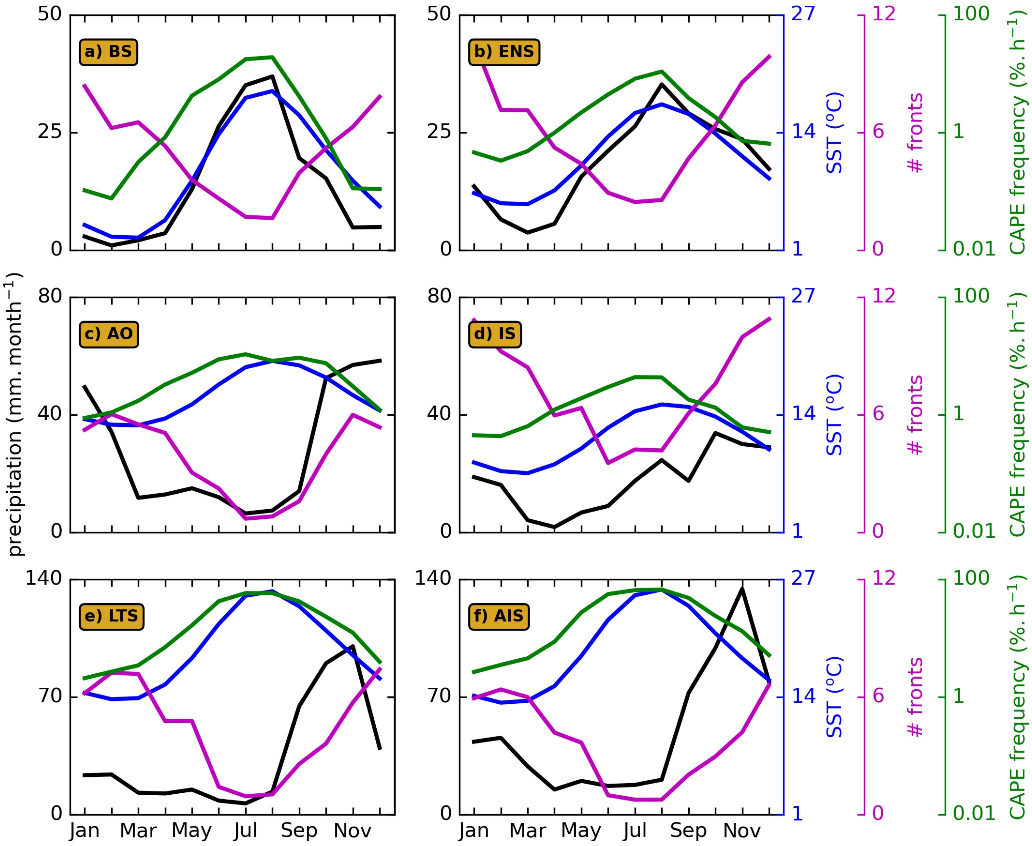

Figure 11. Averaged monthly time series of IMERG MCS precipitation amounts (in mm.month^{-1}, black), ERA-5 Sea Surface Temperature (SST, in degrees, blue), number of fronts (magenta), and Convective Available Potential Energy (CAPE) frequency (defined in section 4; in %.h^{-1}, green; note the logarithmic scale) for the coastal sub-regions: BS (a), ENS (b), AO (c), IS (d), LTS (e) and AIS (f) (see Fig. 3).

4.2 Continental drivers: thermodynamics.

In contrast to the coastal regions, for land regions MCS precipitation peaks generally coincide with the peaks in surface temperature, i.e., July for BC and NC and August for ALP and GHP, despite a relatively low front frequency, suggesting a more thermodynamic control. We interpret this as resulting from land surfaces often constituting topographic boundaries that force large-scale convection without the need for an air mass boundary. We note that CAPE frequency maxima generally occurs slightly earlier in the year (typically in July). ALP and GHP show a long tail in the fall months despite thermodynamic and instability conditions deteriorating. These might be related to Mediterranean unstable air masses that are advected towards the Alps and Balkans, and eventually leading to MCS formation by topographic lifting or MCS advection.

5 Conclusions

We have characterized mesoscale convective systems (MCS) over Europe by building a long-term MCS climatology (16 years) at high spatial resolution (0.1°). MCS are identified by detecting and tracking precipitation features using the recent IMERG satellite-

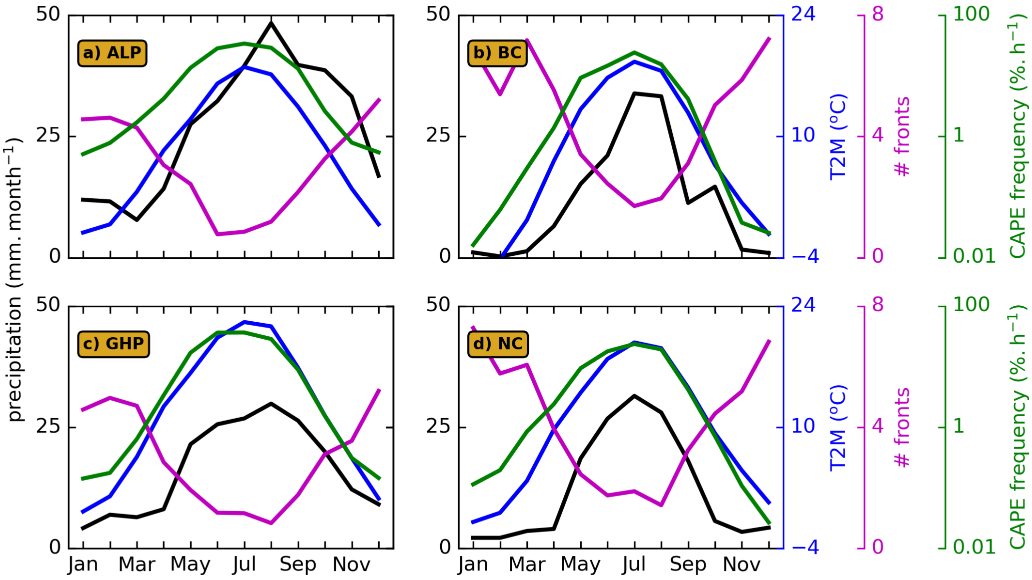

Figure 12. Similar as Fig. 11 but for the continental sub-regions: ALP (a), BC (b), GHP (c) and NC (d) (see Fig. 3).

based dataset and conditioning on lightning data from the EUCLID dataset. MCS are abundant and responsible for substantial precipitation totals in all seasons. In fall and winter, MCS are mainly concentrated over the Mediterranean and the Atlantic coasts, whereas in summer, MCS mainly affect continental Europe, especially mountainous regions, and the northern seas. Spring is transitionary, with MCS activity moving inland and pole-ward.

The contribution of MCS to total rainfall peaks over the Mediterranean during fall, exceeding 70% over large areas. While many other regions are also significantly affected by stratiform precipitation from extratropical cyclones, the MCS contribution often reaches similar amplitudes over the hotspot regions. Concerning extremes, MCS contribute even more strongly, exceeding 90% in the Mediterranean in fall and 70% over northern Europe in summer.

The diurnal cycle of MCS precipitation over coastal areas exhibits large inter-month and inter-regional variability, far from a systematic nocturnal/early morning maximum expected from the climatology (Watters & Battaglia, 2019), and suggesting that local mechanisms are involved. The MCS precipitation diurnal cycle over the selected continental sub-regions shows a more pronounced and systematic diurnal cycle during the warmest months of the year. For these months we find a late afternoon/evening peak for MCS, following the afternoon peak of isolated convective. In some of the locations (particularly in the Great Hungarian Plains in early fall), we find an additional nocturnal maximum, despite reduced convective instability. The exact origin of this striking feature remains unclear and begs for further investigation, such as through high-resolution simulation case studies.

We then analyze the MCS annual cycle and associated variables, finding that, across sub-regions, convective instability peaks in summer whereas frontal activity, for which we found an overall strong involvement in MCS activity, peaks in the winter. Two main features stick out:

- In sub-regions where convective instability is a limiting factor and decreases rapidly from summer to fall, MCS precipitation peaks concomitantly with the peak of convective instability and surface temperature. This is the case for the continental regions and the Baltic and North Seas.
- In sub-regions where the convective instability has a more gradual decrease or remains significant in fall, MCS precipitation tends to peak in fall. We further attribute this delay to more favorable dynamical conditions, namely more pronounced frontal activity and larger boundary layer lapse rates. This is the case of the large water bodies of high-heat capacity, for which the decrease of SSTs during fall is slower. Whereas MCS do occasionally occur in these regions, the lack of dynamical forcing appears as a limiting factor during summer compared to fall.

In summary, this study highlights the significant role of MCS in driving total, and in particular extreme, rainfall in Europe. We advocate studies unveiling the mechanisms leading to extreme MCS rainfall and their local characteristics, such as the nocturnal MCS rainfall enhancement over eastern Europe, diurnal cycle variability in coastal regions, and the role of the topography, microphysics, and radiation. Such studies could combine higher resolution precipitation datasets, e.g., radar, with numerical simulations to explore local effects. Such endeavors may ultimately lead to a better causal understanding and thus improved forecasting of mid-latitude MCS rainfall extremes.

6 Open Research

ERA5 reanalysis data were downloaded from `https://doi.org/10.24381/cds.bd0915c6` and `https://doi.org/10.24381/cds.adbb2d47`. The IMERG precipitation product was downloaded from `https://doi.org/10.5067/GPM/IMERG/3B-HH/06` (Huffman et al., 2019). The surface synoptic observation (SYNOP; O'Brien (2008)) was downloaded from `https://catalogue.ceda.ac.uk/uuid/9f80d42106ba708f92ada730ba321831`. The EUCLID data are available upon request from `https://www.euclid.org/#`. Topography data were supplied by the GEBCO Compilation Group (2022) GEBCO_2022 Grid (doi:10.5285/e0f0bb80-ab44-2739-e053-6c86abc0289c).

Acknowledgments

The authors gratefully acknowledge funding by the European Research Council (ERC) under the European Union's Horizon 2020 research and innovation program (grant number: 771859). JOH further acknowledges funding by a grant from the VILLUM Foundation (grant number: 13168) and the Novo Nordisk Foundation Interdisciplinary Synergy Program (grant no. NNF19OC0057374).

References

Adler, R. F., Sapiano, M. R., Huffman, G. J., Wang, J.-J., Gu, G., Bolvin, D., ... others (2018). The global precipitation climatology project (gpcp) monthly analysis (new version 2.3) and a review of 2017 global precipitation. *Atmosphere*, *9*(4), 138. doi: 10.3390/atmos9040138

Alber, R., Jaagus, J., & Oja, P. (2015). Diurnal cycle of precipitation in estonia. *Estonian Journal of Earth Sciences*, *64*(4), 305. doi: 10.3176/earth.2015.36

Berg, P., & Haerter, J. (2013). Unexpected increase in precipitation intensity with temperature—a result of mixing of precipitation types? *Atmospheric Research*, *119*, 56–61.

Bowman, K. P., Collier, J. C., North, G. R., Wu, Q., Ha, E., & Hardin, J. (2005). Diurnal cycle of tropical precipitation in tropical rainfall measuring mission (trmm) satellite and ocean buoy rain gauge data. *Journal of Geophysical Research: Atmospheres*, *110*(D21). doi: 10.1029/2005JD005763

Brockhaus, P., Luthi, D., & Schar, C. (2008). Aspects of the diurnal cycle in a regional climate model. *Meteorologische Zeitschrift*, *17*(4), 433–444. doi: 10.1127/0941-2948/2008/0316

Cheeks, S. M., Fueglistaler, S., & Garner, S. T. (2020). A satellite-based climatology of central and southeastern u.s. mesoscale convective systems. *Monthly Weather Review*, *148*(6), 2607 - 2621. doi: 10.1175/MWR-D-20-0027.1

Cui, W., Dong, X., Xi, B., Feng, Z., & Fan, J. (2020). Can the gpm imerg final product accurately represent mcss' precipitation characteristics over the central and eastern united states? *Journal of Hydrometeorology*, *21*(1), 39 - 57. doi: 10.1175/JHM-D-19-0123.1

Dai, A. (2001). Global precipitation and thunderstorm frequencies. part ii: Diurnal variations. *Journal of Climate*, *14*(6), 1112 - 1128. doi: 10.1175/1520-0442(2001)014⟨1112:GPATFP⟩2.0.CO;2

Da Silva, N. A., Muller, C., Shamekh, S., & Fildier, B. (2021). Significant amplification of instantaneous extreme precipitation with convective self-aggregation. *Journal of Advances in Modeling Earth Systems*, *13*(11), e2021MS002607. (e2021MS002607 2021MS002607) doi: https://doi.org/10.1029/2021MS002607

Feng, Z., Leung, L. R., Liu, N., Wang, J., Houze Jr, R. A., Li, J., ... Guo, J. (2021). A global high-resolution mesoscale convective system database using satellite-derived cloud tops, surface precipitation, and tracking. *J. Geophys. Res.*, *126*(8), e2020JD034202. doi: 10.1029/2020JD034202

Fowler, H. J., Lenderink, G., Prein, A. F., Westra, S., Allan, R. P., Ban, N., ... others (2021). Anthropogenic intensification of short-duration rainfall extremes. *Nature Reviews Earth & Environment*, *2*(2), 107–122.

García-Herrera, R., Hernández, E., Paredes, D., Barriopedro, D., Correoso, J. F., & Prieto, L. (2005). A mascotte-based characterization of mcss over spain, 2000–2002. *Atmospheric Research*, *73*(3-4), 261–282.

Geerts, B., Parsons, D., Ziegler, C. L., Weckwerth, T. M., Biggerstaff, M. I., Clark, R. D., ... Wurman, J. (2017). The 2015 plains elevated convection at night field project. *Bulletin of the American Meteorological Society*, *98*(4), 767 - 786. doi: 10.1175/BAMS-D-15-00257.1

Haberlie, A. M., & Ashley, W. S. (2019). A radar-based climatology of mesoscale convective systems in the united states. *Journal of Climate*, *32*(5), 1591 - 1606. doi: 10.1175/JCLI-D-18-0559.1

Haerter, J. O., & Schlemmer, L. (2018). Intensified cold pool dynamics under stronger surface heating. *Geophysical Research Letters*, *45*(12), 6299-6310. doi: 10.1029/2017GL076874

Hersbach, H., Bell, B., Berrisford, P., Hirahara, S., Horányi, A., Muñoz-Sabater, J., ... Thépaut, J.-N. (2020). The era5 global reanalysis. *Quarterly Journal of the Royal Meteorological Society*, *146*(730), 1999-2049. doi: 10.1002/qj.3803

Houze, J., & Robert, A. (2012). Orographic effects on precipitating clouds. *Reviews of Geophysics*, *50*(1). doi: 10.1029/2011RG000365

Houze, R. A. (2018). 100 years of research on mesoscale convective systems. *Meteor. Monogr.*, *59*, 17.1 - 17.54. doi: 10.1175/AMSMONOGRAPHS-D-18-0001.1

Huffman, G. J., Stocker, E. F., Bolvin, D. T., Nelkin, E. J., & Tan, J. (2019). Gpm imerg final precipitation l3 half hourly 0.1 degree x 0.1 degree v06. *Goddard Earth Sciences Data and Information Services Center (GES DISC), Accessed: 1st August 2021.*. doi: 10.5067/GPM/IMERG/3B-HH/06

Jirak, I. L., & Cotton, W. R. (2007). Observational analysis of the predictability of mesoscale convective systems. *Weather and Forecasting*, *22*(4), 813 - 838. doi: 10.1175/WAF1012.1

Jirak, I. L., Cotton, W. R., & McAnelly, R. L. (2003). Satellite and radar survey of mesoscale convective system development. *Mon. Wea. Rev.*, *131*(10), 2428 - 2449. doi: 10.1175/1520-0493(2003)131⟨2428:SARSOM⟩2.0.CO;2

Kolios, S., & Feidas, H. (2010). A warm season climatology of mesoscale convective systems in the mediterranean basin using satellite data. *Theoretical and applied climatology*, *102*(1), 29–42.

Laing, A. G., & Fritsch, M. (1997). The global population of mesoscale convective complexes. *Quart. J. Roy. Meteor. Soc.*, *123*(538), 389-405. doi: 10.1002/qj.49712353807

Levizzani, V., Pinelli, F., Pasqui, M., Melani, S., Laing, A. G., & Carbone, R. E. (2010). A 10-year climatology of warm-season cloud patterns over europe and the mediterranean from meteosat ir observations. *Atmospheric Research*, *97*(4), 555-576. (From the Lab to Models and Global Observations: Hans R. Pruppacher and Cloud Physics) doi: 10.1016/j.atmosres.2010.05.014

Li, P., Moseley, C., Prein, A. F., Chen, H., Li, J., Furtado, K., & Zhou, T. (2020). Mesoscale convective system precipitation characteristics over east asia. part i: Regional differences and seasonal variations. *Journal of Climate*, *33*(21), 9271–9286.

Liu, C., & Zipser, E. J. (2015). The global distribution of largest, deepest, and most intense precipitation systems. *Geophysical Research Letters*, *42*(9), 3591-3595. doi: 10.1002/2015GL063776

Luo, L., Xue, M., & Zhu, K. (2020). The initiation and organization of a severe hail-producing mesoscale convective system in east china: A numerical study. *J. Geophys. Res.*, *125*(17), e2020JD032606. (e2020JD032606 2020JD032606) doi: 10.1029/2020JD032606

Maddox, R. A. (1983). Large-scale meteorological conditions associated with midlatitude, mesoscale convective complexes. *Monthly Weather Review*, *111*(7), 1475 - 1493. doi: 10.1175/1520-0493(1983)111⟨1475:LSMCAW⟩2.0.CO;2

Mandapaka, P. V., Germann, U., & Panziera, L. (2013). Diurnal cycle of precipitation over complex alpine orography: inferences from high-resolution radar observations. *Quarterly Journal of the Royal Meteorological Society*, *139*(673), 1025-1046. doi: 10.1002/qj.2013

Mathias, L., Ermert, V., Kelemen, F. D., Ludwig, P., & Pinto, J. G. (2017). Synoptic analysis and hindcast of an intense bow echo in western europe: The 9 june 2014 storm. *Weather and Forecasting*, *32*(3), 1121 - 1141. doi: 10.1175/WAF-D-16-0192.1

Morel, C., & Senesi, S. (2002). A climatology of mesoscale convective systems over europe using satellite infrared imagery. ii: Characteristics of european mesoscale convective systems. *Quart. J. Roy. Meteor. Soc.*, *128*(584), 1973-1995. doi: 10.1256/003590002320603494

Moseley, C., Berg, P., & Haerter, J. O. (2013). Probing the precipitation life cycle by iterative rain cell tracking. *Journal of Geophysical Research: Atmospheres*, *118*(24), 13,361-13,370. doi: 10.1002/2013JD020868

Moseley, C., Henneberg, O., & Haerter, J. O. (2019). A statistical model for isolated convective precipitation events. *Journal of Advances in Modeling Earth Systems*, *11*(1), 360-375. doi: 10.1029/2018MS001383

Nesbitt, S. W., Cifelli, R., & Rutledge, S. A. (2006). Storm morphology and rainfall characteristics of trmm precipitation features. *Mon. Wea. Rev.*, *134*(10), 2702 - 2721. doi: 10.1175/MWR3200.1

O'Brien, C. (2008). *Met office (2008): Land synop reports from land stations collected by the met office metdb system.* `https://catalogue.ceda.ac.uk/uuid/9f80d42106ba708f92ada730ba321831`. (Online; accessed 21 October 2021)

Parfitt, R., Czaja, A., & Seo, H. (2017). A simple diagnostic for the detection of atmospheric fronts. *Geophysical Research Letters*, *44*(9), 4351-4358. doi: https://doi.org/10.1002/2017GL073662

Parker, M. D. (2008). Response of simulated squall lines to low-level cooling. *Journal of the Atmospheric Sciences*, *65*(4), 1323 - 1341. doi: 10.1175/2007JAS2507.1

Pitchford, K. L., & London, J. (1962). The low-level jet as related to nocturnal thunderstorms over midwest united states. *Journal of Applied Meteorology and Climatology*, *1*(1), 43 - 47. doi: 10.1175/1520-0450(1962)001⟨0043:TLLJAR⟩2.0.CO;2

Poelman, D. R., Schulz, W., Diendorfer, G., & Bernardi, M. (2016). The european lightning location system euclid – part 2: Observations. *Natural Hazards and Earth System Sciences*, *16*(2), 607–616. doi: 10.5194/nhess-16-607-2016

Punkka, A.-J., & Bister, M. (2015). Mesoscale convective systems and their synoptic-scale environment in finland. *Weather and Forecasting*, *30*(1), 182 - 196. doi: 10.1175/WAF-D-13-00146.1

Rigo, T., Berenguer, M., & del Carmen Llasat, M. (2019). An improved analysis of mesoscale convective systems in the western mediterranean using weather radar. *Atmospheric research*, *227*, 147–156.

Salio, P., Nicolini, M., & Zipser, E. J. (2007). Mesoscale convective systems over southeastern south america and their relationship with the south american low-level jet. *Monthly Weather Review*, *135*(4), 1290 - 1309. doi: 10.1175/MWR3305.1

Schulz, W., Diendorfer, G., Pedeboy, S., & Poelman, D. R. (2016). The european lightning location system euclid – part 1: Performance analysis and validation. *Natural Hazards and Earth System Sciences*, *16*(2), 595–605. doi: 10.5194/nhess-16-595-2016

Schumacher, R., & Johnson, R. H. (2005). Organization and environmental properties of extreme-rain-producing mesoscale convective systems. *Mon. Wea. Rev.*, *133*(4), 961 - 976. doi: 10.1175/MWR2899.1

Schumacher, R., & Rasmussen, K. (2020). The formation, character and changing nature of mesoscale convective systems. *Nat. Rev. Earth Environ.*, *1*, 300–314. doi: 10.1038/s43017-020-0057-7

Surowiecki, A., & Taszarek, M. (2020). A 10-year radar-based climatology of mesoscale convective system archetypes and derechos in poland. *Monthly Weather Review*, *148*(8), 3471 - 3488. doi: 10.1175/MWR-D-19-0412.1

Tan, J., Huffman, G. J., Bolvin, D. T., & Nelkin, E. J. (2019). Diurnal cycle of imerg v06 precipitation. *Geophysical Research Letters*, *46*(22), 13584-13592. doi: 10.1029/2019GL085395

Tan, J., Jakob, C., Rossow, W. B., & Tselioudis, G. (2015). Increases in tropical rainfall driven by changes in frequency of organized deep convection. *Nature*, *519*(7544), 451–454. doi: https://doi.org/10.1038/nature14339

Taszarek, M., Allen, J., Púčik, T., Groenemeijer, P., Czernecki, B., Kolendowicz, L., ... Schulz, W. (2019). A climatology of thunderstorms across europe from a synthesis of multiple data sources. *Journal of Climate*, *32*(6), 1813 - 1837. doi: 10.1175/JCLI-D-18-0372.1

Twardosz, R. (2007). Diurnal variation of precipitation frequency in the warm half of the year according to circulation types in kraków, south poland. *Theoretical and Applied Climatology*, *89*, 229–238. doi: 10.1007/s00704-006-0268-y

Twardosz, R. (2010). A synoptic analysis of the diurnal cycle of thunderstorm precipitation in kraków (southern poland). *International Journal of Climatology*, *30*(7), 1008-1013. doi: 10.1002/joc.1960

Watters, D., & Battaglia, A. (2019). The summertime diurnal cycle of precipitation derived from imerg. *Remote Sensing*, *11*(15). doi: 10.3390/rs11151781

Supporting Information for "The characteristics of mesoscale convective system rainfall over Europe"

Nicolas A. Da Silva [1], Jan O. Haerter[1,2,3]

[1]Complexity and Climate, Leibniz Centre for Tropical Marine Research, Fahrenheitstrasse 6, 28359 Bremen, Germany

[2]Physics and Earth Sciences, Constructor University Bremen, Campus Ring 1, 28759 Bremen, Germany.

[3]Niels Bohr Institute, University of Copenhagen, Blegdamsvej 17, 2100 Copenhagen, Denmark.

Contents of this file

1. Text S1 to S2
2. Figures S1 to S16

Introduction This document presents supporting figures for "The characteristics of mesoscale convective system rainfall over Europe". It provides the probability density function (PDF) of the goodness of ellipse fit (G) for mesoscale convective systems (MCS; Fig. S1) and the precipitation seasonal climatology (Fig. S4) from the Integrated Multi-satellitE Retrievals for GPM (IMERG) product. It describes an alternative MCS detection method using the Convective Available Potential Energy (CAPE) instead of lightning occurrence (Text S1; Fig. S3). It contains the analogous figures to the main manuscript but for other types of precipitation features (PF; isolated convection and stratiform) for total precipitation (Fig. S6, S7), the contribution to extreme precipitation (Fig. S10, S11, S5), the precipitation/lightning diurnal cycle (Figs S13, S16, S12, S15, S14, S17).

Text S2 and Figs S8, S9 support the coastal maximum of precipitation found in the main manuscript (Figs S8, S9). Finally, this document provides with the frontal pixel frequency as a function the distance for different PF types (Fig. S18).

Text S1: sensitivity to convection classification. Lightning occurrence within a precipitating system provides a clear indication for convection. However, lightning data are subject to measurement error and not continuously available in all regions. Thus, and to assess the robustness of our results, we tested an alternative criterion, namely CAPE determined from ERA5. We first determined an optimal threshold for ERA5 CAPE above which a PF is considered convective by additionally using the surface synoptic observations (SYNOP; O'Brien (2008)) dataset: whenever a cumulonimbus, thunderstorm, or lightning strike was observed at a given SYNOP station and at least 50 other SYNOP stations located within a radius of 500 km around this station (as evidence of convective activity), we extract the nearest ERA5 grid point and construct a PDF of ERA5 CAPE. The ERA5 CAPE field was previously filtered over a 5 x 5 spatial window in which the maximum CAPE was retained. By comparing the exceedance probability of CAPE in the occurrence of convection with the exceedance probability of CAPE for all the concatenated time series of all stations, we determine an optimal threshold of $100, \mathrm{J.kg}^{-1}$ above which the difference between both the former and later exceedance probabilties do not increase anymore (Fig.S2). With this alternative identification method, at any time of its life cycle, if a PF contains (or is surrounded in a 5-km radius) an ERA5 CAPE pixel value exceeding 100 J.kg^{-1}, then this PF is defined as convective. We then use the same diameter and duration thresholds (see section 2 of the main manuscript) to define MCS PFs. With this alternative method we find a similar spatio-temporal distribution of MCS precipitation over Europe (Fig. S3), exhibiting peaks in the same areas as those noted in section 3, which shows that the locations of high MCS activity are robust.

Text S2: coastal effect.

Figs. S9 and S8 were drawn to provide insights on the local maximum of precipitation found in coastal areas and described in the main manuscript. They show the monthly anomalies of surface water vapor mixing ratio and wind conditioned on MCS or isolated convection occurrence (respectively) near the coasts in December in four coasts around Europe. The occurrence of a MCS (respectively isolated convection) coastal event was defined by considering the spatial sum of MCS (resp. isolated convection) hourly precipitation heights within a box along the coast (drawn in magenta) and selecting hourly events for which this total precipitation height exceeds a threshold of 10 mm. Fig S8 shows pronounced wind and moisture anomalies converging to the coasts, and associated precipitation along the coasts. Fig S9 generally shows similar patterns but with a more diverted flow by the coast. While the coasts of Netherlands and Germany are still an area of low level wind convergence for MCS events (Fig S9b), there is an overall inland wind anomaly, which constitutes an exception compared to the other locations.

References

O'Brien, C. (2008). *Met office (2008): Land synop reports from land stations collected by the met office metdb system.* `https://catalogue.ceda.ac.uk/uuid/9f80d42106ba708f92ada730ba321831`. (Online; accessed 21 October 2021)

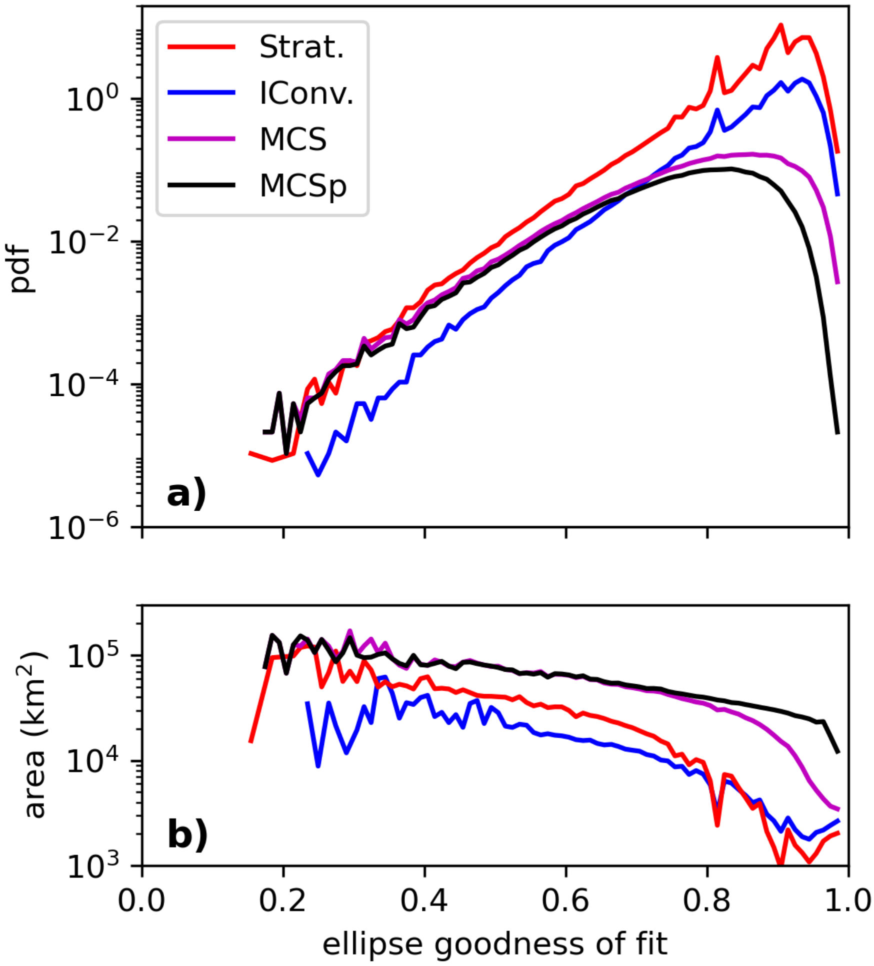

Figure S1. Probability Density Functions (PDF) of the ellipse Goodness of fit (G) as defined in eq. 1 in the main manuscript (a) and PF Area as a function of G for stratiform ("Strat.", red), isolated convective ("IConv.", blue), MCS (magenta) PFs, and for MCS periods ("MCSp", black; b). MCSp was built by selecting only instants for which a MCS PF has MCS attributes (see section 2a of the main manuscript). The PDF (in a) were normalized by the total number of PF.

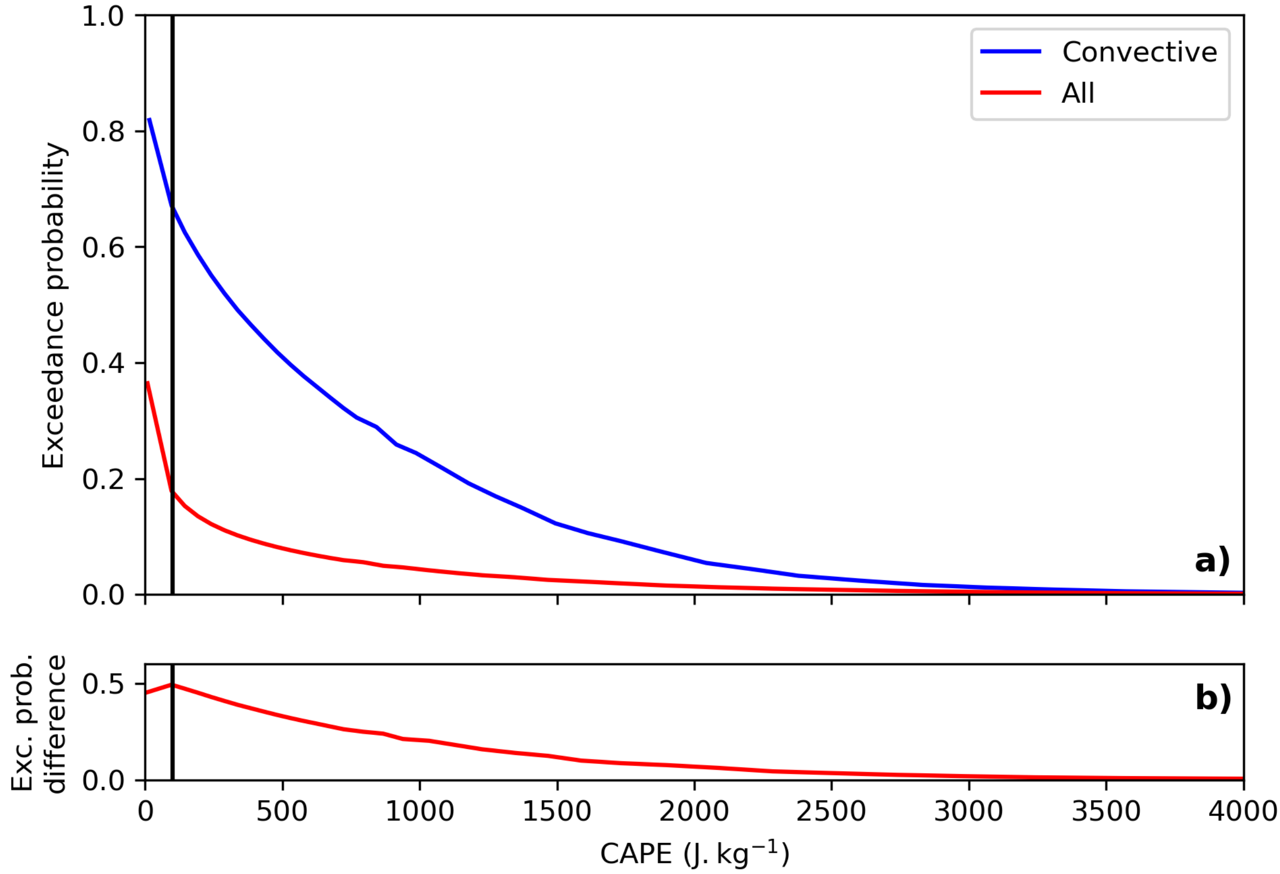

Figure S2. Exceedance probability of Convective Available Potential Energy (CAPE) for SYNOP convective observation events (blue), and for all observation events (red; a) and their difference (b) as a function of CAPE.

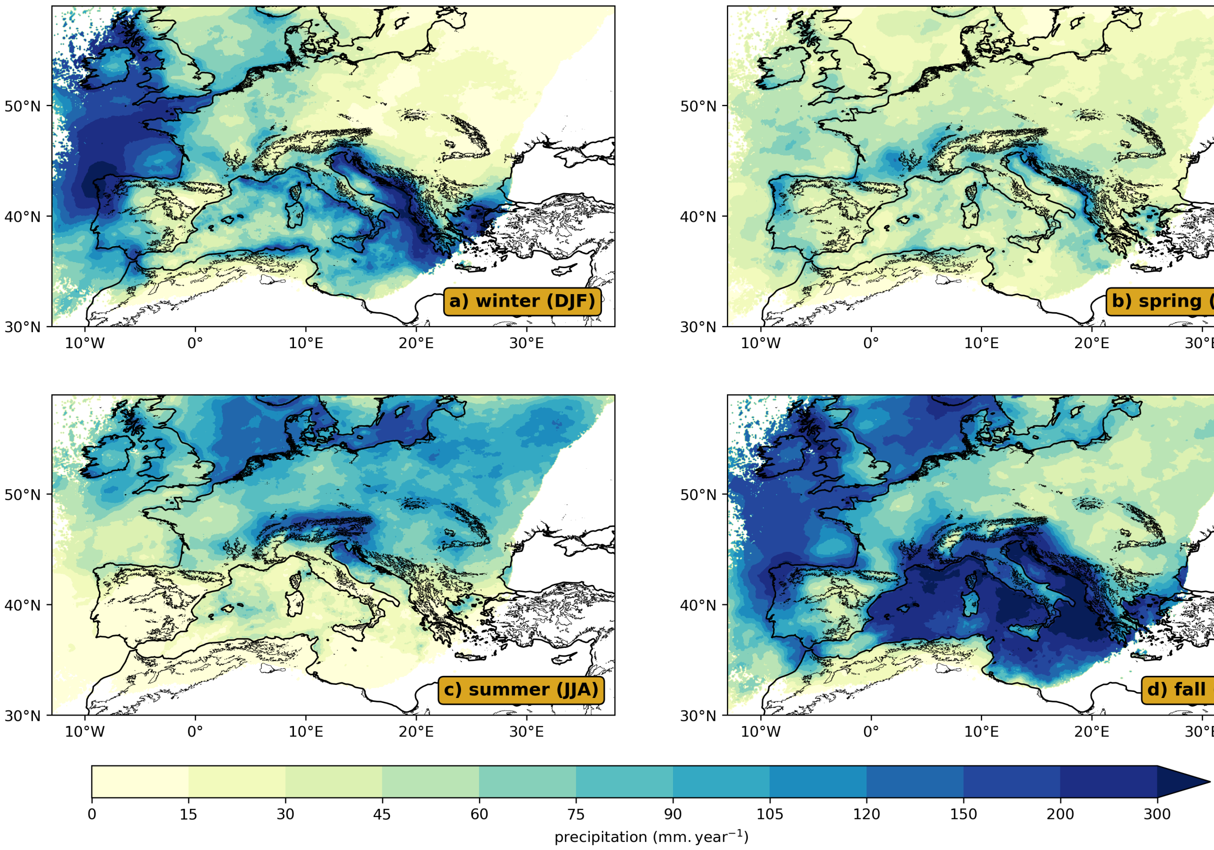

Figure S3. Total precipitation per year from MCS identified based on the alternative CAPE method (text S1) over Europe in winter (DJF, a), spring (MAM, b), summer (JJA, c) and fall (SON, d).

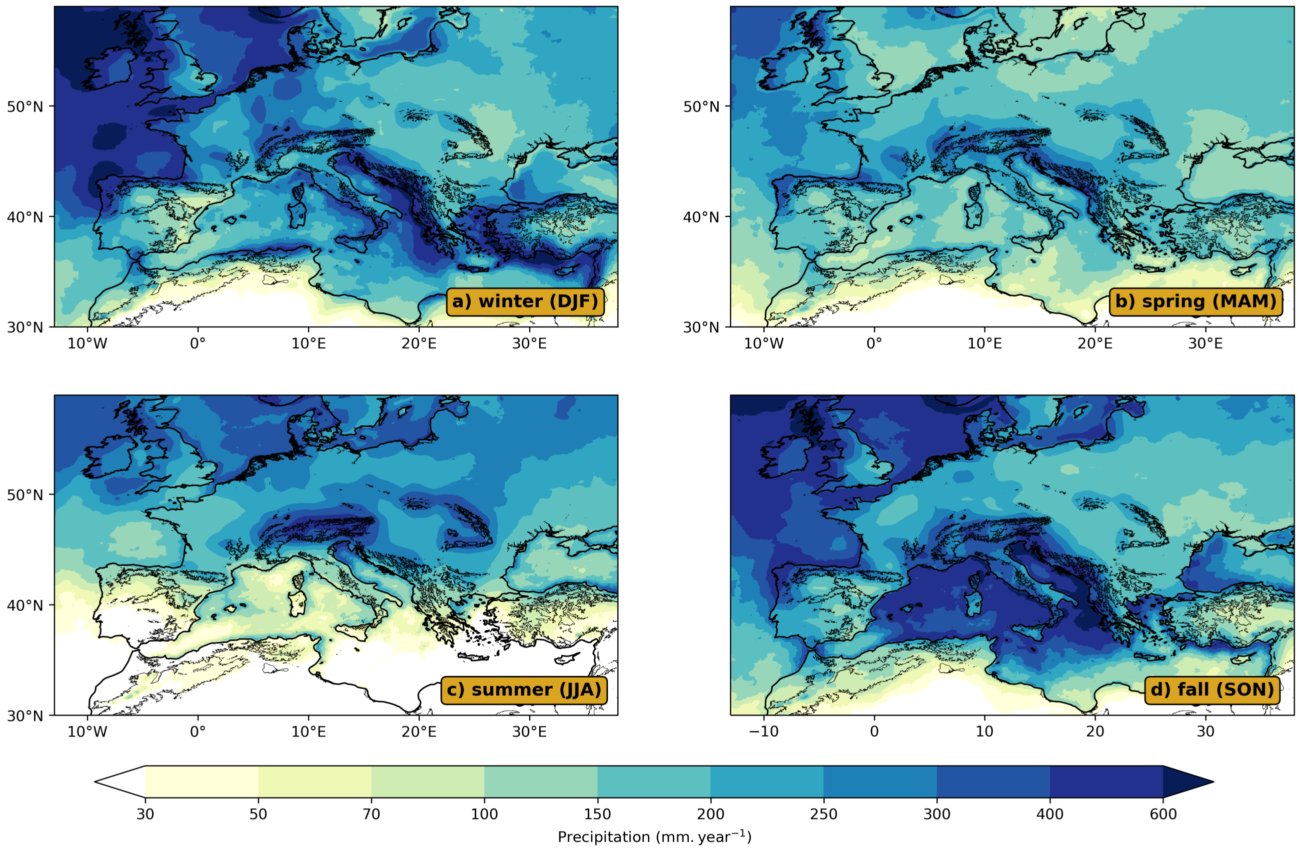

Figure S4. Total IMERG precipitation climatology (from 2001 to 2020; in mm.year^{-1}) over Europe in winter (DJF, a), spring (MAM, b), summer (JJA, c) and fall (SON, d).

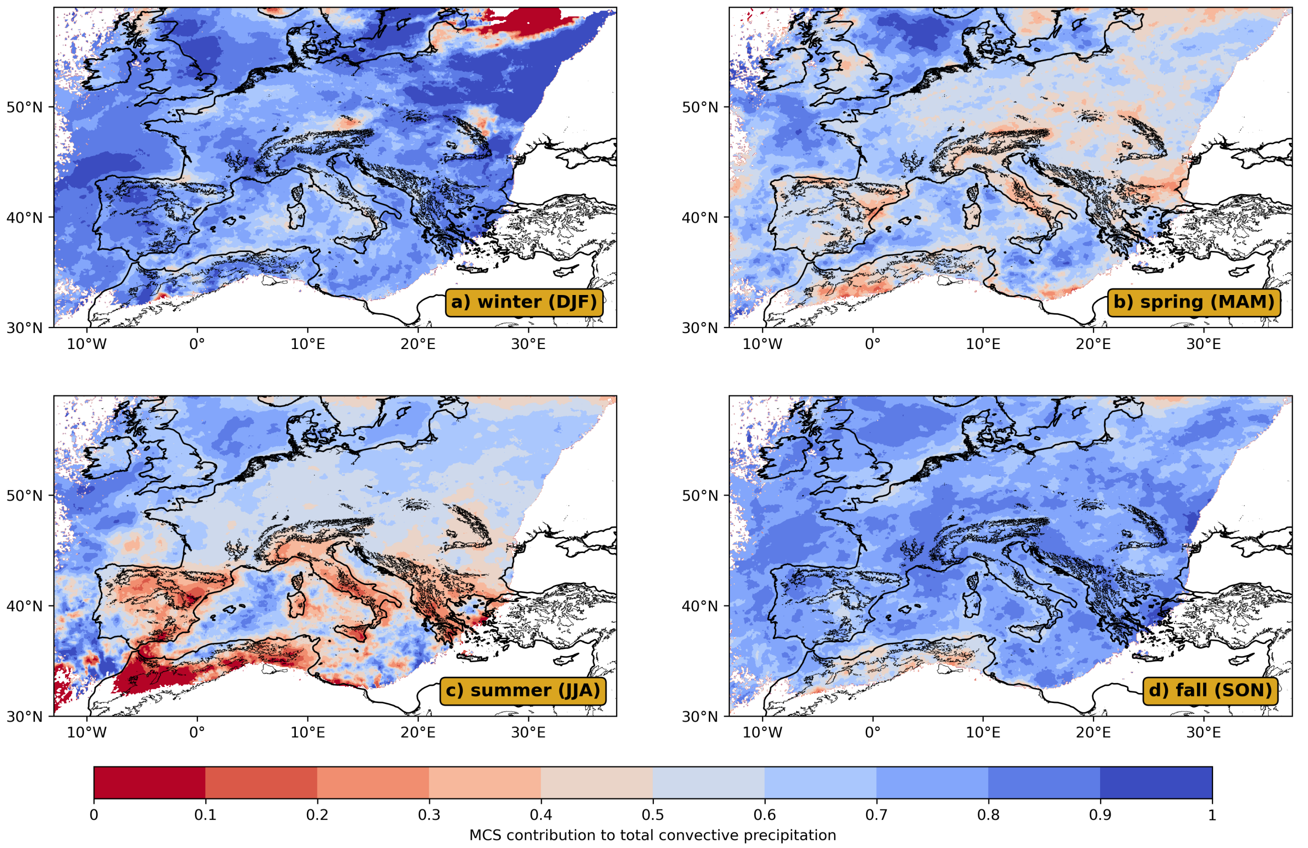

Figure S5. Contribution of MCS to convective precipitation over Europe in winter (DJF, a), spring (MAM, b), summer (JJA, c) and fall (SON, d).

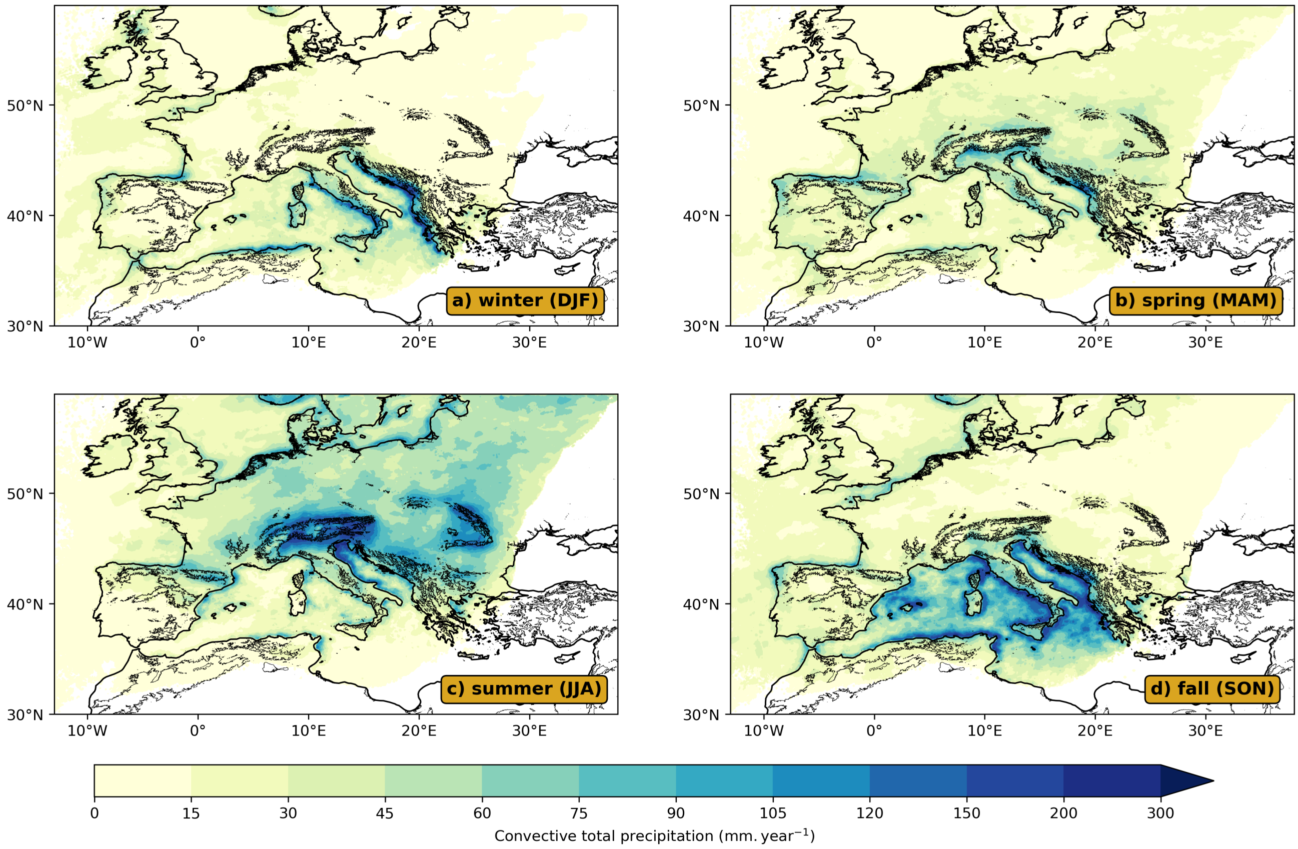

Figure S6. Total precipitation per year (in mm.year^{-1}) from isolated convective PFs over Europe in winter (DJF, a), spring (MAM, b), summer (JJA, c) and fall (SON, d).

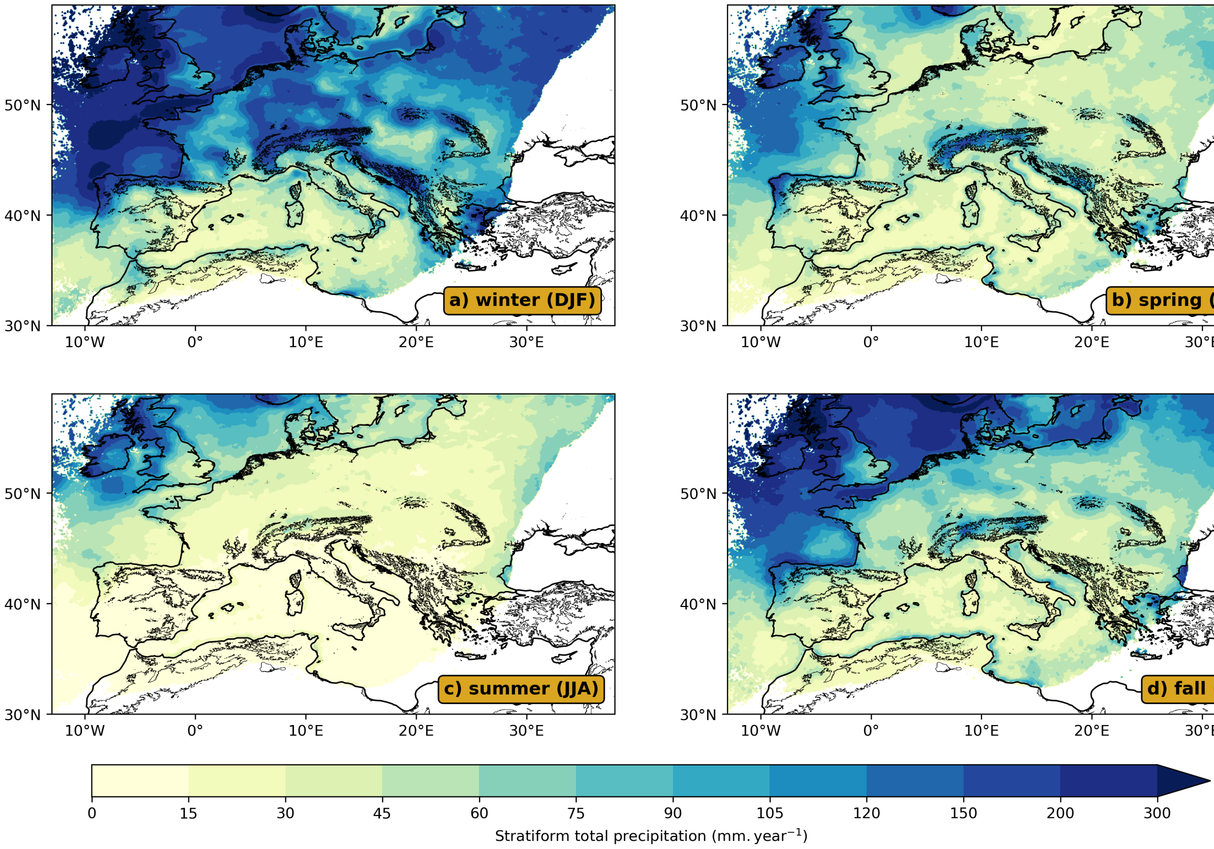

Figure S7. Total precipitation per year (in mm.year^{-1}) from stratiform PFs over Europe in winter (DJF, a), spring (MAM, b), summer (JJA, c) and fall (SON, d). White areas represent missing values, defined as points with means of less than one lightning strike per year.

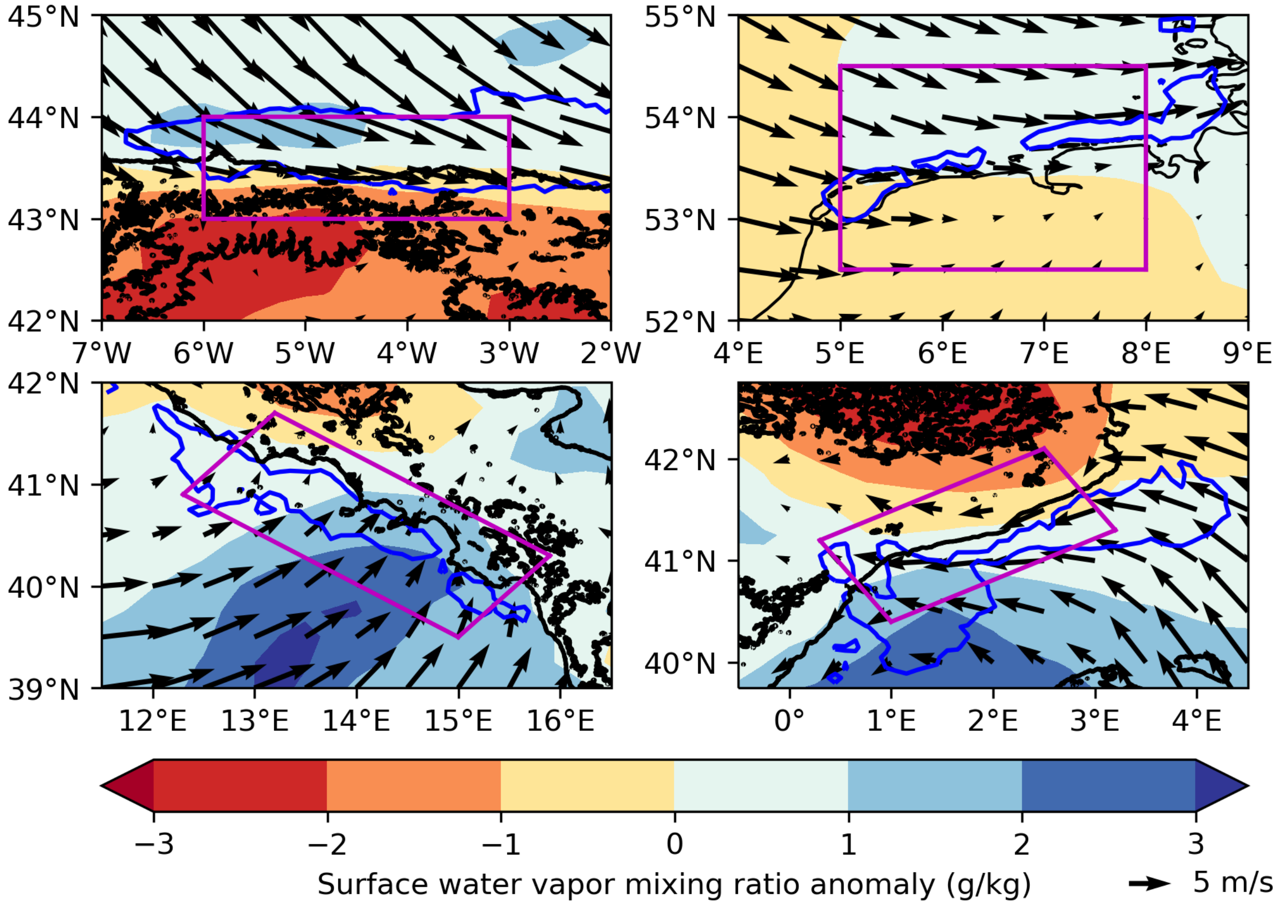

Figure S8. Surface water vapor mixing ratio (shadings) and wind (arrows) monthly anomalies for isolated convection coastal precipitation events (inside the magenta box) in December over the coasts of northern Spain (a), Netherlands and Germany (b), western Italy (c) and eastern Spain (d). Blue contours delimit areas where isolated convection mean precipitation is above 0.5 mm for these events.

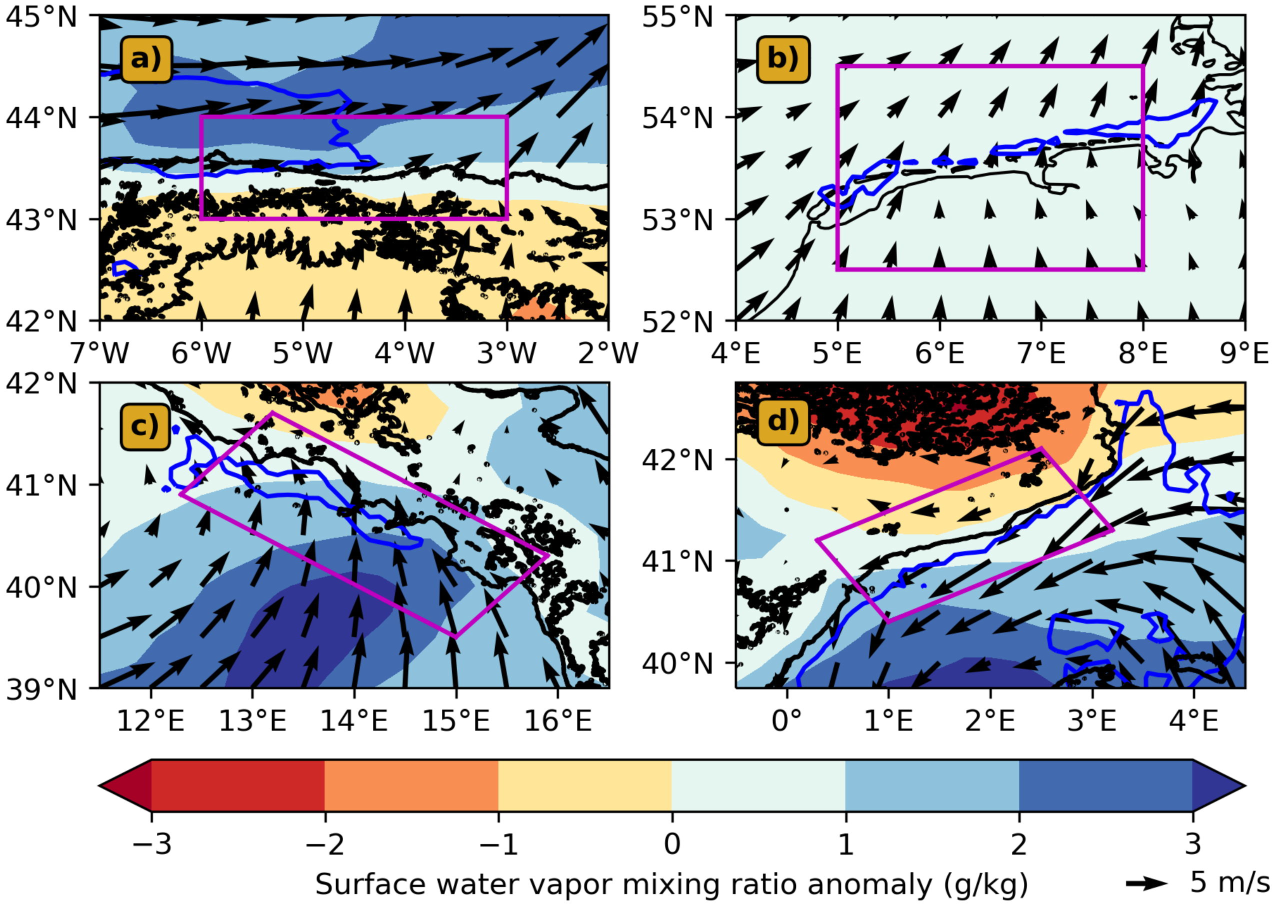

Figure S9. Surface water vapor mixing ratio (shadings) and wind (arrows) monthly anomalies for MCS coastal precipitation events (inside the magenta box) in December over the coasts of northern Spain (a), Netherlands and Germany (b), western Italy (c) and eastern Spain (d). Blue contours delimit areas where MCS mean precipitation is above 2 mm for these events.

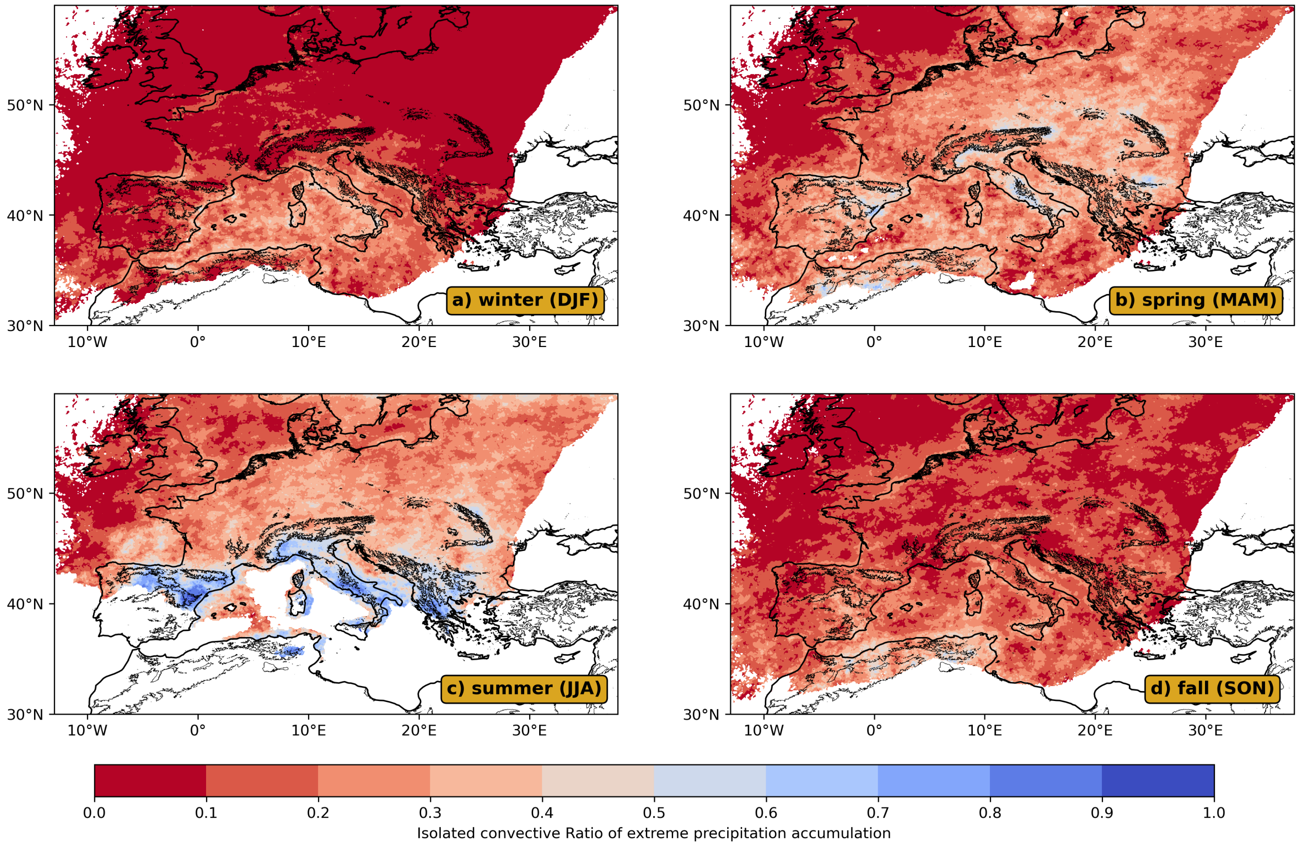

Figure S10. Contribution of isolated convection to the precipitation features producing the 10% most extreme precipitation accumulations (as defined in section 3.4) over Europe in winter (DJF, a), spring (MAM, b), summer (JJA, c) and fall (SON, d).

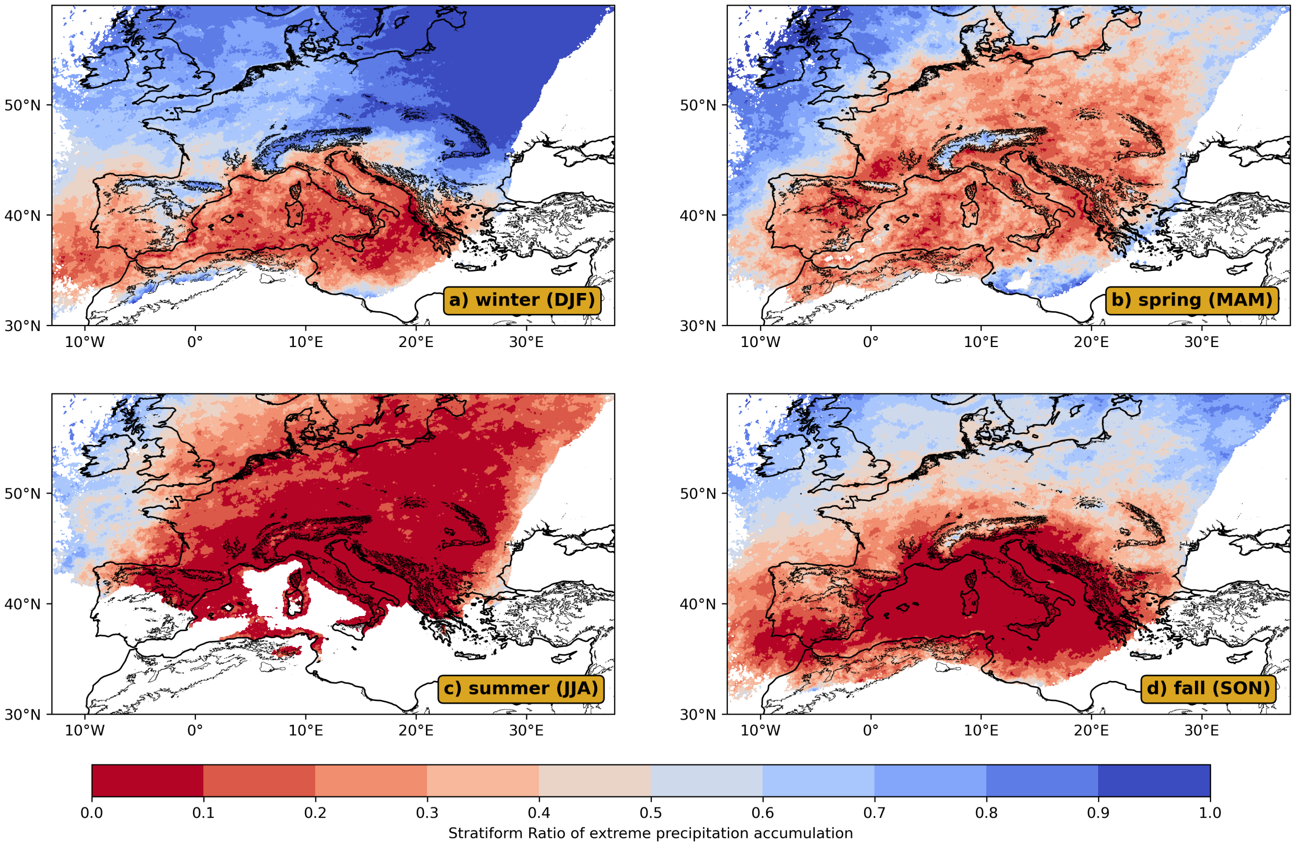

Figure S11. Contribution of stratiform events to the precipitation features producing the 10% most extreme precipitation accumulations (as defined in section 3.4) over Europe in winter (DJF, a), spring (MAM, b), summer (JJA, c) and fall (SON, d).

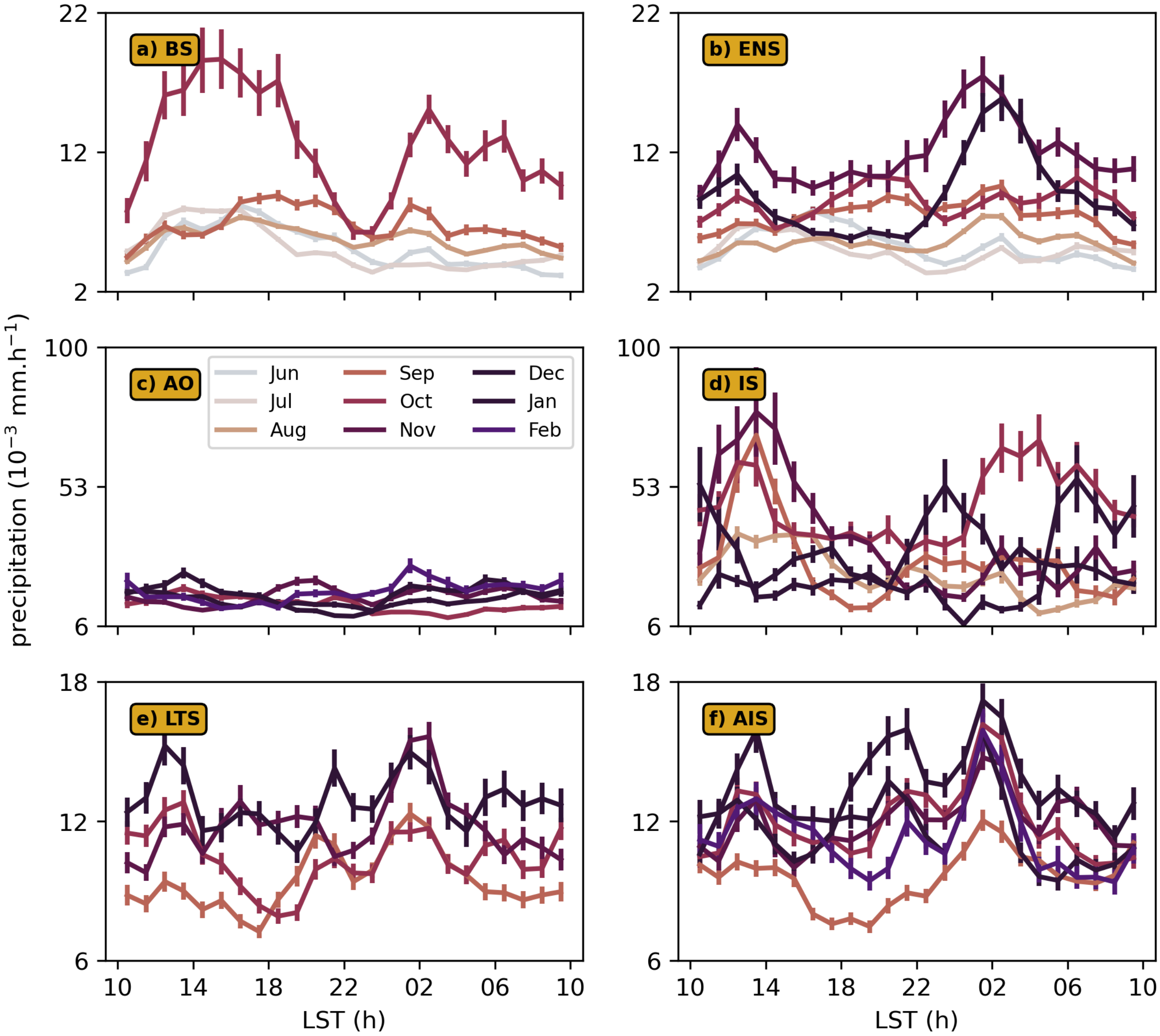

Figure S12. Monthly expected values of isolated convective precipitation (in mm.h^{-1}) conditioned on isolated convection occurrence within the coastal sub-regions as a function of LST: BS (a), ENS (b), AO (c), IS (d), LTS (e) and AIS (f) (see Fig. 3 of the main manuscript). Results are given for months with the main MCS activity according to Fig. 4 of the main manuscript. For each LST bin the standard error is calculated to estimate the uncertainty in the mean and represented by error bars.

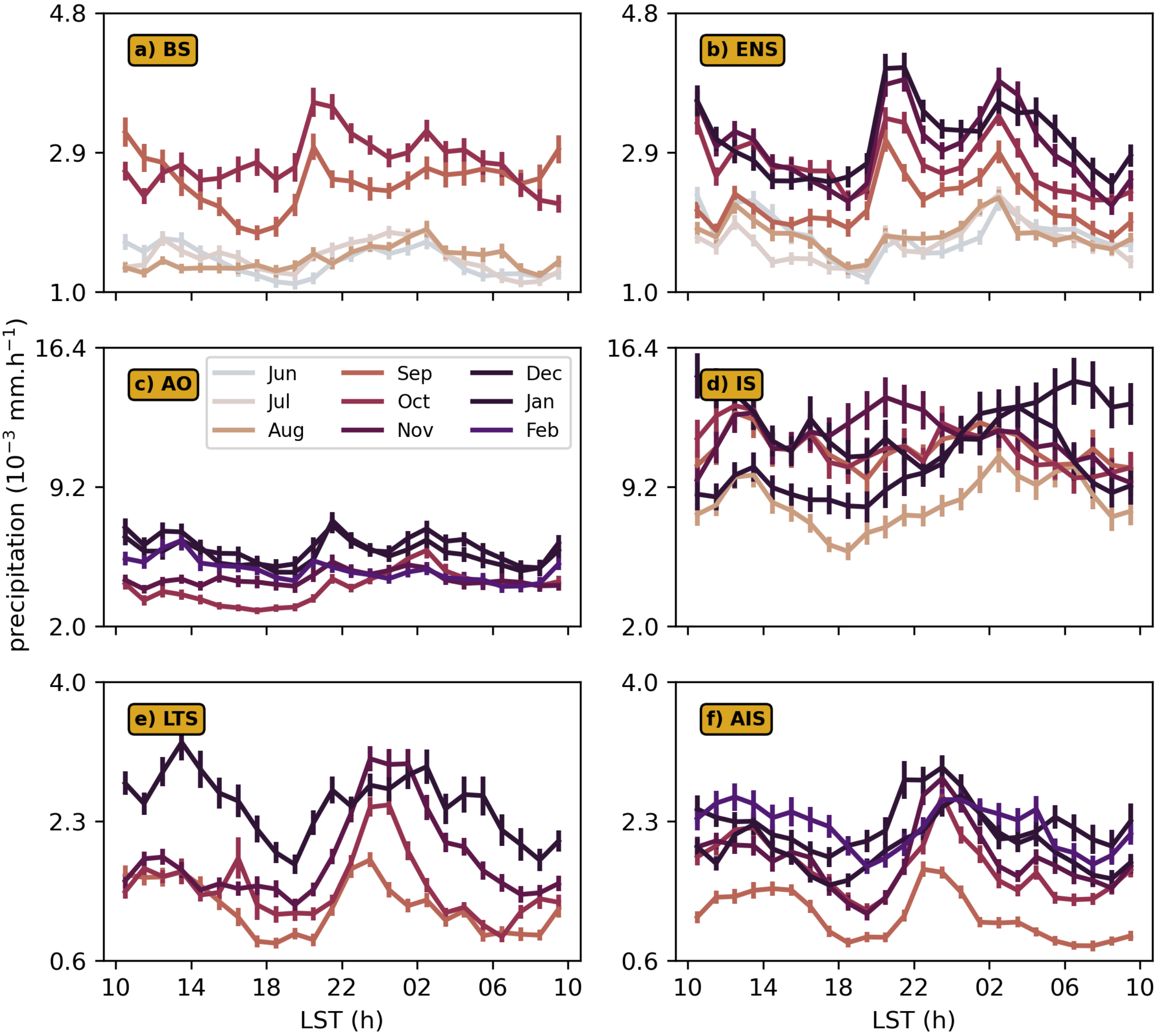

Figure S13. Monthly expected values of stratiform precipitation (in mm) conditioned on stratiform precipitation occurrence within the coastal sub-regions as a function of LST: BS (a), ENS (b), AO (c), IS (d), LTS (e) and AIS (f) (see Fig. 3 of the main manuscript). Results are given for months with the main MCS activity according to Fig. 4 of the main manuscript. For each LST bin the standard error is calculated to estimate the uncertainty in the mean and represented by error bars.

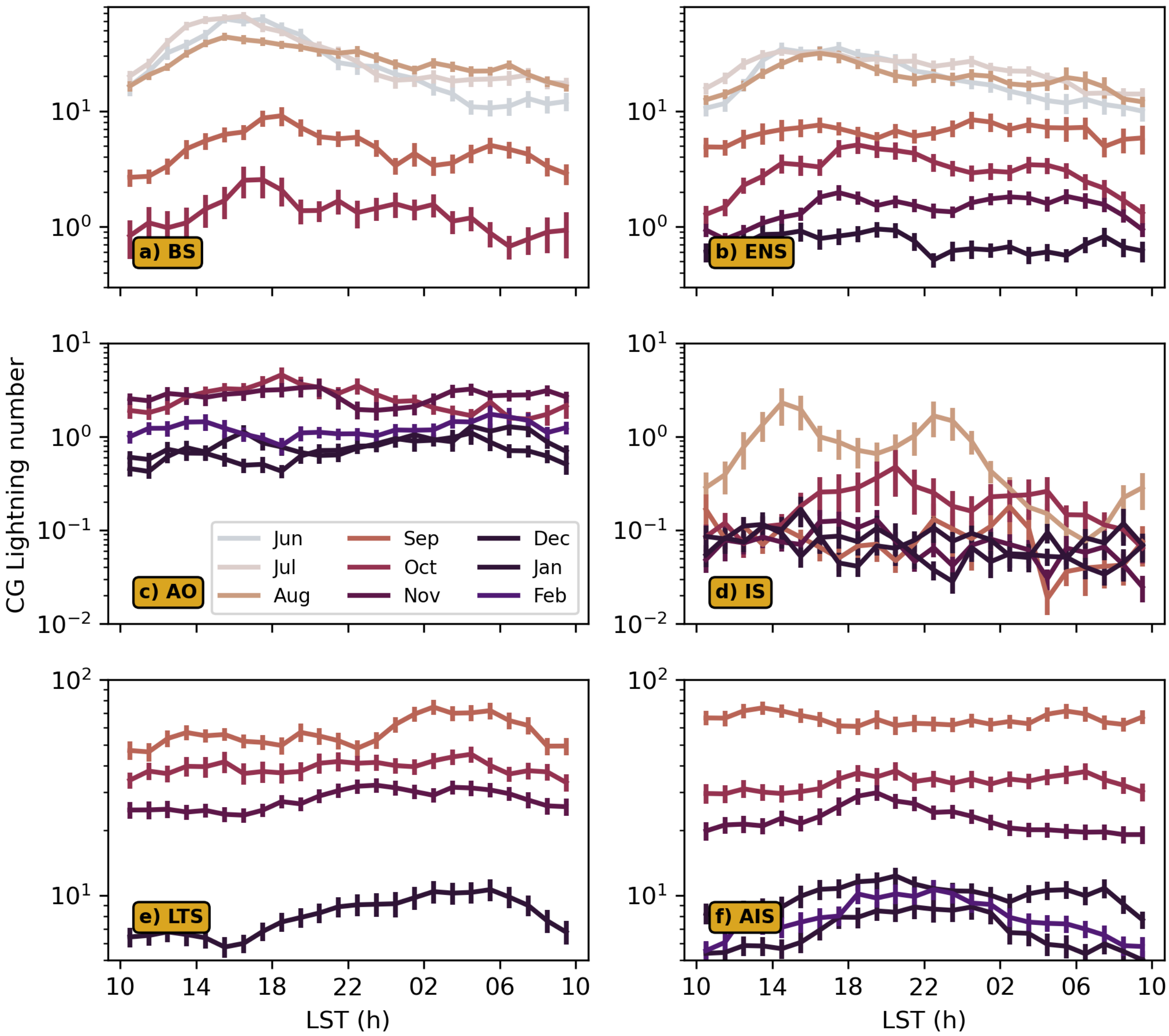

Figure S14. Monthly averaged diurnal cycle of EUCLID Cloud to Ground lightning strikes for the coastal sub-regions: BS (a), ENS (b), AO (c), IS (d), LTS (e) and AIS (f) (see Fig. 3 of the main manuscript).

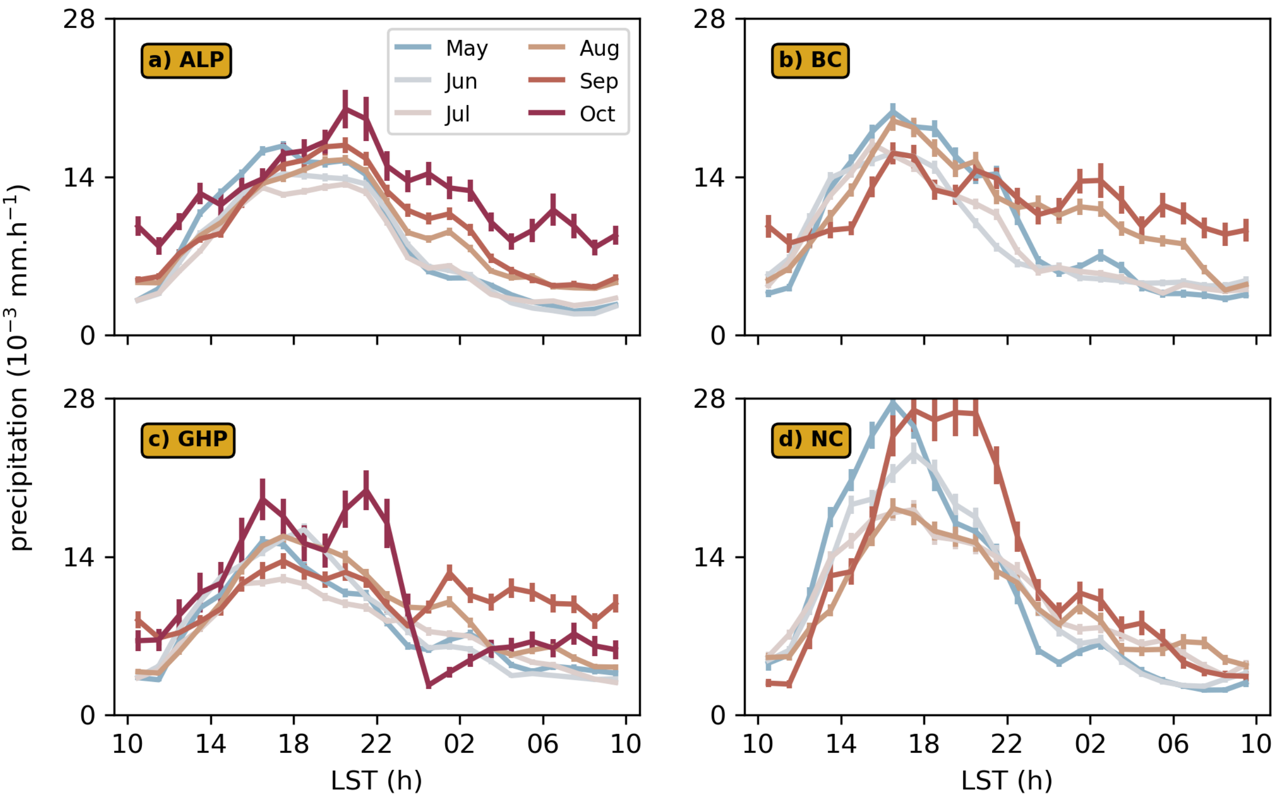

Figure S15. Monthly expected values of isolated convection precipitation (in mm.h^{-1}) conditioned on isolated convection occurrence within the continental sub-regions as a function of LST: ALP (a), BC (b), GHP (c) and NC (d) (see Fig. 3 of the main manuscript). Results are given for months with the main MCS activity according to Fig. 4 of the main manuscript. For each LST bin the standard error is calculated to estimate the uncertainty in the mean and represented by error bars.

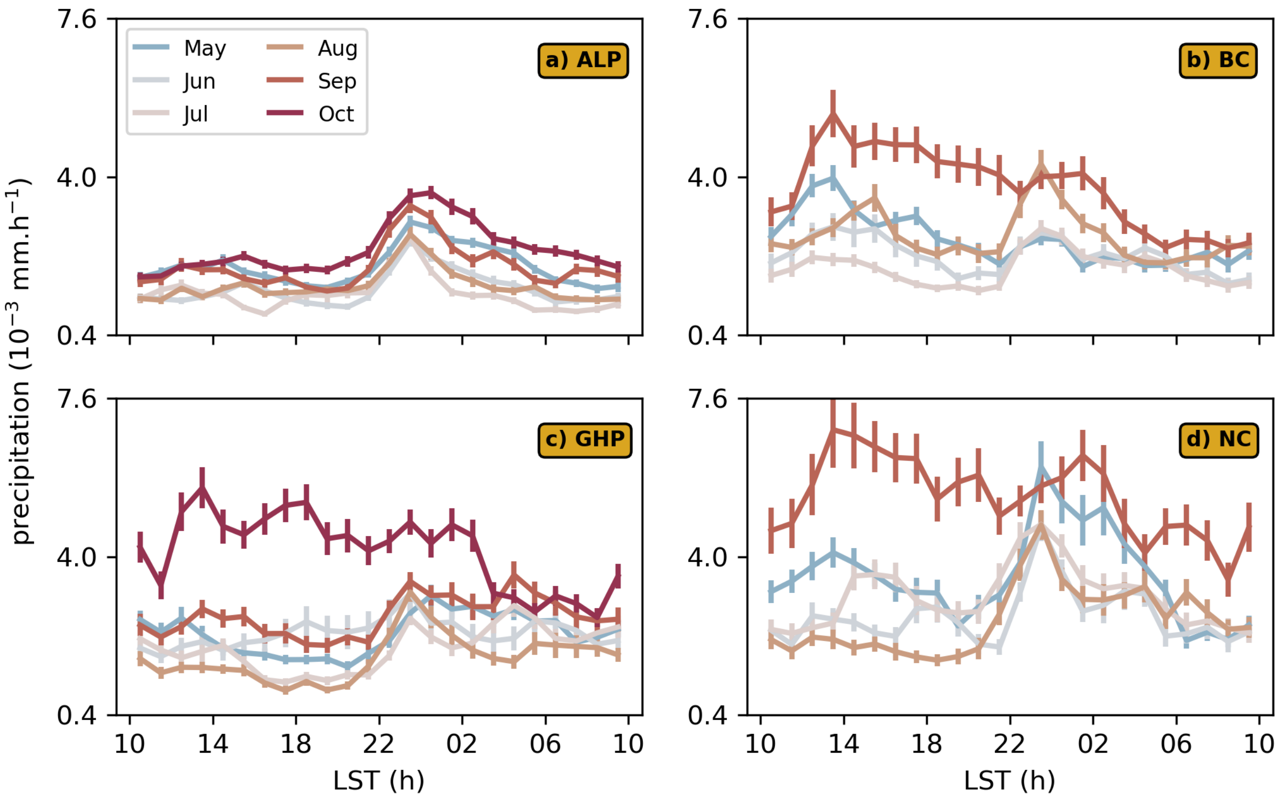

Figure S16. Monthly expected values of stratiform precipitation (in mm.h^{-1}) conditioned on stratiform precipitation occurrence within the continental sub-regions as a function of LST: ALP (a), BC (b), GHP (c) and NC (d) (see Fig. 3 of the main manuscript). Results are given for months with the main MCS activity according to Fig. 4 of the main manuscript. For each LST bin the standard error is calculated to estimate the uncertainty in the mean and represented by error bars.

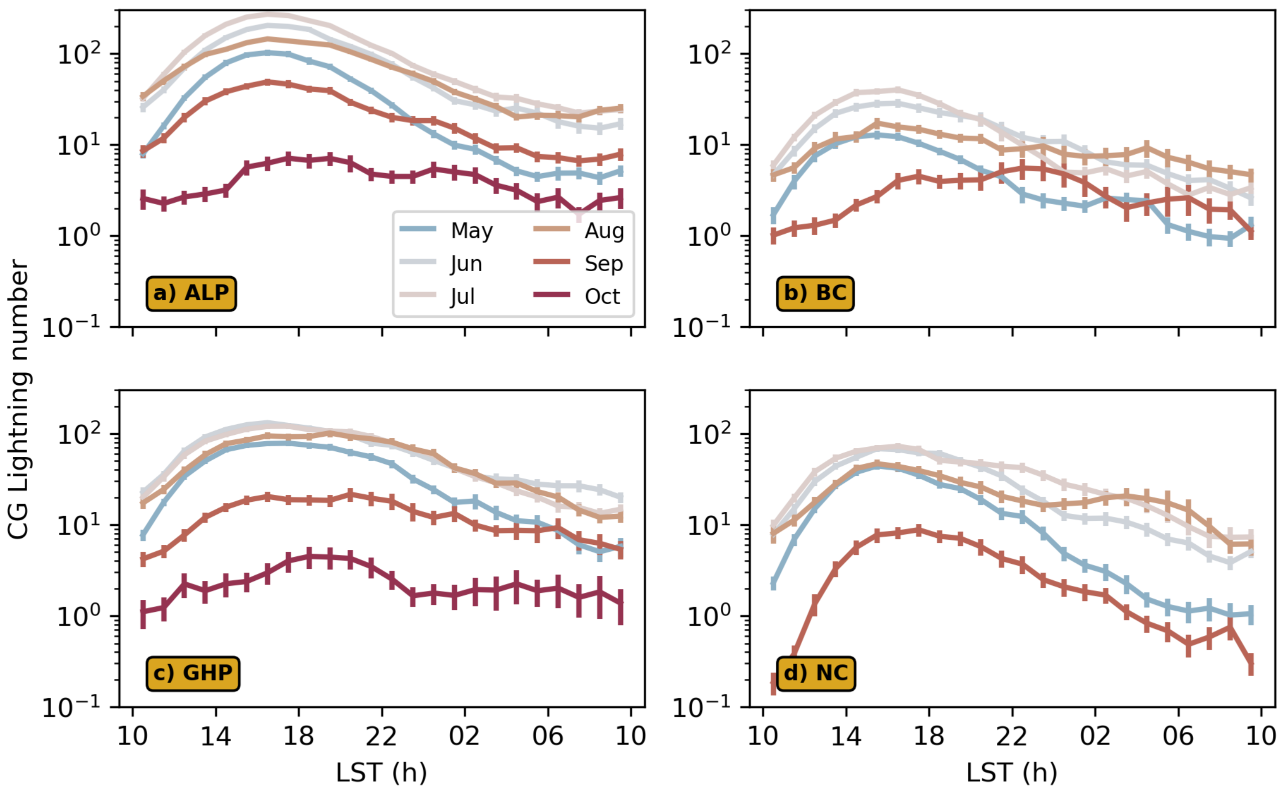

Figure S17. Monthly averaged diurnal cycle of EUCLID Cloud to Ground lightning strikes for the continental sub-regions: ALP (a), BC (b), GHP (c) and NC (d) (see Fig. 3 of the main manuscript).

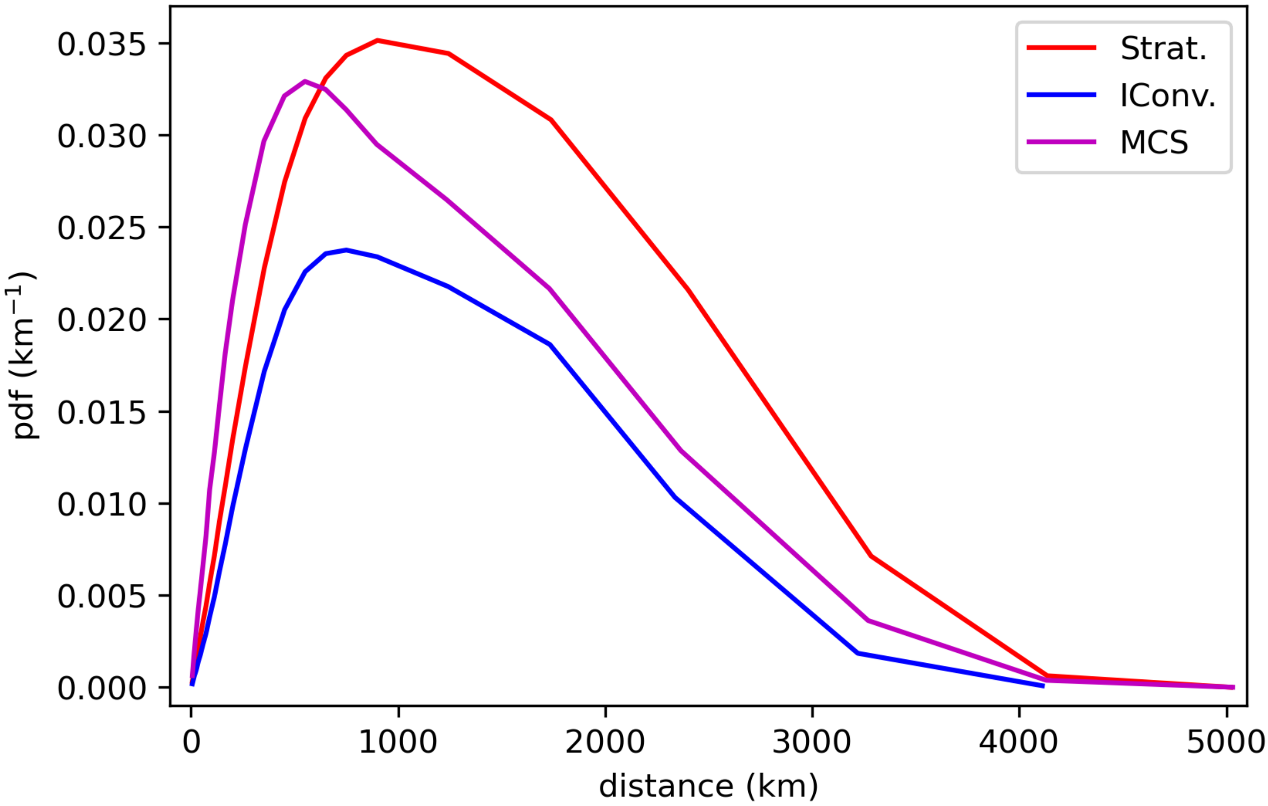

Figure S18. Unnormalized probability density functions (pdf) of frontal pixels as a function of distance from the center of every stratiform ("Strat.",red), isolated convective ("IConv", blue) and MCS (magenta) PFs at their maximum extent.